

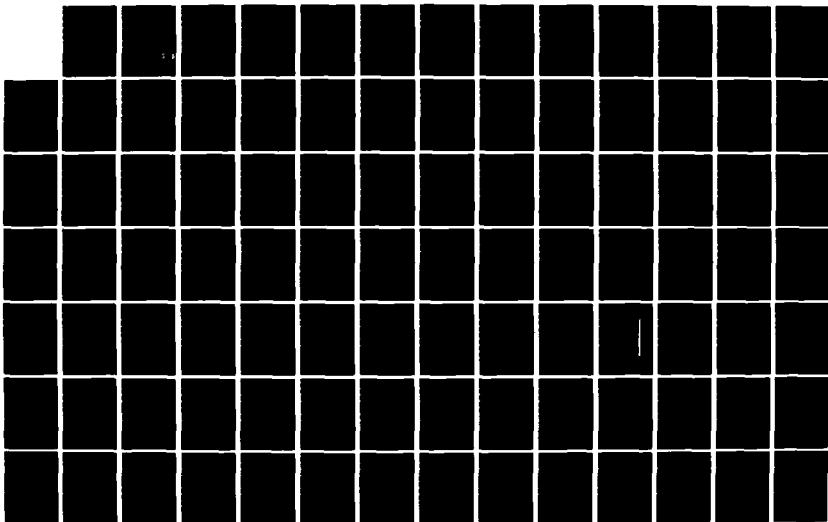
AD-A154 467

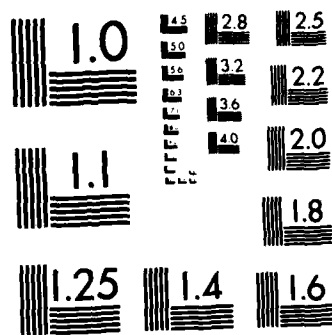
A NUMERICAL SOLUTION OF A NONISOTHERMAL WALL USING THE  
TWO-DIMENSIONAL NA. (U) AIR FORCE INST OF TECH  
WRIGHT-PATTERSON AFB OH SCHOOL OF ENGI. T K ROBERTS  
MAR 85 AFIT/GAE/AA/85M-5 F/G 28/13

1/2

UNCLASSIFIED

NL





MICROCOPY RESOLUTION TEST CHART  
NATIONAL BUREAU OF STANDARDS-1963-A

AD-A154 467



A NUMERICAL SOLUTION OF A NONISOTHERMAL  
WALL USING THE TWO-DIMENSIONAL  
NAVIER-STOKES EQUATIONS

THESIS

Timothy K. Roberts  
Captain, USAF

Accession  
NTIS GR  
DTIC TAB  
Unannounced  
Justification

This document has been approved  
for public release and sale; its  
distribution is unlimited.

DTIC  
ELECTE  
JUN 4 1985  
S P E D

DTIC FILE COPY

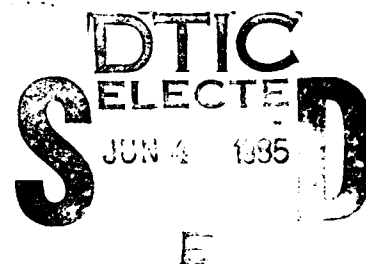
DEPARTMENT OF THE AIR FORCE  
AIR UNIVERSITY

**AIR FORCE INSTITUTE OF TECHNOLOGY**

Wright-Patterson Air Force Base, Ohio

8 5 5 0 175

AFIT/GAE/AA/85M-5



A NUMERICAL SOLUTION OF A NONISOTHERMAL  
WALL USING THE TWO-DIMENSIONAL  
NAVIER-STOKES EQUATIONS

THESIS

Timothy K. Roberts  
Captain, USAF

AFIT/GAE/AA/85M-5

Accession For	
NTIS GRA&I	<input checked="" type="checkbox"/>
DTIC TAB	<input type="checkbox"/>
Unannounced	<input type="checkbox"/>
Justification	
By	
Distribution/	
Availability Codes	
Avail and/or	
Dist	Special
A/	



AFIT/GAE/AA/85M-5

A NUMERICAL SOLUTION OF A NONISOTHERMAL WALL  
USING THE TWO-DIMENSIONAL NAVIER-STOKES EQUATIONS

THESIS

Presented to the Faculty of the School of Engineering  
of the Air Force Institute of Technology  
Air University  
In Partial Fulfillment of the  
Requirements for the Degree of  
Master of Science in Aeronautical Engineering

Timothy K. Roberts, B.S.

Captain, USAF

March 1985

Approved for public release; distribution unlimited

## PREFACE

I have always been interested in fluid flows and ways of analyzing them. When I was offered the opportunity by Maj Hodge to investigate a method of analyzing the nonisothermal wall effect in hypersonic flow, I was both excited and interested in the project. The study itself was intended to be a proof-of-concept for the numerical methods used and a stage to show the aerospace industry that the nonisothermal wall effect is important and can be included in design analyses. While the results of the thesis have shown that the particular method used is not the optimal approach, I feel that the objectives of the study have been met.

Attempting any project of this size creates a long list of indebtedness; the fact that it was necessary for me to continue the effort after leaving AFIT only lengthens that list. One of the most important people, of course, has been my advisor, Maj James K. Hodge. His insight, direction, and especially patience have been invaluable to me in completing this project. The help I received from Dr Urmilla Ghia of the University of Cincinnati while she was at AFIT as a Distinguished Visiting Professor, and from Dr Wilbur Hankey and Dr Joseph Shang of the Flight Dynamics Laboratory at Wright-Patterson AFB has been valuable and illuminating. I thank Dr Ghia for introducing me to the rigor necessary to

wrest correct results from recalcitrant equations. Drs Hankey and Shang were invaluable in helping master the nuances of computational fluid dynamics.

Finishing a thesis after leaving AFIT requires the active support from the people you work with. First on this list is my branch chief, Mr Ed Barth. Without his active support of my studies, this thesis would not have been completed. Drs Phil Kessel and Joseph Baum have been very helpful in aiding and critiquing my efforts. Finally, the people in my section, who understood when their section chief was somewhat preoccupied at times.

The most important acknowledgment has been saved for last. It is an oft-stated truism that "I couldn't have done it without my wife." This is a truth that repetition cannot dim. Mary has been at my side throughout AFIT and after, egging me on, supporting me, and showing me that someone else cared, too. More than anyone else, Mary, this one's for you. And to David, who shouldn't have but did.

Timothy K. Roberts

# TABLE OF CONTENTS

	Page
List of Figures . . . . .	vi
List of Symbols . . . . .	viii
Abstract . . . . .	x
I. Introduction . . . . .	1
Background . . . . .	1
Objective . . . . .	3
II: Theoretical Development . . . . .	4
Overview . . . . .	4
Boundary Layer Solutions . . . . .	6
Reason For Discarding Boundary Layer Approximations . . . . .	10
Navier-Stokes Solutions . . . . .	11
Heat Transfer Modeling . . . . .	12
III: Numerical Solution Method . . . . .	15
Overview . . . . .	15
Numerical Grid . . . . .	15
MacCormack's Explicit Method . . . . .	18
IV: Program Description . . . . .	23
Overview . . . . .	23
NONISOCODE . . . . .	23
STEADY . . . . .	30
V: Results . . . . .	32
Overview . . . . .	32
Flow Conditions . . . . .	32
Limitations of Results . . . . .	33
Heat Transfer Solutions . . . . .	36
Flow Field Solutions . . . . .	39
Shock Wave-Boundary Layer Interactions . . . . .	41
Numerical Oscillations . . . . .	43
VI: Conclusions and Recommendations . . . . .	45
Overview . . . . .	45
Conclusions . . . . .	45



Nonisothermal Wall Effect . . . . .	45
Shock Wave-Boundary Layer Interaction .	46
Pressure Spike Due To Nonisothermal Wall . . . . .	46
Numerical Methods . . . . .	46
Recommendations . . . . .	48
Bibliography . . . . .	79
Appendix A: Program Listings for NONISOCODE and STEADY	81
Vita . . . . .	117

# LIST OF FIGURES

Figure		Page
1	Test Article . . . . .	51
2	Semi-Adaptive Physical Grid . . . . .	52
3	Nondimensional Convective Heat Transfer Coefficient . . . . .	53
4	Isothermal Streamwise Velocity Surface . . .	54
5	Isothermal Streamwise Velocity Contours . .	55
6	Isothermal Normal Velocity Surface . . . . .	56
7	Isothermal Normal Velocity Contours . . . .	57
8	Isothermal Mach Number Surface . . . . .	58
9	Isothermal Mach Number Contours . . . . .	59
10	Isothermal Temperature Surface . . . . .	60
11	Isothermal Temperature Contours . . . . .	61
12	Isothermal Pressure Surface . . . . .	62
13	Isothermal Pressure Contours . . . . .	63
14	Isothermal Density Surface . . . . .	64
15	Isothermal Density Contours . . . . .	65
16	Nonisothermal Streamwise Velocity Surface . . . . .	66
17	Nonisothermal Streamwise Velocity Contours . . . . .	67
18	Nonisothermal Normal Velocity Surface . . .	68
19	Nonisothermal Normal Velocity Contours . . .	69
20	Nonisothermal Mach Number Surface . . . . .	70
21	Nonisothermal Mach Number Contours . . . . .	71
22	Nonisothermal Temperature Surface . . . . .	72

23	Nonisothermal Temperature Contours . . . . .	73
24	Nonisothermal Pressure Surface . . . . .	74
25	Nonisothermal Pressure Contours . . . . .	75
26	Nonisothermal Density Surface . . . . .	76
27	Nonisothermal Density Contours . . . . .	77
28	Surface Pressure . . . . .	78

# LIST OF SYMBOLS

<u>Symbol</u>	<u>Definition</u>	<u>Units</u>
$c$	speed of sound	ft/sec
$C_p$	specific heat	ft-lb <sub>f</sub> /slug-deg R
$e$	energy	
$h$	convective heat transfer coefficient	Btu/ft <sup>2</sup> -sec-deg R
$i, j, k$	orthogonal unit vectors	
$k$	thermal conductivity	Btu/ft-sec-deg R
$L$	reference length	ft
	MacCormack operator	
$M$	Mach number	
$P$	pressure	lb <sub>f</sub> /ft <sup>2</sup>
$Pr$	Prandtl number	
$Q$	exponential stretching factor	
$r$	recovery factor	
$Re$	Reynolds number	
$T$	temperature	degrees Rankine (deg R)
$t$	time	seconds
$U$	streamwise velocity	ft/sec
$V$	normal velocity	
$\delta$	wedge deflection angle	degrees
$\gamma$	ratio of specific heats	
$\rho$	density	slugs/ft <sup>3</sup>
$\sigma_{ij}, \tau_{ij}$	stress tensor components	

$\mu$	coefficient of viscosity	slugs/ft-sec
$\lambda$	bulk viscosity	
$\eta$	transformed normal coordinate	
$\xi$	transformed streamwise coordinate	

#### Subscripts

aw	adiabatic wall
e	value at edge of boundary layer
i,j	value at a plane location (i,j)
ref	reference value
w	value at the wall or surface
w <sub>1</sub>	leading edge surface value
w <sub>2</sub>	trailing edge surface value
$\infty$	freestream value

#### Superscripts

n	value at time step n
*	value at Eckert's reference conditions

# ABSTRACT

Wind tunnel tests of Space Shuttle Orbiter insulating articles have demonstrated the presence of a nonisothermal wall effect, which is a lag in heat transfer recovery after the flow passes over a surface temperature discontinuity resulting in a downstream transport of energy. Theoretical analyses and numerical simulations of hypersonic flow over discontinuous nonisothermal surfaces using boundary layer theory have also indicated the presence of this effect.

This thesis studies the nonisothermal wall effect by modeling the hypersonic flow over an inclined wedge with a discontinuous nonisothermal surface. The flow is modeled using the two-dimensional Navier-Stokes equations. MacCormack's method is used to solve the Navier-Stokes equations. The program used to implement these methodologies is discussed and a listing given. A semi-adaptive grid is used to represent the physical conditions of the problem. Heat transfer is presented as a nondimensional ratio of the local convective heat transfer coefficient to a reference heat transfer coefficient. *Adapted from: J. Spacecraft and Rockets, Vol. 17, No. 1, 1980, p. 1-10.*

The results of this study show that the nonisothermal wall effect can be successfully modeled using the two-dimensional Navier-Stokes equations and MacCormack's explicit method. The lag in the recovery of the convective heat transfer coefficient is found to match lags seen in other

analyses of the problem. Due to the high Mach number modeled, a shock wave-boundary layer interaction is found to have an effect on the heat transfer. A significant surface pressure spike is found to occur downstream of the discontinuity, which may be a result of the increase in size of the momentum and thermal boundary layers at the discontinuity.

The study concludes that the nonisothermal wall effect can be adequately modeled by the two-dimensional Navier-Stokes equations; that the shock wave-boundary layer interaction does have an effect on the heat transfer; and that the occurrence of a spike in surface pressure may be a unique result of the nonisothermal wall effect. Significant recommendations include the need for further study of the nonisothermal wall effect, the need to use more optimal grids and solution methods, the need to more thoroughly investigate the shock wave-boundary layer effect, and the need for further study of the surface pressure response to the nonisothermal wall effect.

A NUMERICAL SOLUTION OF A NONISOTHERMAL WALL  
USING THE TWO-DIMENSIONAL NAVIER-STOKES EQUATIONS

CHAPTER I: INTRODUCTION

BACKGROUND

The development and use of the Space Transportation System has given rise to some unanticipated problems in reentry aerodynamics. The fact that the flow field over the Orbiter is laminar during reentry down to Mach 8 permits some phenomena usually masked by turbulent flow to become evident. One such phenomenon which significantly affects the flow and the heat transfer is the nonisothermal wall effect. This effect occurs when flow passes over a surface composed of two or more materials of different thermal response. The nonisothermal wall effect occurs at numerous locations on the Orbiter's surface. One such location is the junction between the reusable carbon-carbon (RCC) nose-cap and the reusable surface insulation (RSI) tiles. The flow must pass over a discontinuity in wall temperature due to different thermal responses. Similar discontinuities exist at numerous other places on the Orbiter's surface.

During reentries of earlier space vehicles such as Apollo or ballistic missile reentry vehicles, the flow over the vehicle was turbulent. The mixing inherent in turbulent flow, augmented by the surface roughness of these vehicles,



reduces the dramatic change in the wall heat transfer induced by a nonisothermal wall condition. However, an Orbiter reentry is characterized by a laminar flow field over much of the vehicle's surface until the Orbiter has decelerated to about Mach 8; at that point, transition to turbulent flow is abrupt. Thus, the nonisothermal wall effect becomes evident. In fact, the localized scorching and discoloration seen on Columbia, Challenger, and Discovery seem to be caused by the nonisothermal wall effect.

Studies of wind tunnel tests of Orbiter insulating articles have demonstrated the presence of this effect. Theoretical analyses using boundary layer theory of hypersonic nonisothermal walls had indicated that the discontinuity in wall temperature would induce changes in the flow. Numerical simulations using classical boundary-layer theory backed up these findings. However, the wind tunnel tests indicated that when the flow passed from a steel surface to a surface of Orbiter insulation material, wall temperature recovery was much slower than that predicted by either Eckert high-speed plate theory or boundary-layer simulations. The data gathered in these tests would seem to indicate that some other effect is at least as important as normal diffusion in transporting energy. First, axial diffusion of energy at a location where there is a discrete change in wall temperature over an axial distance of order less than the normal boundary layer

thickness is one possible effect. Second, the viscous shock wave - boundary layer interaction at hypersonic speeds changes the pressure and heat transfer in an axial direction. These two effects have not been investigated on a nonisothermal wall.

#### OBJECTIVE

The objective of this thesis is to numerically model hypersonic flow over an isothermal and a nonisothermal wall using the two-dimensional Navier-Stokes equations. The use of the Navier-Stokes equations allows accurate modeling of the axial diffusion if there is sufficient axial grid resolution. The nonisothermal wall effect should be very noticeable. This paper will attempt to show the effects of the shock wave-boundary layer interaction and axial diffusion of energy on the nonisothermal wall effect.

## CHAPTER II: THEORETICAL DEVELOPMENT

### OVERVIEW

The objective of this thesis is to numerically model hypersonic flow over a wedge with and without a discontinuity in surface temperature. This chapter will discuss the theory behind the investigation. The problem will be described and possible avenues of investigation proposed. The best method of solution will be selected and reasons for that selection will be discussed.

### PROBLEM DESCRIPTION

The physical problem to be modeled is a wedge in a hypersonic flow field. The problem is described in Cappelano (1:2-5), Hodge et al (2:2), and Woo (3). See Figure 1 for a picture. A steel test article has a 6 inch by 6 inch test plate inserted in it 7 inches behind the leading edge of the test article. Cappelano reviewed and interpreted wind tunnel test data for three types of inserts: a thin steel plate (for calibration), a piece of high temperature reusable surface insulation (HRSI), and a piece of flexible reusable surface insulation (FRSI). Woo reduced the data for the HRSI and the FRSI test runs. Each insert was instrumented with varying numbers of surface thermocouples to record the axial surface temperature distribution. The FRSI insert had the most thermocouples and hence the most complete set of axial surface temperature readings; thus, the FRSI insert is modeled in this study. Only one angle of

attack is simulated in this study; restrictions on computer time required that excursions to other angles of attack be deferred to later studies.

The flow conditions modeled were as follows: a freestream Mach number of 14.24, freestream stagnation temperature of 2000 degrees Rankine (deg R), and a wedge inclination angle of 3 degrees. The combination of high Mach number and stagnation temperature produce a very low freestream static temperature of 48 deg R; several problems will arise from this. One of the immediate ones is that gradients will be very steep in the boundary layer, requiring significant resolution over a very thin layer. Another problem is that any numerically-induced waves could easily cause temperatures just in front of the leading edge to become negative in the computations, thus causing the solution to stop.

#### AVENUES OF INVESTIGATION

Several avenues of investigation are available to solve a problem such as this, depending on the desired results. Approaches fall into two broad categories: boundary layer solutions and Navier-Stokes solutions. Both approaches will be examined in some detail below. Boundary-layer oriented solutions offer a relatively fast solution, but at the expense of some details of the flow. If the problem is such that those approximations cannot be accepted, then the

investigator must use methods of increasing complexity, collectively known as the Navier-Stokes family of solutions.

There are several levels of complexity within the family of Navier-Stokes solutions. Slightly more complicated, but consequently more realistic, are the parabolized Navier-Stokes equations. Beyond that are the "full" Navier-Stokes equations in two or three dimensions. For reasons to be explained in more detail below, a two-dimensional Navier-Stokes solution was selected for this problem.

#### BOUNDARY LAYER SOLUTIONS

Boundary layer solutions depend on Prandtl's boundary layer theory. The approximations made by this theory are such that, in most cases, the solution resulting from boundary layer theory is very close to the actual flow field. This is especially true in low Mach number or incompressible flows. At hypersonic Mach numbers, the boundary layer approximations tend to give results that diverge somewhat from the actual flow field, especially when there is an interaction between the oblique shock and the viscous boundary layer.

The boundary layer equations developed by Prandtl make several important assumptions. These assumptions follow from some basic observations about the nature of any flow field. The boundary layer is defined as that region near the surface of the body in which the flow velocity increases

from zero at the wall (due to the viscous nature of fluids) to the freestream velocity at some distance from the body. Experimentation has shown that this distance, the boundary layer thickness, is normally quite small compared to other characteristic lengths of the problem. Prandtl's boundary layer equations can be derived from the full set of the two-dimensional Navier-Stokes equations using order of magnitude analysis. The variables used will be assumed to be in nondimensional form. For example, the axial velocity component is nondimensionalized with respect to the freestream velocity and has an order of magnitude of one. Likewise, the axial length is nondimensionalized with respect to the length of the wedge and is of order one. The normal length is nondimensionalized with respect to the boundary layer thickness,  $\delta$ . Thus, it has an order of magnitude of  $\delta$ . With these building blocks, the two-dimensional Navier-Stokes equations can be reduced to Prandtl's boundary layer equations.

Consider first the continuity equation:

$$\frac{\partial}{\partial x}(\rho u) + \frac{\partial}{\partial y}(\rho v) = 0 \quad (2.1)$$

$\frac{1}{1} \qquad \frac{\delta}{1}$

The appropriate order of magnitude has been written below each term. In order to maintain the continuity equation, it can be seen that the order of magnitude of the normal velocity component,  $v$ , must be  $\delta$ .

Next, consider the axial linear momentum equation:

$$\frac{\partial}{\partial t}(\rho u) + \frac{\partial}{\partial x}(\rho u^2 - \tau_{11}) + \frac{\partial}{\partial y}(\rho uv - \tau_{12}) = 0 \quad (2.2)$$

The stress tensor terms  $\sigma_{11}$  and  $\tau_{12}$  are defined as (4:61):

$$\sigma_{11} = -P + \frac{1}{Re} \left( \frac{4}{3} \frac{\partial u}{\partial x} - \frac{2}{3} \frac{\partial v}{\partial y} \right) \quad (2.3a)$$

$$\tau_{12} = \frac{1}{Re} \left( \frac{\partial u}{\partial y} + \frac{\partial v}{\partial x} \right) \quad (2.3b)$$

Substituting these terms into Eq. 2.2:

$$\begin{aligned} \frac{\partial}{\partial t}(\rho u) + \frac{\partial}{\partial x} \left[ \rho u^2 + P - \frac{1}{Re} \left( \frac{4}{3} \frac{\partial u}{\partial x} - \frac{2}{3} \frac{\partial v}{\partial y} \right) \right] \\ \frac{1}{\delta} \quad \frac{1}{1} \quad 1 \quad \delta^2 \quad \frac{1}{\delta} \quad \frac{\delta}{\delta} \\ + \frac{\partial}{\partial y} \left[ \rho uv - \frac{1}{Re} \left( \frac{\partial u}{\partial y} + \frac{\partial v}{\partial x} \right) \right] = 0 \\ \frac{1}{\delta} \quad 1 \delta \quad \delta^2 \quad \frac{1}{\delta} \quad \frac{\delta}{1} \end{aligned} \quad (2.4)$$

The appropriate order of magnitude has been written under each term for which it is known. By discarding those terms with orders of less than one (i.e., orders of delta and its multiples), the axial linear momentum equation becomes:

$$u \frac{\partial u}{\partial x} + v \frac{\partial u}{\partial y} = -\frac{1}{\rho} \frac{\partial P}{\partial x} - \frac{1}{\rho} \frac{1}{Re} \frac{\partial^2 u}{\partial x^2} \quad (2.5)$$

Now consider the normal linear momentum equation:

$$\frac{\partial}{\partial t}(\rho v) + \frac{\partial}{\partial x}(\rho uv - \tau_{12}) + \frac{\partial}{\partial y}(\rho v^2 - \sigma_{22}) = 0 \quad (2.6)$$

The new stress tensor term  $\sigma_{22}$  is defined as (4:61):

$$\sigma_{22} = -P + \frac{1}{Re} \left( \frac{4}{3} \frac{\partial v}{\partial y} - \frac{2}{3} \frac{\partial u}{\partial x} \right) \quad (2.7)$$

Substituting for the stress tensor terms yields:

$$\begin{aligned} \frac{\partial}{\partial t}(\rho v) + \frac{\partial}{\partial x} \left[ \rho uv - \frac{1}{Re} \left( \frac{\partial u}{\partial y} + \frac{\partial v}{\partial x} \right) \right] \\ \frac{\delta}{1} \quad \frac{1}{1} \quad 1 \cdot \delta \quad \delta^2 \quad \frac{1}{\delta} \quad \frac{\delta}{1} \\ + \frac{\partial}{\partial y} \left[ \rho v^2 + P - \frac{1}{Re} \left( \frac{4}{3} \frac{\partial v}{\partial y} - \frac{2}{3} \frac{\partial u}{\partial x} \right) \right] = 0 \\ \frac{1}{\delta} \quad \delta^2 \quad \delta^2 \quad \frac{\delta}{\delta} \quad \frac{1}{1} \end{aligned} \quad (2.8)$$

where the orders of magnitude were again written under each term, as usual. The only term to survive in this equation is the partial derivative of pressure in the y-direction:

$$\frac{\partial P}{\partial y} = 0 \quad (2.9)$$

Finally, consider the energy equation:

$$\begin{aligned} \frac{\partial}{\partial t}(\rho e) + \frac{\partial}{\partial x} \left[ \rho u e - \frac{1}{Pr Re} \frac{\partial T}{\partial x} - u \tau_{11} - v \tau_{12} \right] \\ + \frac{\partial}{\partial y} \left[ \rho v e - \frac{1}{Pr Re} \frac{\partial T}{\partial y} - u \tau_{12} - v \tau_{22} \right] \end{aligned} \quad (2.10)$$

Substituting once more for the stress tensor terms:

$$\begin{aligned} \frac{\partial}{\partial t}(\rho e) + \frac{\partial}{\partial x} \left[ \rho u e - \frac{1}{Pr Re} \frac{\partial T}{\partial x} - u \left\{ -P + \frac{1}{Re} \left( \frac{4}{3} \frac{\partial u}{\partial x} - \frac{2}{3} \frac{\partial v}{\partial y} \right) \right\} \right] \\ - v \left\{ \frac{1}{Re} \left( \frac{\partial u}{\partial y} + \frac{\partial v}{\partial x} \right) \right\} \right] + \frac{\partial}{\partial y} \left[ \rho v e - \frac{1}{Pr Re} \frac{\partial T}{\partial y} - u \left\{ \frac{1}{Re} \left( \frac{\partial u}{\partial y} + \frac{\partial v}{\partial x} \right) \right\} \right] \\ - v \left\{ -P + \frac{1}{Re} \left( \frac{4}{3} \frac{\partial v}{\partial y} - \frac{2}{3} \frac{\partial u}{\partial x} \right) \right\} \right] = 0 \end{aligned} \quad (2.11)$$

the order of magnitude are once again listed under each term for which they are known. The resulting equation is:

$$\frac{\partial e}{\partial t} + u \frac{\partial e}{\partial x} + v \frac{\partial e}{\partial y} = -\frac{u}{\rho} \frac{\partial P}{\partial x} + \frac{1}{\rho Pr Re} \frac{\partial^2 T}{\partial y^2} + \frac{u}{\rho Re} \left( \frac{\partial u}{\partial y} \right)^2 \quad (2.12)$$

This is equivalent to the usually accepted boundary layer energy equation.

Eqs. 2.1, 2.5, 2.9, and 2.12 show explicitly the major assumptions in Prandtl's boundary layer theory. Eq. 2.1 shows that the dominant velocity term is in the axial direction; it will dominate the characteristics of the boundary layer. Eq. 2.5 reinforces this point and, along with Eq. 2.9, shows that the pressure distribution in the boundary layer varies only in an axial direction. The surface pressure is virtually equal to the impressed freestream pressure. Any shock wave-boundary layer interaction is ignored



by this assumption. Finally, Eq. 2.12 shows that virtually all the heat transfer occurs in the normal direction, with almost no axial diffusion. The consequences of Eq. 2.12 are that  $\Delta x$  is of order one. But if  $\Delta x$  is of order delta, such as across a discontinuity in wall temperature, the axial diffusion of energy is neglected. It should be noted that these results are best applied to incompressible or low-speed compressible flow problems.

#### REASONS FOR DISCARDING BOUNDARY LAYER SOLUTIONS

Boundary-layer oriented solutions were discarded a priori for this study for two basic reasons. First, the temperature derivatives in the streamwise or axial direction are ignored. Second, the boundary layer solutions do not adequately model the shock wave-boundary layer interaction that occurs at hypersonic Mach numbers.

The question of temperature derivatives is straightforward. Recall that this study wishes to investigate the nonisothermal wall effect. One of the constituents of the nonisothermal wall effect could be axial diffusion. Yet boundary layer theory ignores axial diffusion. Therefore, nonisothermal wall effect cannot be properly investigated with a tool that ignores axial diffusion.

The interaction of the leading edge shock wave and the boundary layer is an important part of the the flow field structure. Such shock wave-boundary layer interactions have

long been recognized as important; see, for example, an early article by Nagamatsu and Sheer (4:454-462). In this article, Nagamatsu described how induced surface pressures from the interaction were as high as twelve times the freestream pressure for a similar freestream Mach number. Clearly, in such an environment, boundary layer assumptions break down and more realistic models must be used. These two factors were the greatest contributors to discarding boundary layer solutions for this effort.

#### NAVIER-STOKES SOLUTIONS

The method of choice for solving fluid flow problems is solving the Navier-Stokes equations. Unfortunately, a general analytical solution is not available for the majority of applications; numerical solutions must be resorted to, as they were in this study. 'Small-scale' effects such as the nonisothermal wall effect can be seen and their importance evaluated.

The Navier-Stokes equations used here are written in conservative form, that is, in terms of  $\rho$ ,  $\rho u$ ,  $\rho v$ , and  $\rho e$ . The full set of equations used are:

$$\begin{bmatrix} \rho \\ \rho u \\ \rho v \\ \rho e \end{bmatrix}_t + \begin{bmatrix} \rho u \\ \rho u^2 - \sigma_{11} \\ \rho uv - \tau_{12} \\ \rho ue - \frac{1}{Pr Re} \frac{\partial T}{\partial x} - u \sigma_{11} - v \tau_{12} \end{bmatrix}_x$$

$$+ \begin{bmatrix} \rho v \\ \rho uv - \tau_{12} \\ \rho v^2 - \tau_{22} \\ \rho ve - \frac{1}{Pr Re} \frac{\partial T}{\partial y} - u \tau_{12} - v \tau_{22} \end{bmatrix}_y = \bar{0} \quad (2.13)$$

where:

$$\begin{aligned} \sigma_{11} &= -P + \frac{1}{Re} \left( \frac{4}{3} \frac{\partial u}{\partial x} - \frac{2}{3} \frac{\partial v}{\partial y} \right) \\ \tau_{12} &= \frac{1}{Re} \left( \frac{\partial u}{\partial y} + \frac{\partial v}{\partial x} \right) \\ \sigma_{22} &= -P + \frac{1}{Re} \left( \frac{4}{3} \frac{\partial v}{\partial y} - \frac{2}{3} \frac{\partial u}{\partial x} \right) \end{aligned} \quad (2.13a)$$

The grid used in this study is semi-adaptive; a complete discussion will be given below. The code used transforms the equations internally.

### HEAT TRANSFER MODELING

Heat transfer is expressed in this study as the convective heat transfer coefficient,  $h$ , also known as the film transfer coefficient. It is defined as:

$$h = \frac{-k \frac{\partial T}{\partial y} \big|_{wall}}{T_w - T_{aw}} \quad (2.14)$$

and is expressed in Btu/ft<sup>2</sup>-sec-deg R. To be able to compare results with Woo (3) and Hodge, the convective heat transfer coefficient is nondimensionalized with respect to a reference convective heat transfer coefficient based on

freestream quantities:

$$h_{ref} = 0.332 c_p \left( \frac{\mu_{\infty} \rho_{\infty} u_{\infty}}{x} \right)^{1/2} \quad (2.15)$$

Note that the only variable is the distance along the wedge in feet,  $x$ . Thus,  $h_{ref}$  is truly a reference condition at any point along the surface of the wedge. According to Eckert, for an isothermal wall and no viscous shock-boundary layer interaction, the ratio of  $h$  to  $h_{ref}$  is independent of  $x$ .

In both quantities, the coefficient of viscosity,  $\mu$ , is determined by Sutherland's law:

$$\mu = \frac{\mu_0 T_w^{3/2}}{T_w + 198.6^\circ R} ; \mu_0 = 2.27 \times 10^{-8} \frac{\text{slug}}{\text{ft} \cdot \text{sec} \cdot \sqrt{R}} \quad (2.16)$$

Although Sutherland's law is generally considered to be valid down to about 180 deg R (4:19), Hodge et al have determined that Sutherland's law can be applied to lower temperature flows with minimal error (2:2). The thermal conductivity of air is computed by:

$$k = \frac{\mu c_p}{J Pr} ; J = 778 \frac{\text{ft} \cdot \text{lb}_f}{\text{Btu}} \quad (2.17)$$

with units of Btu/ft-sec-deg R. The Prandtl number is taken to be constant,  $Pr = 0.72$ . Both the coefficient of viscosity and thermal conductivity are computed at the wall conditions.

Eckert's reference temperature,  $T^*$ , can be used to validate the use of Sutherland's law for computation of the

coefficient of viscosity.  $T^*$  is defined as (6:304):

$$T^* = T_e + \left( \frac{T_w - T_e}{2} \right) + 0.22 (T_{aw} - T_e) \quad (2.18)$$

where  $T_e$  is the boundary layer edge temperature (also equal to the freestream static temperature behind the shock), and  $T_w$  is the wall temperature (which will vary for the nonisothermal wall). Adiabatic wall temperature,  $T_{aw}$ , is defined as (6:301):

$$T_{aw} = T_\infty \left[ 1 + \frac{r}{2} (\gamma - 1) M_\infty^2 \right] \quad (2.19)$$

where the recovery factor,  $r$ , is taken to be a constant,  $r = 0.9$ . This is not the generally accepted definition; the recovery factor is usually defined as the square root of the Prandtl number. However, this alternative definition simplifies computations, causes only a few percent deviation from convective heat transfer coefficient computed with the "traditional" recovery factor, and allows direct comparison with Hodge's and Woo's results.  $T^*$  is an empirical correcting factor. Eckert found that if one assumes the specific heats to be constant, one can use  $T^*$  to correlate many "exact" laminar boundary layer solutions to within a few percent. It is also apparent that if  $T^*$  is greater than 180 deg R, Sutherland's law is appropriate for the computation of the coefficient of viscosity. In this case,  $T^*$  is equal to over 765 deg R. Thus, the use of Sutherland's law is justified.

### CHAPTER III: NUMERICAL SOLUTION METHODS

#### OVERVIEW

This chapter will consider the generation and use of the numerical grid and the numerical implementation of the Navier-Stokes equations in NONISOCODE using MacCormack's explicit method.

#### NUMERICAL GRID

The numerical grid used in this study was a semi-adaptive grid. It was generated in such a way so as to achieve two goals: a) maintain about ten points in the boundary layer at all positions along the plate, and b) maintain thirty points in the normal direction at all stations along the plate. The combination of these two goals led to the use of a semi-adaptive grid.

The normal grid distribution was found to be the solution of the following differential equation:

$$\frac{\partial^2 y}{\partial \eta^2} + Q \frac{\partial y}{\partial \eta} = 0 \quad (3.1)$$

The solution to this equation is:

$$y = \left[ \frac{y_{\max}}{1 - e^{-Q\eta_{\max}}} \right] (1 - e^{-Q\eta}) \quad (3.2)$$

where  $y$  is the solved physical location of the normal grid point,  $y_{\max}$  is the highest physical grid location,  $\eta$  is the number of the grid point being solved for,  $\eta_{\max}$  is the maximum number of grid points, and  $Q$  is the stretching

exponent.

The primary goal was to maintain about ten points in the boundary layer at all stations in the streamwise direction. This was required in order to adequately model the temperature inversion that exists there. An earlier phase of this effort had shown that it is very easy to miss that inversion if the grid isn't carefully planned, thus rendering the results useless. The limit of ten points in the boundary layer was set to keep the required stretching down; NONISOCODE will not run a grid that has a stretching exponent much greater than -0.15. Ten points was considered an acceptable compromise between desired level of detail and the requirements of the parent code.

The secondary goal of maintaining thirty points in the normal direction at all stations was an objective of convenience. It would have been possible to use forty, fifty, or more points in the normal direction to achieve any desired level of detail; however, the price paid is that of increased run time for the solution and increasingly unwieldy arrays. Use of more than thirty points in the normal direction was considered unnecessary for the level of detail desired. To do so would have required more modifications to the code; simple enough in theory but prone to error in application.

Generating the grid was a trial-and-error process. There were several known constraints. One was the minimum

height of the grid needed at the downstream edge of the computational domain in order to pass shock and Mach waves (i.e., not have them reflect off the far-field boundary). Another constraint was the compromise between the number of points in the boundary layer and the total number of points in the normal direction mentioned above. It was decided that the grid should grow in the normal direction proportional to the boundary layer thickness. Allowing  $y_{\max}$  to increase while maintaining the same exponential stretch and total number of points was done using this equation:

$$\text{GRIDY}_i = \text{GRIDY}_{\text{ref}} \left( \frac{X_i}{X_{\text{ref}}} \right)^{1/2} \quad (3.3)$$

The normal coordinate is proportional to the square root of the ratio of the current streamwise coordinate to a reference coordinate. The constant of proportionality is the reference normal coordinate. The choice of the reference coordinate is somewhat arbitrary; the driving factor influencing it is the location of the closest point to the leading edge that allows ten points in the temperature inversion. For an exponential stretching coefficient of  $Q = -0.15$ , that location was  $X/L = 0$ . The actual grid growth began at the leading edge; prior to that, the grid used was a rectangular, regular grid for the three points in the freestream ahead of the wedge. The rationale here is that freestream conditions are not computationally severe and hence can be accommodated in a regular grid. Beginning



the semi-adaptive grid at the leading edge accounts for the growth of the boundary layer.

Figure 2 is a plot of the grid used in this study. Note that the initial gradient of the parabolic grid is quite steep. This is because the boundary layer is growing very quickly near the leading edge. Note also that the steepest grid gradients are in the most benign flow region. Near the leading edge, the shock wave is very close to the surface and the boundary layer is very thin. Thus, at the far-field boundary, the flow is essentially inviscid and at freestream conditions. The stagnation region, the area of sharp turning in the flow, and the shock wave are all present in a region of relatively small grid gradients, not unlike the gradients found elsewhere in the computational domain.

#### MACCORMACK'S EXPLICIT METHOD

NONISOCODE implements the Navier-Stokes equations using MacCormack's explicit method. MacCormack's method is one of the best known methods for numerically solving supersonic and hypersonic flow problems. Originally presented in 1969 (8), the method has become widely used for many high-speed problems.

The adjective 'explicit' refers to the fact that a solution at any point in the flow is independent of the solution at any other point at that time step. One of the

distinguishing characteristics of super- and hypersonic problems is that information cannot travel upstream, since the flow velocity everywhere (except in a very thin region within the boundary layer) is greater than the speed at which flow information can travel - the speed of sound. In the problem under consideration, the vast majority of the flow to be solved is in the hypersonic flow regime with only a small (but important) region in the subsonic regime. Thus, a solution method that is efficient in the hypersonic regime is desirable. MacCormack's explicit method is an efficient method at high velocities (i.e., super- and hypersonic). It is true that a very important portion of the flow to be solved is subsonic (the boundary layer where the bulk of the heat transfer occurs). It is also true that implicit methods are more efficient in subsonic regimes. However, since the overall flow is mixed, MacCormack's explicit method is the more advantageous overall.

#### DERIVATION OF MACCORMACK'S EXPLICIT METHOD

Recall the two-dimensional Navier-Stokes equations derived earlier:

$$\frac{\partial \bar{u}}{\partial t} + \xi_x \frac{\partial \bar{F}}{\partial \xi} + \eta_x \frac{\partial \bar{F}}{\partial \eta} + \xi_y \frac{\partial \bar{G}}{\partial \xi} + \eta_y \frac{\partial \bar{G}}{\partial \eta} = \bar{0} \quad (3.4)$$

where:

$$\bar{U} = \begin{bmatrix} \rho \\ \rho u \\ \rho v \\ \rho e \end{bmatrix} \quad (3.4a)$$

$$\bar{F} = \begin{bmatrix} \rho u \\ \rho u^2 - \sigma_{11} \\ \rho uv - \tau_{12} \\ \rho ue - \frac{1}{PrRe} \frac{\partial T}{\partial x} - u\sigma_{11} - v\tau_{12} \end{bmatrix} \quad (3.4b)$$

$$\bar{G} = \begin{bmatrix} \rho v \\ \rho uv - \tau_{12} \\ \rho v^2 - \sigma_{22} \\ \rho ve - \frac{1}{PrRe} \frac{\partial T}{\partial y} - u\tau_{12} - v\sigma_{22} \end{bmatrix} \quad (3.4c)$$

MacCormack's method states that, if the solution  $U^n_{i,j}$  is known at time  $t = n \Delta t$  at each point in the mesh, then at time  $t = (n+1)\Delta t$  the solution can be described as:

$$U^{n+1}_{i,j} = \mathcal{L}(\Delta t) U^n_j \quad (3.5)$$

where  $\mathcal{L}(\Delta t)$  defines these operations:

$$\begin{aligned} U^{n+\frac{1}{2}}_{i,j} &= U^n_{i,j} - \frac{\Delta t}{\Delta x} (F^n_{i,j} - F^n_{i-1,j}) - \frac{\Delta t}{\Delta y} (F^n_{i,j} - F^n_{i,j-1}) \\ U^{n+1}_{i,j} &= \frac{1}{2} \left[ U^n_{i,j} + U^{n+\frac{1}{2}}_{i,j} - \frac{\Delta t}{\Delta x} (F^{n+\frac{1}{2}}_{i+1,j} - F^{n+\frac{1}{2}}_{i,j}) \right. \\ &\quad \left. - \frac{\Delta t}{\Delta y} (F^{n+\frac{1}{2}}_{i,j+1} - F^{n+\frac{1}{2}}_{i,j}) \right] \end{aligned} \quad (3.6)$$

An example of the application of MacCormack's explicit method is shown by considering the computation of density:

$$\rho^{n+1}_{i,j} = \mathcal{L}(\Delta t) \rho^n_{i,j} \quad (3.7)$$

Now we write Equation 3.7 in terms of its components:

$$\rho^{n+\frac{1}{2}}_{i,j} = \rho^n_{i,j} - \frac{\Delta t}{\Delta x} \left[ (\rho u)^n_{i,j} - (\rho u)^n_{i-1,j} \right] - \frac{\Delta t}{\Delta y} \left[ (\rho u)^n_{i,j} - (\rho u)^n_{i,j-1} \right] \quad (3.8a)$$

$$\rho_{i,j}^{n+1} = \frac{1}{2} \left[ \rho_{i,j}^n + \rho_{i,j}^{n+\frac{1}{2}} - \frac{\Delta t}{\Delta x} \left\{ (\rho u)_{i,j}^{n+\frac{1}{2}} - (\rho u)_{i,j}^{n+\frac{1}{2}} \right\} - \frac{\Delta t}{\Delta y} \left\{ (\rho u)_{i,j+1}^{n+\frac{1}{2}} - (\rho u)_{i,j}^{n+\frac{1}{2}} \right\} \right] \quad (3.8b)$$

Note that:

$$\rho_{i,j}^{n+1} = f \left[ (\rho u)_{i,j}^n, (\rho u)_{i+1,j}^{n+\frac{1}{2}}, (\rho u)_{i,j+1}^{n+\frac{1}{2}}, \dots \right] \quad (3.9)$$

Thus, the two computations should proceed simultaneously.

#### TRUNCATION ERROR OF MACCORMACK'S EXPLICIT METHOD

The truncation error of MacCormack's explicit method is second order, as mentioned earlier. This is true only of the combined form:

$$u_{i,j}^{n+1} = \frac{1}{2} \left[ u_{i,j}^n + u_{i,j}^n - \frac{\Delta t}{\Delta x} (F_{i,j}^n - F_{i-1,j}^n) - \frac{\Delta t}{\Delta y} (F_{i,j}^n - F_{i,j-1}^n) - \frac{\Delta t}{\Delta x} (F_{i,j+1}^{n+\frac{1}{2}} - F_{i,j}^{n+\frac{1}{2}}) - \frac{\Delta t}{\Delta y} (F_{i,j+1}^{n+\frac{1}{2}} - F_{i,j}^{n+\frac{1}{2}}) \right] \quad (3.10)$$

By themselves, the predictor and corrector are only first order accurate. The use of backward space differencing in the predictor and forward space differencing in the corrector (or vice versa; as long as the directions are different) allow the method to achieve second order accuracy.

#### STABILITY OF MACCORMACK'S EXPLICIT METHOD

The stability of MacCormack's explicit method has not been analytically demonstrated yet. According to MacCormack ((9:3) and (9:152-154)), some insight could be derived from approximations. For instance, one could linearize the Navier-Stokes equations and then study the amplification of Fourier components of the solution (9:152). Alternatively, one could examine three separate parts of the Navier-Stokes equations (inviscid, viscous, and mixed derivatives) and

find stability conditions for each part (9:3). MacCormack did postulate stability criteria as follows:

$$\Delta t = \frac{\Delta x}{|u| + c + \frac{1}{\rho} \left( \frac{2 \gamma \mu}{Pr \Delta x} + \sqrt{\frac{\gamma \mu}{\Delta y}} \right)} \quad (3.11)$$

This condition is usually called the Courant-Friedrich-Levy (CFL) condition. The implementation of MacCormack's method in NONISOCODE uses a form of the CFL condition computed at each streamwise strip for different  $\Delta y$ 's which ignores the viscous contributions. The implementation in NONISOCODE is also in transformed coordinates, so that its form is somewhat different from that of Eq. 3.11.

## CHAPTER IV: PROGRAM DESCRIPTION

### OVERVIEW

This chapter will discuss the two primary codes used in this study, NONISOCODE and STEADY. Each code will be discussed in some detail. Listings of both programs can be found in the Appendix A.

### NONISOCODE

The Navier-Stokes simulation code used in this study, NONISOCODE, is a derivative of a code written by Dr J. S. Shang et al at the Flight Dynamics Laboratory (AFWAL/FIM), Wright-Patterson AFB, Ohio. A copy of the program listing is found in Appendix A. This section will describe the major parts of NONISOCODE and discuss special features in the code developed for this study.

#### Program Overview

NONISOCODE is a two-dimensional Navier-Stokes simulation designed for use with super- or hypersonic flows. It uses MacCormack's explicit method to compute flow quantities and includes a pressure damping subroutine to allow damping of Gibbs phenomena. The code from which NONISOCODE was adapted was originally designed to analyze three-dimensional flow problems; the basic structure of NONISOCODE still

reflects this. The original program was designed to compute flow conditions for an axial 'page' and then sum all the 'pages' together for a three-dimensional flow solution. This structure facilitated vectorization of the code for parallel processor computers; however, it does run on 'scalar' machines as well. NONISOCODE only computes two-dimensional flows, but still retains the three-dimensional structure; thus, flow variables will be written as  $P(K,J,l)$ . The inclusion of the unitary third dimension reflects the actual two-dimensional nature of the problem. A brief discussion of each subroutine follows.

#### Subroutine MAIN

This portion of NONISOCODE is the executive. It accepts input values, directs most subroutine calls, and outputs results. There are three output files. The first is used to restart the computation from a given point in time. This is done because a converged solution generally requires about 40,000 iterations; most computer operating systems have much lower time limits than implied by that number. The second output file is tied to this restart capability. In order to get a quick look at the state of the computed flow field, this output file holds the most important flow variables at each point in the field: density, velocity components, pressure, temperature, and turbulent eddy viscosity. In addition, there is a list of surface condi-

tions for each grid point along the surface. The final file is a graphical output file which is designed to interface with several common graphics packages. This file contains velocity components, temperature, pressure ratios, Mach number, and density for each grid point in the field.

#### Subroutine EDDY

This subroutine computes the eddy viscosity matrix for the flow field using the Baldwin-Lomax viscosity model. However, since wind tunnel tests have shown that the flow over the wedges modeled is laminar, this subroutine is superfluous and is bypassed. Subroutine MAIN loads zero values into the eddy viscosity matrix and does not call EDDY.

#### Subroutine PREAMB

PREAMB is used to establish the initial conditions for the solution of the Navier-Stokes equations. PREAMB establishes the freestream flow field over the entire computational domain, thus giving an impulsive start to the solution. As will be discussed later, the initial conditions at the upstream boundaries permit the use of a wedge angle. There is a provision for three points in the freestream to allow the fourth-order damping routine to operate in the stagnation region. The surface initial conditions are no-slip. The downstream boundary is nonreflec-



tive, allowing waves to pass out. None of the other boundaries are; this can be a cause of many problems if the grid is improperly designed.

#### Subroutine TMSTEP

TMSTEP computes the CFL condition required for stability of the solution. The CFL condition is computed for each space step in a streamwise row of grid points. The minimum time step in each row is selected and compared to other minimum time steps in the grid from the surface to the far-field boundary. The minimum CFL condition is then chosen as the CFL condition for the entire flow field. It is then multiplied by an input CFL factor (always less than one) to guarantee numerical stability. A CFL factor is required because the CFL condition only guarantees neutral numerical stability and because the diffusion terms weren't included. From this description, it can be seen that such a scheme is inefficient with grids that are irregular or are highly stretched. The minimum CFL condition will be based on the smallest space step but will drive the integration step size for the largest space step. Consequently, the solution will slow down proportionally. This was the case in this study; the grid used is semi-adaptive and exponentially stretched in the normal direction. The CFL condition will be based on space step sizes near the wall, while space steps at the far field boundary are an order of magnitude larger.

#### Subroutine BC

This subroutine sets the boundary conditions for the solution. It is called for each iteration. The surface boundary condition is the classical no-slip boundary condition; this prevents the investigation of possible slip flow in the stagnation region of the wedge. All inflow boundary conditions are Dirichlet boundary conditions where the values of the flow properties are specified. The outflow boundary (downstream) uses Neumann boundary conditions, where the gradients of the flow properties are zero. Thus, all inflow boundaries do not permit waves to reflect from them (which isn't physically correct and can cause numerical problems); having a shock wave impinge on the far-field boundary, for instance, is a sure way to bomb the solution. The downstream boundary does permit waves to be absorbed and not reflected; a shock can 'exit' the downstream boundary and not affect the solution. The use of Dirichlet boundary conditions for inflow boundaries (upstream and far-field) specify the minimum height of the normal grid; it must be higher at the trailing edge than any waves that might impinge.

#### Subroutine TRANS

TRANS is used to transform the physical coordinate system into a regular, rectangular grid for computation. A generalized transformation is derived using the chain rule

(assuming that a transformation exists, i.e., the Jacobian of the transformation is nonzero and positive). The transformation scale factors (derivatives) are approximated using second order central differences. The output from TRANS is a transformed grid matrix of scale factors used in all subsequent computations.

Subroutines PAGE, LETA(J), LZETA(J), SUM

This set of subroutines represents the application of MacCormack's explicit method to the solution of the two-dimensional Navier-Stokes equations. PAGE is a holdover from the original three-dimensional version of the code; it is essentially a controller for the following subroutines. LETA(J) computes the flow derivatives with respect to the streamwise transformed coordinate eta; LZETA(J) does the same with respect to the transformed normal coordinate zeta. SUM(J) sums both of those sets of derivatives for a final solution. SUM(J) also calls the final subroutine, when appropriate.

Subroutine DAMPING

DAMPING is used to control the generation of Gibb's phenomena (oscillations) in the solution. The type of pressure damping used is an artificial viscosity. Although the Mach number modeled is quite high, the pressure damping required turned out to be rather low, on the order of 0.4.

## SPECIAL FEATURES

Two special features were incorporated into NONISOCODE in order to analyze the nonisothermal wall. The first is the incorporation of the wedge angle. The original code from which NONISOCODE was adapted could only consider axisymmetric, zero angle flows. In order to perform this study, wedge angles had to be included in subroutines PREAMB and BC. In those subroutines, the velocity components  $U$  and  $V$  were replaced by  $U \cos \delta$  and  $-U \sin \delta$ . Once the wedge angle is included in PREAMB and BC, the flow solution will include it from then on.

The other special feature included in NONISOCODE was the ability to enter a step in wall temperature at any point along the surface of the wedge. This required two modifications. The first was a major change in some of the logic in PREAMB and BC. The step in wall temperature was included with IF statements that keyed on where along the surface the solution was. Before a certain point,  $T_w$  would be  $T_{w1}$ ; after that point,  $T_{w2}$ . The second modification installed a key, KG, which corresponds to the station of the wall temperature discontinuity, in the input files and the code. Thus, a user can set  $T_{w1}$ ,  $T_{w2}$ , and KG to whatever is desired; the wall temperatures can be the same (as was done in this study for the isothermal wedge) or, for the same effect, KG can specify the trailing edge of the surface. Or,

as was done for the nonisothermal portion of the study, the discontinuity can be placed anywhere on the surface. In order to preserve the generality of the code,  $T_{w1}$  and  $T_{w2}$  are specified in separate statements that determine  $T_w$ , which is then used.

### STEADY

STEADY is the heat transfer code developed specifically for this study. It is a simple code, but it does incorporate some interesting points. A listing of STEADY can be found in Appendix A.

STEADY is designed to read the restart files of NONISO-CODE and extract the field temperature from them. It then computes the reference convective heat transfer coefficient to be used to nondimensionalize the convective heat transfer coefficient. The convective heat transfer coefficient is then computed. Again, the change in wall temperature is accounted for (if the wedge is nonisothermal; if not, an input value bypasses those lines). The coefficient of viscosity is computed based on the wall temperature. Thermal conductivity thus includes the varying wall temperature.

One particularly interesting aspect of STEADY is the way the partial derivative of temperature with respect to normal distance is computed.  $T_y$  must be computed in the transformed plane to maintain second order accuracy. As

noted before,  $T_y$  can be represented as:

$$\frac{\partial T}{\partial y} = \eta_y \frac{\partial T}{\partial \eta} + \xi_y \frac{\partial T}{\partial \xi} \quad (4.1)$$

Due to the physical grid used,  $\eta = 0$ . Thus,  $T_y$  is now represented as:

$$\frac{\partial T}{\partial y} = \frac{\partial T / \partial \eta}{\partial y / \partial \eta} \quad (4.2)$$

This derivative can be computed as the quotient of two three-point, one-sided differences with respect to eta. Those differences are second order accurate.

There are two output files. The first prints a listing of  $X/L$ , reference convective heat transfer coefficient, local convective heat transfer coefficient, and the nondimensional ratio  $H/H_{ref}$ . The second output file is a listing of  $X/L$  and  $H/H_{ref}$  for use in plotting.

Convergence is determined by comparing the convective heat transfer coefficient between NONISOCODE runs, which are usually 2000 iterations apart. If the percent difference between the two convective heat transfer coefficients is less than 2%, the solution is considered to have converged. The difference between isothermal and nonisothermal convective heat transfer coefficients is determined in essentially the same fashion. The equation used is:

$$\left( \frac{A_{new} - A_{old}}{A_{old}} \right) \times 100\% = \text{Difference} \quad (4.3)$$

## CHAPTER V: RESULTS

### OVERVIEW

This chapter will discuss the results of the numerical simulation of the isothermal and nonisothermal wedges. There will be a brief discussion of the limitations of the results, due primarily to the analytical technique used. The heat transfer solution for both the isothermal and the nonisothermal surfaces will be discussed. The flow field conditions at convergence will be described. The presence of shock wave-boundary layer interaction will be discussed briefly, also. Its possible effect on the solution will be considered. Finally some peculiarities of the NONISOCODE solution will be discussed

### FLOW CONDITIONS

Both the isothermal and nonisothermal wedges were modeled under the same conditions. The freestream Mach number was 14.24 and the freestream stagnation temperature was 2000 deg R. As a result, the freestream static temperature is only 48.13 deg R and the freestream static pressure is only 0.4981 lbs/sq ft. The speed of sound is 340 ft/sec. The wedges were modeled with a three degree deflection angle, the lowest angle discussed in Cappelano (1:14). These conditions guarantee that boundary layer gradients will be quite steep and the stagnation area conditions severe. The surface temperatures were as follows. For the

isothermal wedge, the surface was considered to be at a uniform temperature of 540 deg R. The nonisothermal wedge had a leading edge temperature of 540 deg R and a trailing edge temperature (after the discontinuity) of 700 deg R.

#### LIMITATIONS OF THE RESULTS

The chief limitation in this study is the size of the streamwise integration step,  $\Delta x$ . Considerable time was spent on determining and applying the correct distribution of normal grid points. This was necessary in order to sufficiently resolve the temperature inversion layer in the region of interest near the discontinuity. In the course of that investigation, it was found that NONISOCODE did not handle a highly stretched grid well; in fact, if the exponential stretch factor,  $Q$ , exceeded about -0.15, this particular problem wouldn't run at all. That is due to a combination of the grid and the particular initial conditions (high Mach number, steep gradients, etc.). Due to the time spent on the normal grid, there was insufficient time to properly investigate the streamwise grid distribution. Because a discontinuity in surface temperature is being investigated, it would be desirable to have a high concentration of grid points in the vicinity of the discontinuity. In fact, at one point, a double exponential stretch was considered, with the first stretch in the normal direction



and the second extending both up- and downstream from the discontinuity. However, the limitations of NONISOCODE and the lack of time available forced the use of a constant grid distribution in the streamwise direction. Thus, the solution in the immediate vicinity of the discontinuity suffers from truncation error and subsequent 'smearing'. As will be noted later, this effect can be seen in the plots of the nonisothermal convective heat transfer coefficient.

Another limitation to the results to be discussed is the modeling of the leading edge. When the normal grid distribution was established, it was determined that a semi-adaptive grid would be used, one that grew in relation to the growth of the boundary layer. It was desired to maintain about ten points in the boundary layer to sufficiently resolve the temperature inversion. The profile that the grid was based on was at  $X/L = 0.2$ . This was done in order to escape the direct effects of the shock wave-boundary layer interaction and the stagnation region and to avoid a more stringent stability criterion. As a result, from  $X/L = 0$  to  $X/L = 0.2$ , the normal grid distribution is constant and will not necessarily contain enough points in the boundary layer to accurately model the temperature inversion. When heat transfer is computed, the partial derivative  $\partial T / \partial y$  is computed using three point, one-sided differences in  $\partial T / \partial y$  and  $\frac{\partial y}{\partial \eta}$ . This requires at least three points inside the temperature inversion to approximate the slope. Those points are

not guaranteed prior to  $X/L = 0.2$ . Thus, no results are presented for the leading edge region; the numbers would be inaccurate and misleading.

Another point to consider in interpreting the results is the format in which the results are presented. Strictly speaking, this isn't a limitation, but it is important to correctly interpreting the results. Consider Figures 4 and 5; they are representative surface and contour plots, respectively. Note that in Figure 4, the data appears to stop along a parabolic curve, nowhere near the apparent far-field boundary shown in the plot. In fact, the parabolic curve is the far-field boundary of the computational domain, as explained earlier. The appearance of the plot is an artifact of the plotting program, DISPLAA. DISPLAA only recognizes a rectangular grid, so that data presented for the parabolic semi-adaptive grid shows up superimposed on a zero-value rectangular background.

The same effect is visible in Figure 5, the representative contour plot. Here, the edge of the computational domain is shown by a very close clustering of contours, showing the drop from free-stream values to an artificial zero value. In both cases, the zero-value data had to be inserted to allow DISPLAA to plot the semi-adaptive grid results. As a beneficial side effect, the presence of the zero-value data serves to constantly highlight the shape of the physical computational domain.

## HEAT TRANSFER SOLUTIONS

The first results to be discussed are the heat transfer solutions. Figure 3 is a plot of the nondimensionalized convective heat transfer coefficients for the isothermal and the nonisothermal surfaces and experimental data from Hodge et al (2:8, 10). Nondimensionalization was accomplished by ratioing the dimensional convective heat transfer coefficients to a reference convective heat transfer coefficient described earlier. Hodge's data was already nondimensionalized in the same fashion; the only correction that needed to be made was to shift his data points downstream to account for the presence of three grid points in the freestream ahead of the leading edge in this study.

Consider first the isothermal convective heat transfer coefficient, plotted as a solid line in Figure 3. It is fairly constant about the value  $h/h_{ref} = 1.741$  for the region from  $X/L = 0.2$  to  $X/L = 0.9$ . There is only a 3.4% variation from this value over this range. Note that the ratio does tend to trail off somewhat towards the trailing edge of the wedge. The theoretical value for an isothermal  $h/h_{ref}$  is constant; the variation shown is probably due to truncation error in the computations.

The nonisothermal  $h/h_{ref}$  is shown by the dotted line in Figure 3. Up to about  $X/L = 0.42$ , the nonisothermal and the isothermal values are identical, which is to be expected. At  $X/L = 0.42$ , the nonisothermal curve begins to oscillate

somewhat in the immediate vicinity of the temperature discontinuity on the wedge. Immediately thereafter,  $h/h_{\text{ref}}$  plummets to 0.64 and then recovers slowly to values about 17% below the isothermal values. This difference between the isothermal and the nonisothermal values after the discontinuity is expected due to the higher temperature of the trailing edge's surface, 160 deg R hotter than for the isothermal wall.

The slow recovery of the nonisothermal  $h/h_{\text{ref}}$  is due in part to truncation error 'smearing' the convective heat transfer coefficient. However, some of the lag in recovery is due to the axial diffusion of energy. Within the scope of this study, it is impossible to separate the contributions of truncation error and axial diffusion to the  $h/h_{\text{ref}}$  recovery lag; it is, however, clear that axial diffusion of energy is occurring, that the nonisothermal wall effect is present. The lack of recovery indicates that some of the energy is being convected downstream and is consequently reducing the local convective heat transfer.

Hodge's experimental data are also presented in Fig. 3. The isothermal data is for a thin stainless steel plate (2:2, 5); the nonisothermal data is for an FRSI test sample (2:2, 6). The isothermal data, plotted as +s, shows a close correlation with the isothermal Navier-Stokes prediction, with only a 2.3% average variation from the computed data over the trailing edge portion of the plate. The

agreement is best for the first five points; as the trailing edge is approached, the experimental data diverges slightly. The reason for this divergence is unknown. There are only three data points available for the nonisothermal FRSI test article. Fig. 3 shows these points, plotted as O's, reflecting the same trend of recovery after the discontinuity as the Navier-Stokes prediction. The magnitudes of the computed and experimental convective heat transfer coefficients match fairly well for the first and third experimental points; the middle experimental point is well off the computed curve. The reason for this disagreement is unknown. Note, however, that the behavior of the two computed curves and the isothermal thin-skin points is similar; they all seem to have a "hump" between  $X/L = 0.6$  and  $X/L = 0.75$ .

Finally, note that the behavior of the computed and experimental curves is quite different. The computed isothermal and nonisothermal curves tend to follow on another after the discontinuity, allowing for the 17% difference. The slope and shape of the two curves are quite similar. The isothermal and nonisothermal experimental curves do not tend to mirror one another. As noted above, the nonisothermal data tends to approach the isothermal data as the trailing edge of the wedge is approached. Indeed, the last values show only a 7.6% difference between them. It has been suggested, in another context, that what is

happening in the experimental data near the trailing edge is a three-dimensional effect. While there is very little concrete evidence to go on in this study, it is safe to say that the experimental and computed nonisothermal values near the trailing edge are in fairly close agreement. This would seem to mitigate against any three-dimensional effects.

#### FLOW FIELD SOLUTIONS

Results of NONISOCODE simulations are plotted in Figures 4 through 27. The results for the isothermal wall are shown in Figures 4 through 15; the nonisothermal wall in Figures 16 through 27. The surface plots for pressure and density clearly show the leading edge shock wave. The shock angle is in the vicinity of 6 degrees, agreeing with theory. The pressures behind the shock are about 50% higher than predicted by Rankine-Hugoniot shock jump equations; this is due to the shock wave-boundary layer interaction. Behind the shock, outside of the boundary layer, the freestream static temperature is close to the 64.95 deg R predicted by Rankine-Hugoniot theory. As these examples show, NONISOCODE has done a good job of modeling the flow field. One interesting point is the size of the temperature inversion. The surface plots of temperature, Figures 10 and 22, show the inversion clearly defined by the ridge near the bottom edge of the plot. It can be seen that the inversion is only about 0.0096 ft tall (about 0.1 in). This is a very small

region for such a large temperature rise.

Another interesting point is the surface pressure distribution. Figure 28 shows the isothermal and nonisothermal surface pressure distributions, as well as a theoretical Rankine-Hugoniot line. The analytical curves are identical prior to  $X/L=0.6$ , but after the flow crosses the thermal discontinuity, the nonisothermal surface pressure experiences a pressure spike of about 0.2 lbs/sq ft. The spike occurs about  $3/4$  inch (0.0632 ft) behind the discontinuity. After this spike, the nonisothermal surface pressure decays in a similar fashion to the isothermal surface pressure, but at a value about 4% above it.

The pressure spike can be explained in terms of the thermal boundary layer. At the discontinuity, the surface temperature jumps from 540 deg R to 700 deg R; this will cause a corresponding increase in the thickness of the thermal boundary layer. When this "bloom" occurs, compression waves are generated in the flow field. Assuming that the Mach cone for these compression waves is centered at the edge of the boundary layer at the discontinuity, the Mach angle (defined as the inverse sine of the reciprocal of the edge Mach number) is a little greater than 4 degrees. The compression wave will impinge the surface of the wedge about 0.6 inches behind the discontinuity. Referring to Figure 28, it can be seen that this is where the pressure spike occurs. The actual calculated point of impingement is at  $X/L$

= 0.69564; the computed pressure spike occurs at  $X/L = 0.6681$ . This 4% discrepancy can be explained by the fact that, as the compression wave goes deeper into the boundary layer, flow Mach number decrease rapidly and the compression wave is "bent back", causing the wave to impinge slightly ahead of the predicted point.

The Rankine-Hugoniot line at the bottom of the plot shows the theoretical downstream pressure; if traditional boundary layer assumptions had been applied, this  $v$  value would also represent the surface pressure behind the shock. It serves to demonstrate the effect of the shock wave-boundary layer interaction; the predicted pressure behind the shock is significantly lower than the computed (and actual) pressure due to the interaction of the shock wave and boundary layer.

In general, the flow field solutions for the isothermal and nonisothermal wedges are quite comparable, with the obvious difference of the temperature discontinuity. Both solutions are accurate models of the real flow field. With the agreement between model and reality demonstrated, the heat transfer results can be considered as accurately modeling the physical situation.

#### SHOCK WAVE-BOUNDARY LAYER INTERACTIONS

An interaction of the bow or leading edge shock wave and the boundary layer is a phenomenon that will occur in



most hypersonic aerodynamics problems. Its presence in this problem was not unexpected. The presence of the interaction affects the flow field solution and the heat transfer. The discussion that follows is based on the work of Dorrance (11:144-148). It should be noted that no effort was made to analyze in depth the shock wave-boundary interaction; rather, the presence of the interaction was observed, its strength calculated, and a qualitative overview of its effects was made.

When an object is moving at hypersonic speeds, the displacement thickness is much larger than for the same object at slower speeds. This is due to the higher temperatures found in a hypersonic boundary layer. The larger size of the displacement thickness means that the effective shape of the body is changed to include the displacement thickness. At the leading edge, the flow is turned sharply away from the surface; this turning gives rise to a series of compression waves that coalesce into a shock. The very presence of the shock affects the growth of the boundary layer. This interaction is the shock wave boundary layer interaction.

The strength of this interaction can be estimated by computing an interaction factor  $\bar{\chi}$ , defined as:

$$\bar{\chi} = (C^{1/2} M^3) / Re^{1/2} \quad (5.1)$$

where  $C = \rho \mu / (\rho_e \mu_e)$  (5.2)

If this interaction factor is greater than 1, then the effects of shock wave-boundary layer interaction must be accounted for. In the current problem,  $\bar{\chi}$  at the leading edge has a value of about 20.2; it drops off to a value of 2.65 at the trailing edge of the wedge.  $\bar{\chi}$  is greater than 1 and the interaction must be considered. Referring again to Fig. 28, the presence and magnitude of the interaction can be seen by comparing the analytical pressure curves with the theoretical line. Near the leading edge, the computed pressure is about 50% greater than the theoretical value. Further downstream, this difference decreases to about 20%.

#### NUMERICAL OSCILLATIONS

When examining the surface plots in Figures 4 through 27, it is very easy to see oscillations in the plots for streamwise velocity, temperature, and, to a lesser extent, Mach number and density. These oscillations, seen most easily in the surface plots for streamwise velocity, have one probable origin.

The most probable explanation is that the oscillations are artifacts of the plotting process. This determination comes from the nature of DISPLAA, the program used to generate the plots. The version of DISPLAA used requires a rectangular grid to plot its data. If the data are presented in a non-rectangular format, DISPLAA uses a nine-

point linear average interpolating scheme to interpolate the data to a rectangular grid. This problem did not use a rectangular grid, and the results are presented in the semi-adaptive grid format. Thus, DISPLAA has interpolated the data to fit its own grid. Now the oscillations are most apparent in the streamwise velocity surface plots and the temperature surface plots. The gradients here from the surface to the freestream are, in absolute terms, the most severe encountered in the entire solution. The next most severe gradients are to be found in the temperature solution, partly because temperature is dependent on flow velocity. Realizing that the data is interpolated and realizing that the most severe gradients are present in the plots where the oscillations are most apparent lead directly to the argument that those oscillations are artifacts of DISPLAA and are enhanced by steep gradients.

A point to buttress this argument is that the oscillations do not show up in the data. An investigation of the raw data plotted shows no oscillations of the kind seen in the surface plots. Also, the oscillations do not show up in the contour plots. Thus, it is improbable that the oscillations have any other cause.

## CHAPTER VI: CONCLUSIONS AND RECOMMENDATIONS

### OVERVIEW

This chapter will discuss conclusions and recommendations derived from the study. Conclusions regarding the numerical methods used and concerning the nonisothermal wall effect will be discussed. Recommendations for further study and possible methods will be presented.

### CONCLUSIONS

#### NONISOTHERMAL WALL EFFECT

This study has demonstrated that the nonisothermal wall effect can be modeled using a two-dimensional Navier-Stokes simulation. The nonisothermal wall effect manifests itself as an 'incomplete' recovery in the nonisothermal convective heat transfer coefficient after the temperature discontinuity on the wedge surface. The actual magnitude of the nonisothermal wall effect was not determined due to numerical 'smearing' caused by truncation error; however, there is no doubt that the nonisothermal wall effect was modeled by NONISOCODE. Additionally, it has been shown that the numerical results agree closely with experimental results; differences can be explained by the lack of axial resolution in the region of the thermal discontinuity.

A subsidiary conclusion that can be drawn is that

NONISOCODE adequately models hypersonic flow over wedges. This is, of course, a necessary condition for the proper simulation of the nonisothermal wall effect. The temperature inversion layer and the axial diffusion of heat energy at the thermal discontinuity are correctly modeled by NONISOCODE .

#### SHOCK WAVE-BOUNDARY LAYER INTERACTION

It has been shown that a shock wave-boundary layer interaction did occur and did have observable effects on the computed solution. The 20% to 50% increase in surface pressure over theoretical predictions is in general agreement with Nagamatsu and Sheer.

#### PRESSURE SPIKE DUE TO NONISOTHERMAL WALL

The observed pressure spike is a real phenomenon that is probably a result of the nonisothermal wall effect. Its probable cause is the impingement of a compression wave on the surface of the wedge. The compression wave, in turn, is probably generated by the sudden, almost discontinuous growth of the momentum and thermal boundary layers at the discontinuity. This pressure spike may be a distinguishing characteristic of the nonisothermal wall effect, and might be used to signal its existence.

#### NUMERICAL METHODS

The numerical methods used in this study were adequate

to properly model the nonisothermal wall effect. MacCormack's explicit method was appropriate to the problem. The grid chosen was appropriate to the problem, with two specific exceptions (to be addressed below). In particular, the use of a semi-adaptive grid that grows (in the normal direction) with the boundary layer was essential to the success of the study. This grid permitted the investigation of the temperature inversion in the boundary layer while allowing shock and Mach waves to escape the downstream boundary without excessive stretching.

The method used to compute the convective heat transfer coefficient was entirely appropriate; the use of three-point, one-sided finite differences in the transformed plane for  $\partial T / \partial y$  retained second order accuracy. The method used to determine convergence is simple and straight-forward, but it adequately demonstrates convergence of temperature, the figure of merit for this study.

There were, however, some significant problems with the numerical methods used. The most significant problem was the choice of grid. The use of a regularly-distributed grid in the streamwise direction simplified computations but it also induced numerical error in the stagnation region and in the vicinity of the temperature discontinuity. The solution in the stagnation region suffered because the grid did not allow resolution of the stagnation region. A similar problem occurred at the discontinuity. The problem is more

serious here because the lack of resolution coupled with the existence of the discontinuity induces a significant truncation error. Thus, the less-than-total convective heat transfer coefficient recovery is, in part, an artifact of the truncation error. While the recovery does demonstrate the nonisothermal wall effect, it is impossible to determine the magnitude of the effect in this study.

Another problem that is of lesser significance is the exclusive use of the three-point, one-sided finite difference to model the partial derivative of temperature with respect to normal distance. While this finite difference worked quite well for  $X/L > 0.4$ , it is unreliable for the area near the leading edge. This is due to the decreasing number of points in the temperature inversion. It is possible that using a two-point, one-sided finite difference near the stagnation region would yield valid results, although at the cost of numerical accuracy. Exclusively using the three-point, one-sided finite difference denied investigation of the convective heat transfer coefficient near the leading edge.

#### RECOMMENDATIONS

There are several recommendations that result from this study. The first is that the nonisothermal wall effect needs more study. This effort has shown that it is possible to accurately model the nonisothermal wall effect; it has

also demonstrated that there are several shortcomings in the methods used. More study needs to be done in order to correctly model all aspects of the nonisothermal wall effect and to determine its magnitude.

Closely tied to the first recommendation is the second, which is the use of a more appropriate grid for modeling the nonisothermal wall effect. Although this study showed that the inviscid portion of the hypersonic flow can be modeled with a fairly coarse grid, the stagnation region and the temperature discontinuity require a much finer, specialized grid. In particular, the grid should employ dual stretching: the normal distribution must be stretched in order to include the temperature inversion, while the streamwise distribution must stretch at the stagnation point and at the discontinuity. The stretching at the discontinuity should be both up- and downstream to capture the true character of the nonisothermal wall effect.

The use of such a grid will raise problems with NONISOCODE. During the study, several variants of stretched grids were tried; very few worked. The reason for all the failures is unknown; however, it became apparent that NONISOCODE in its present form cannot use highly stretched grids (with a stretching exponent much greater than  $Q = -0.15$ ). Whether this is due to the transformation from the physical to the transform plane or to the implementation of MacCormack's method or to some other source is unknown. That



aspect requires more investigation.

A further recommendation is to further investigate numerically the shock wave-boundary layer interaction and how it affects the nonisothermal wall effect. The interaction has a tendency to increase the surface pressure downstream of the shock and can influence the heat transfer characteristics of the flow. The grid used did not allow sufficient resolution of the stagnation region or the region about the thermal discontinuity. A different grid will need to be used to investigate this problem.

A final recommendation is to further study the pressure spike that is seen to occur downstream of the discontinuity. It is possible that this spike is a distinguishing characteristic of the nonisothermal wall effect. Further investigation could show whether or not the pressure spike can signal the presence of a nonisothermal wall effect.

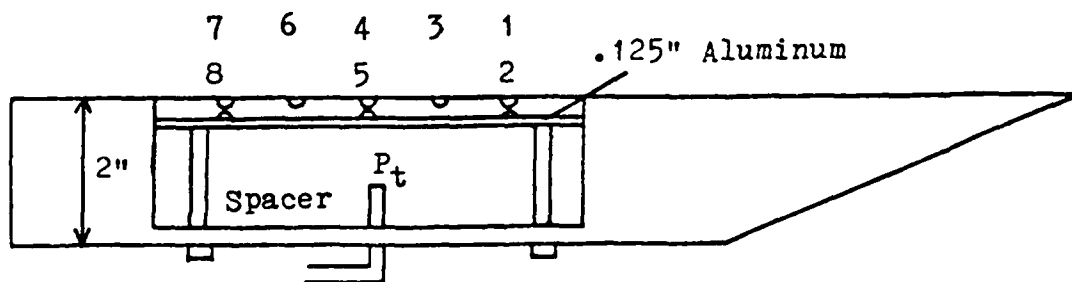
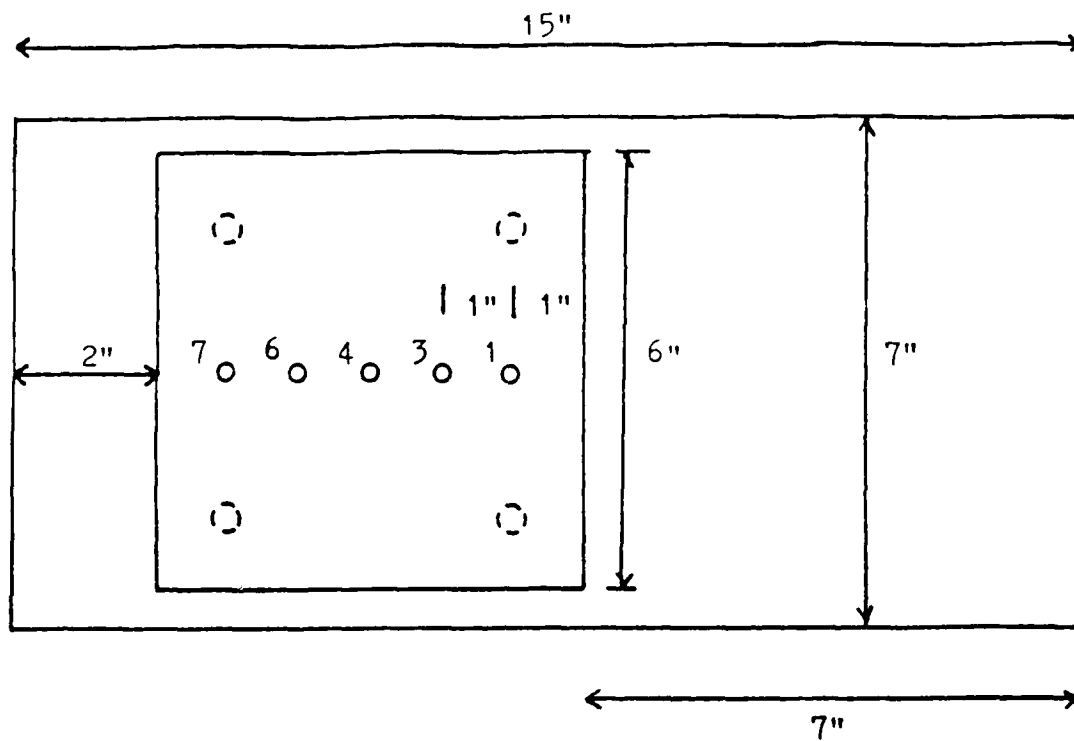


Fig. 1: Test Article

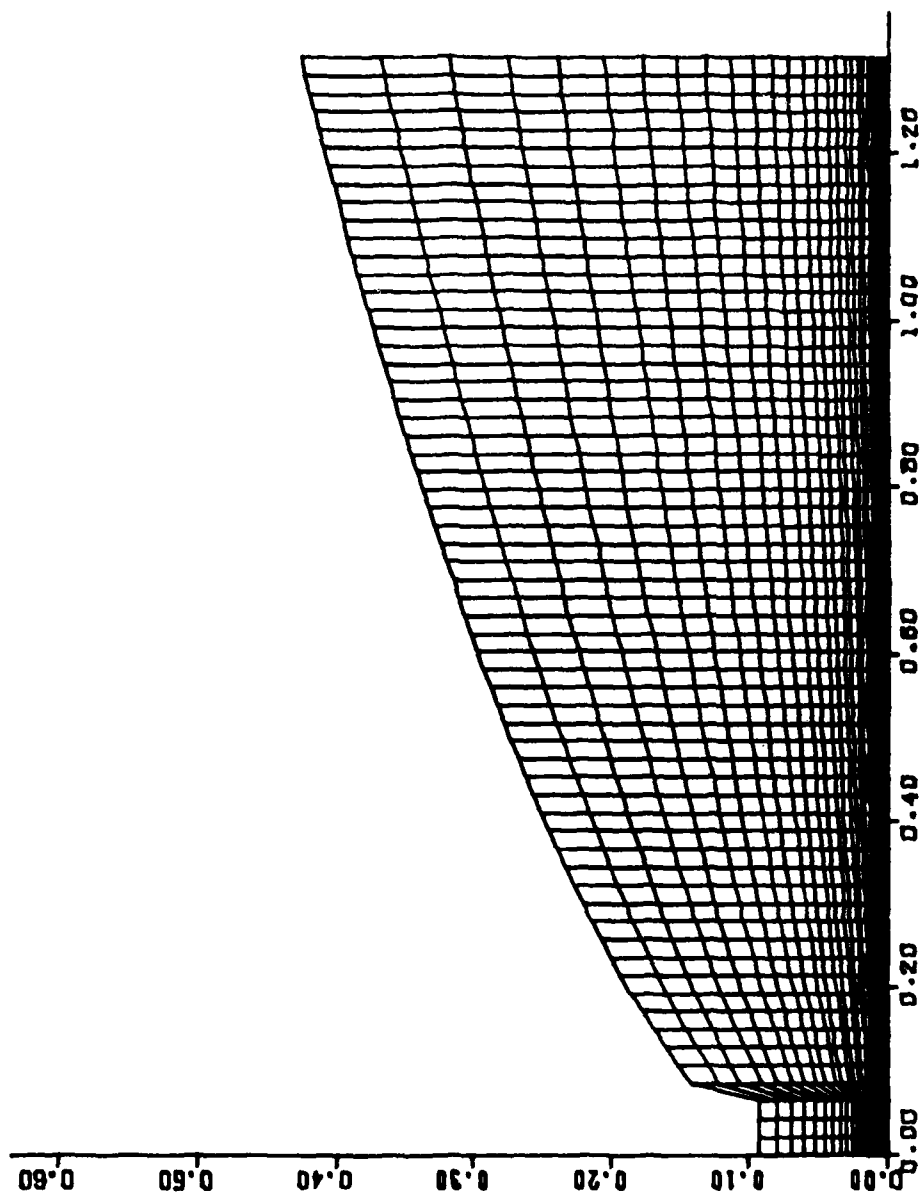


Fig. 2: Semi-Adaptive Physical Grid

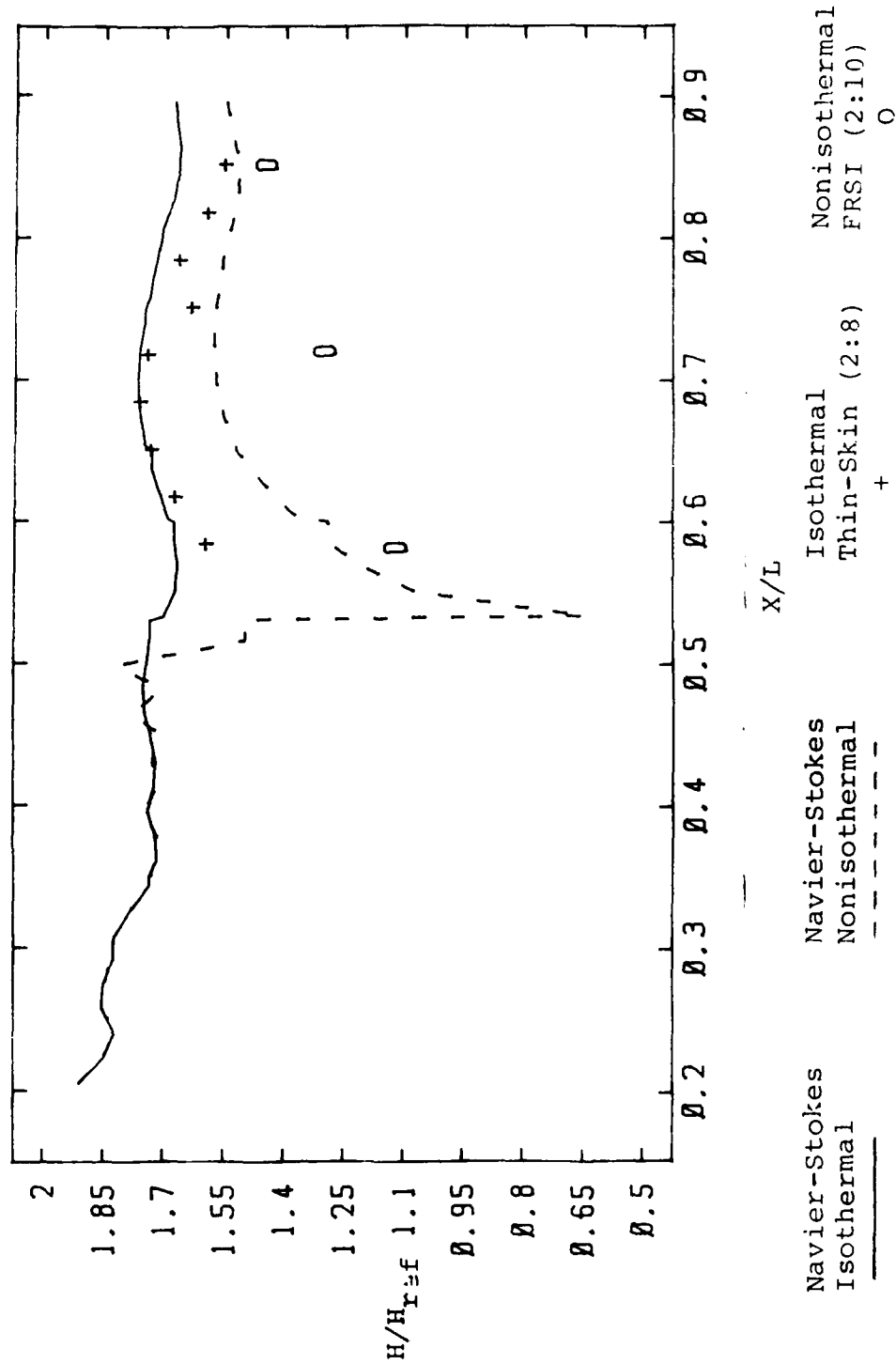


Fig. 3: Nondimensional Convective Heat Transfer Coefficient

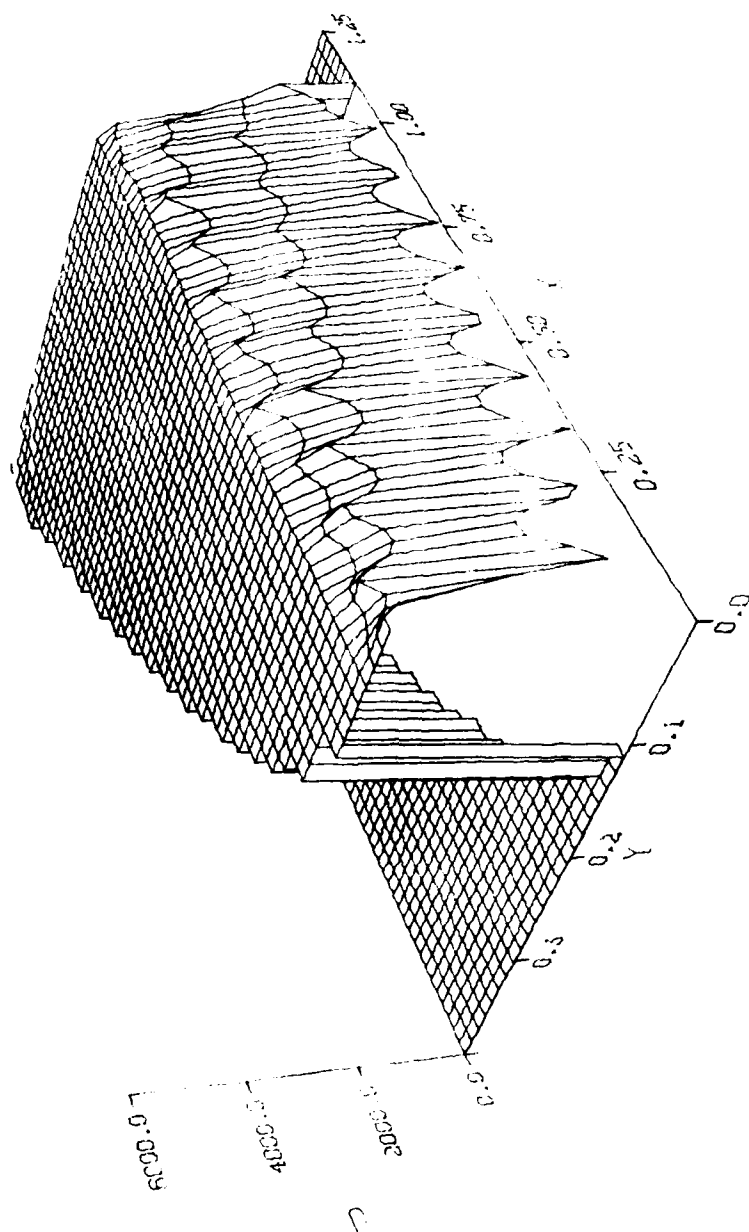


Fig. 4: Isothermal Streamwise Velocity Surface

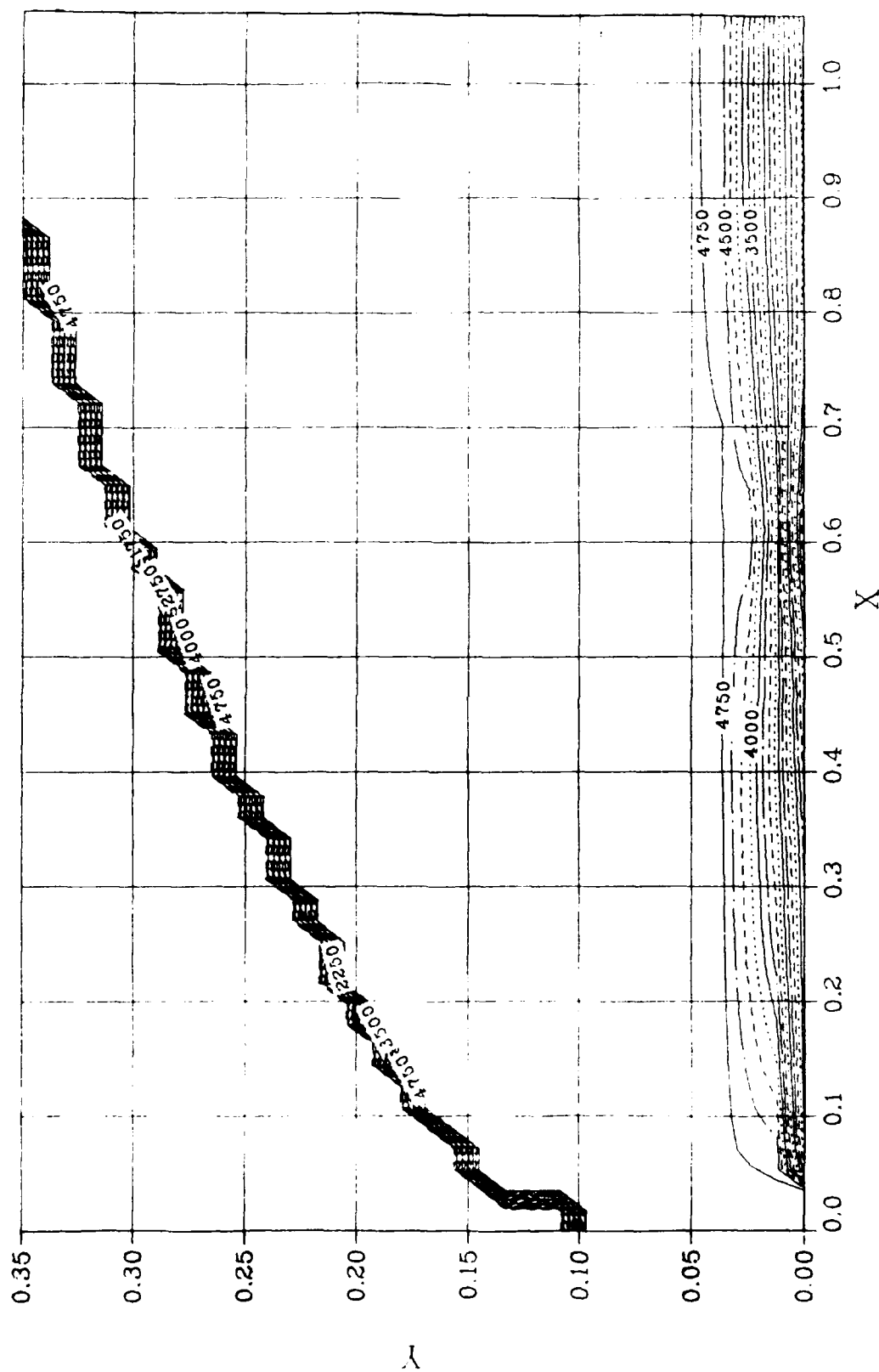


Fig. 5: Isothermal Streamwise Velocity Contours

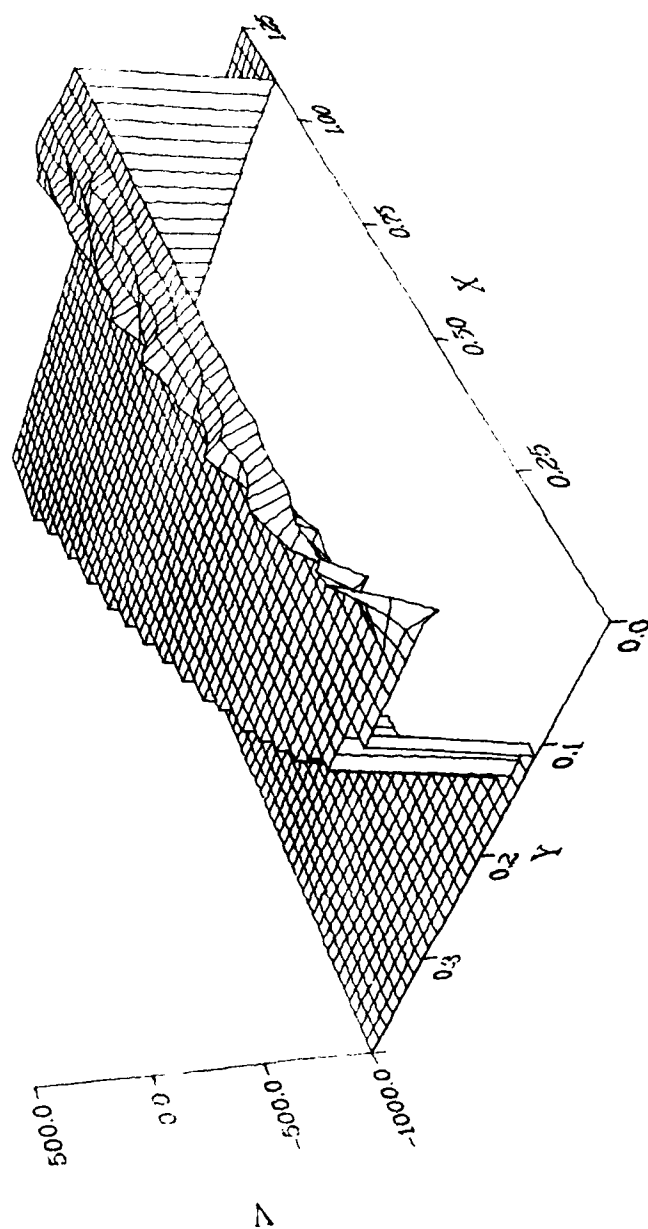


Fig. 6: Isothermal Normal Velocity Surface

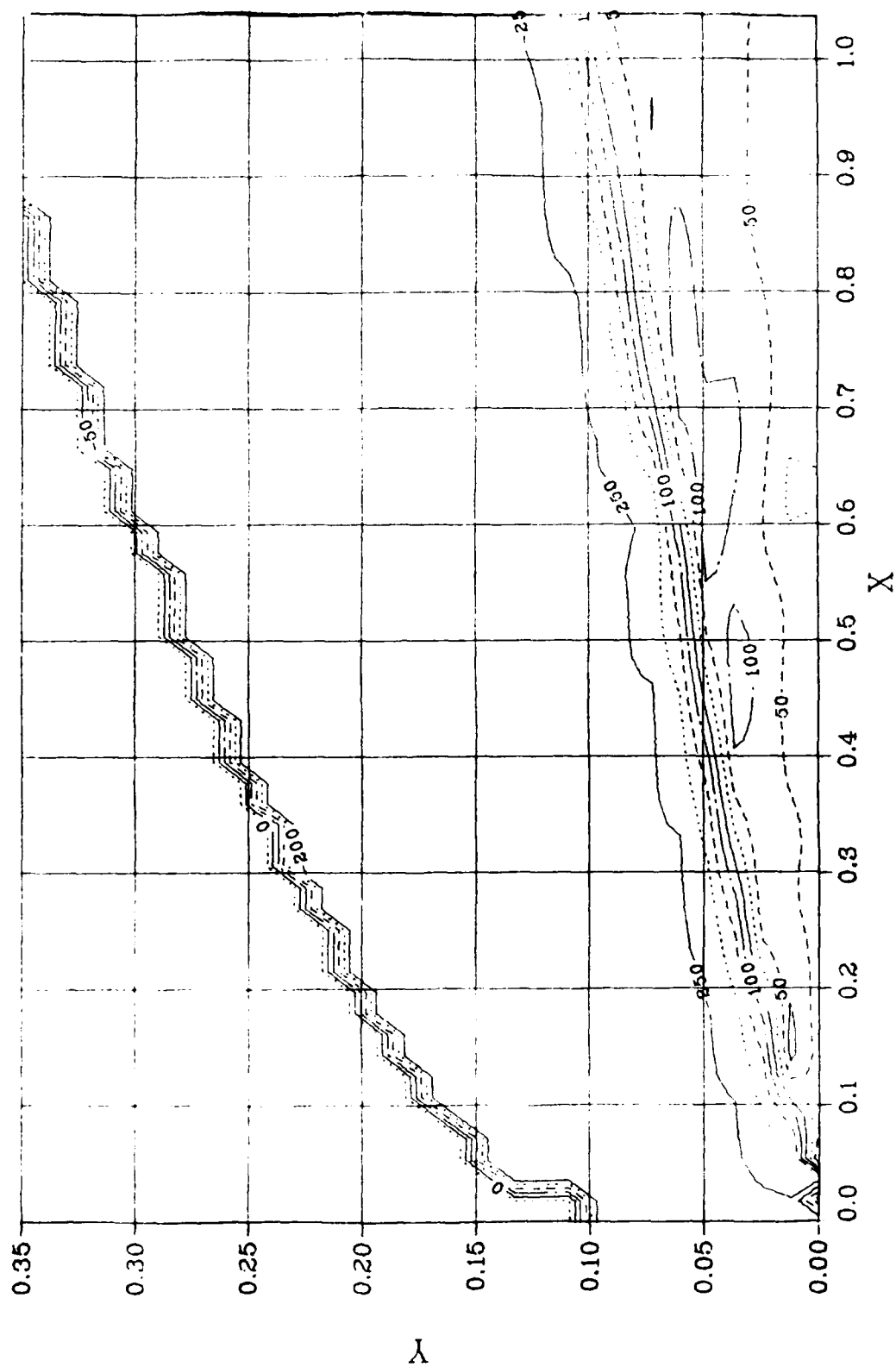


Fig. 7: Isothermal Normal Velocity Contours



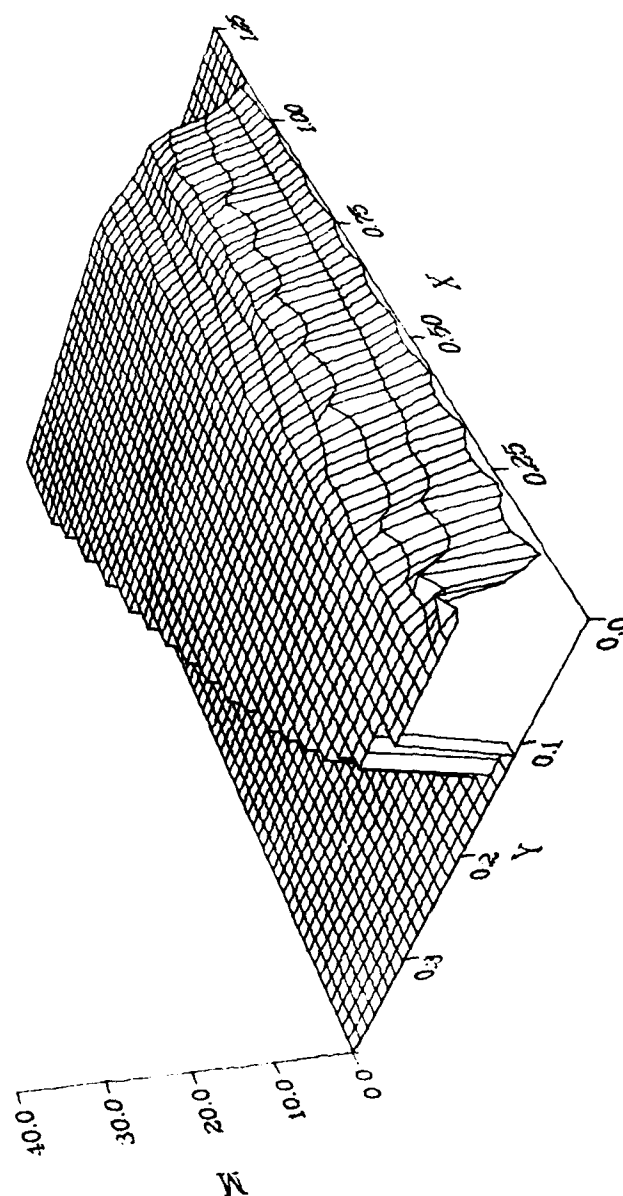


Fig. 8: Isothermal Mach Number Surface

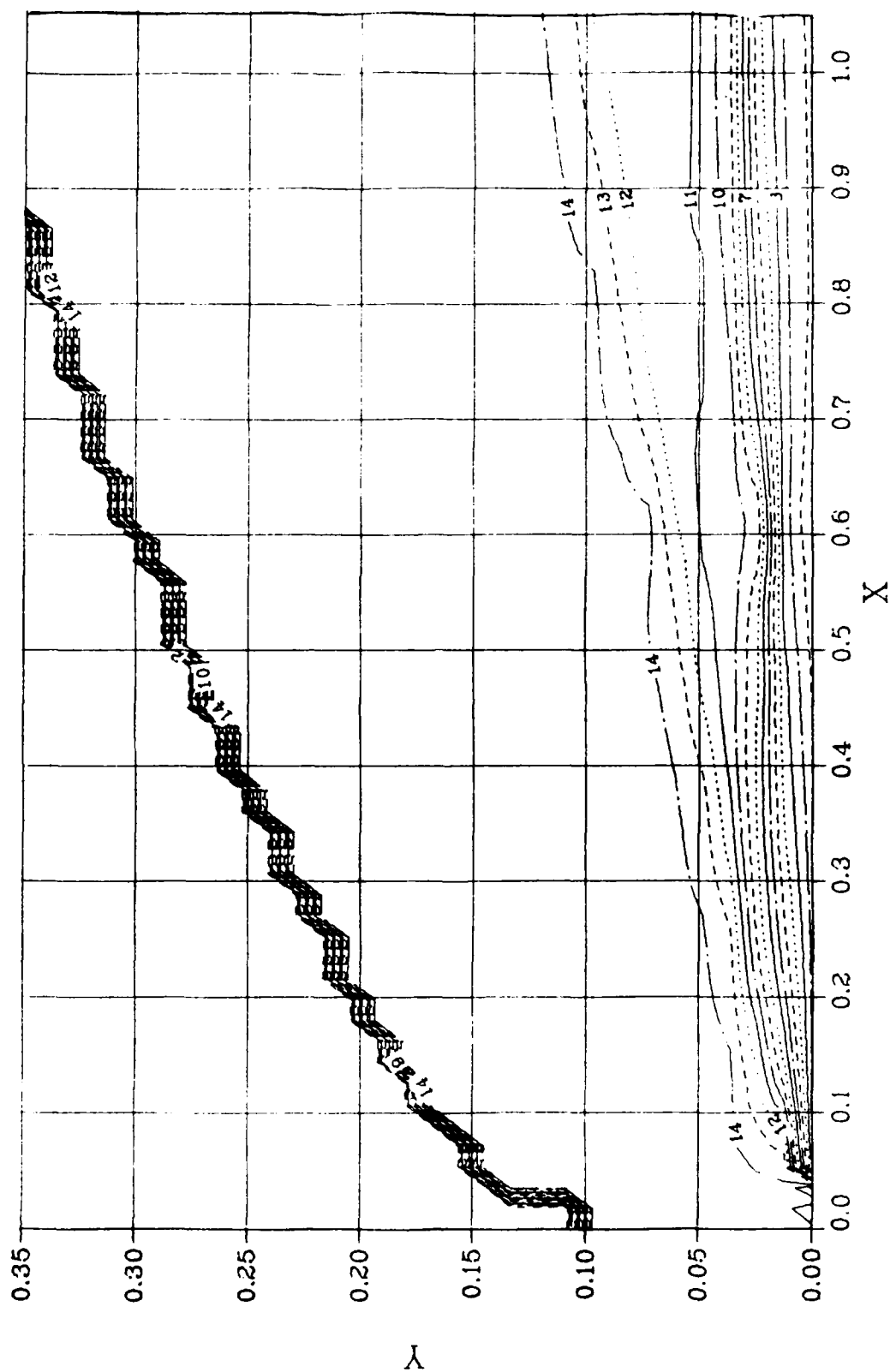


Fig. 9: Isothermal Mach Number Contours

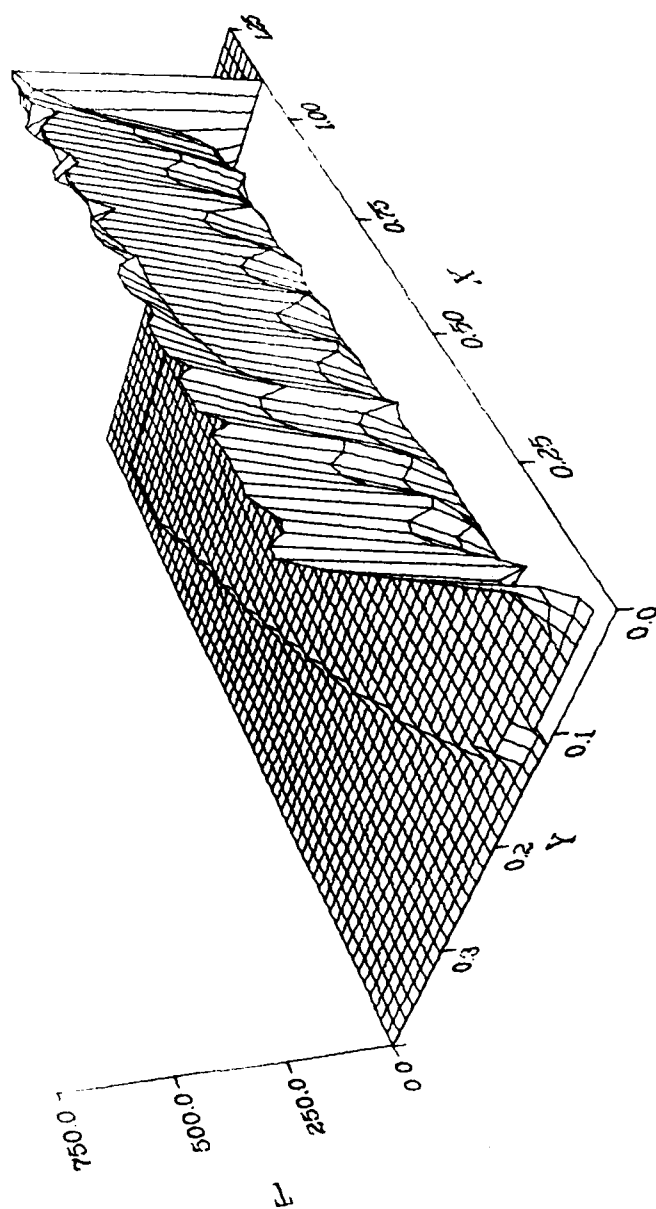


Fig. 10: Isothermal Temperature Surface

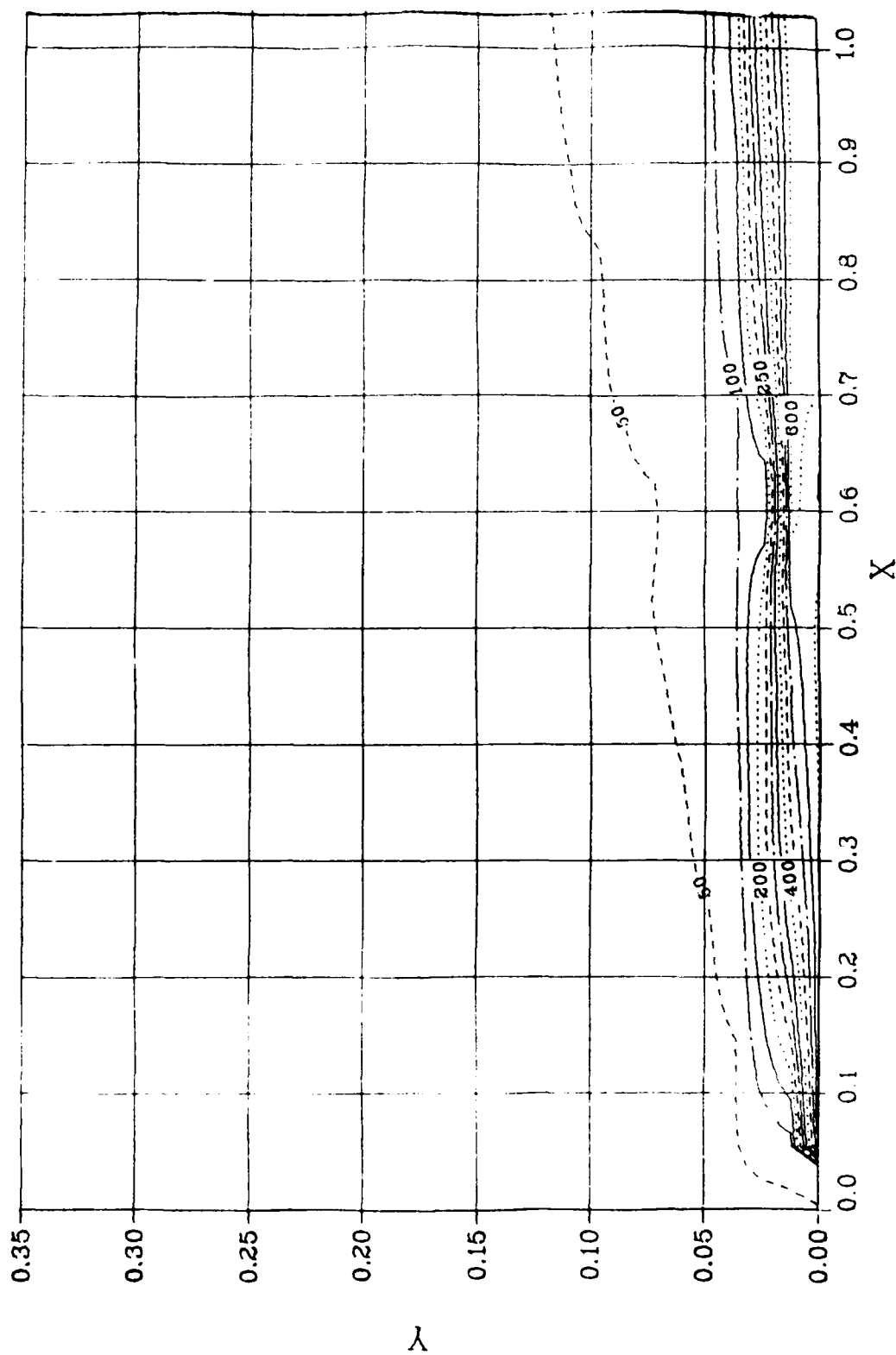


Fig. 11: Isothermal Temperature Contours

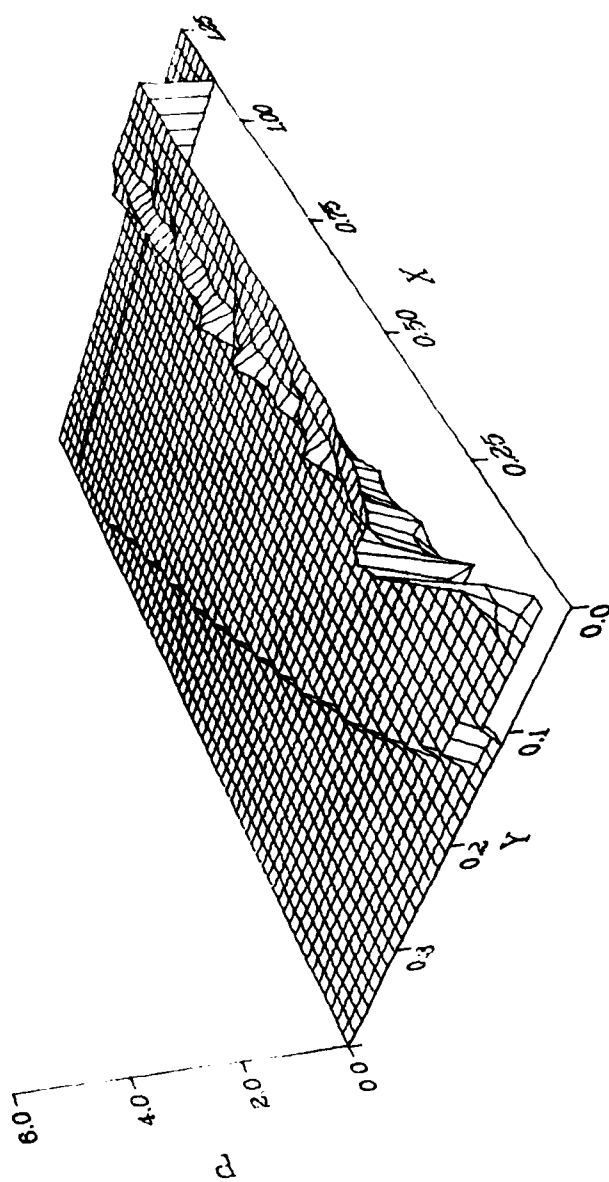


Fig. 12: Isothermal Pressure Surface

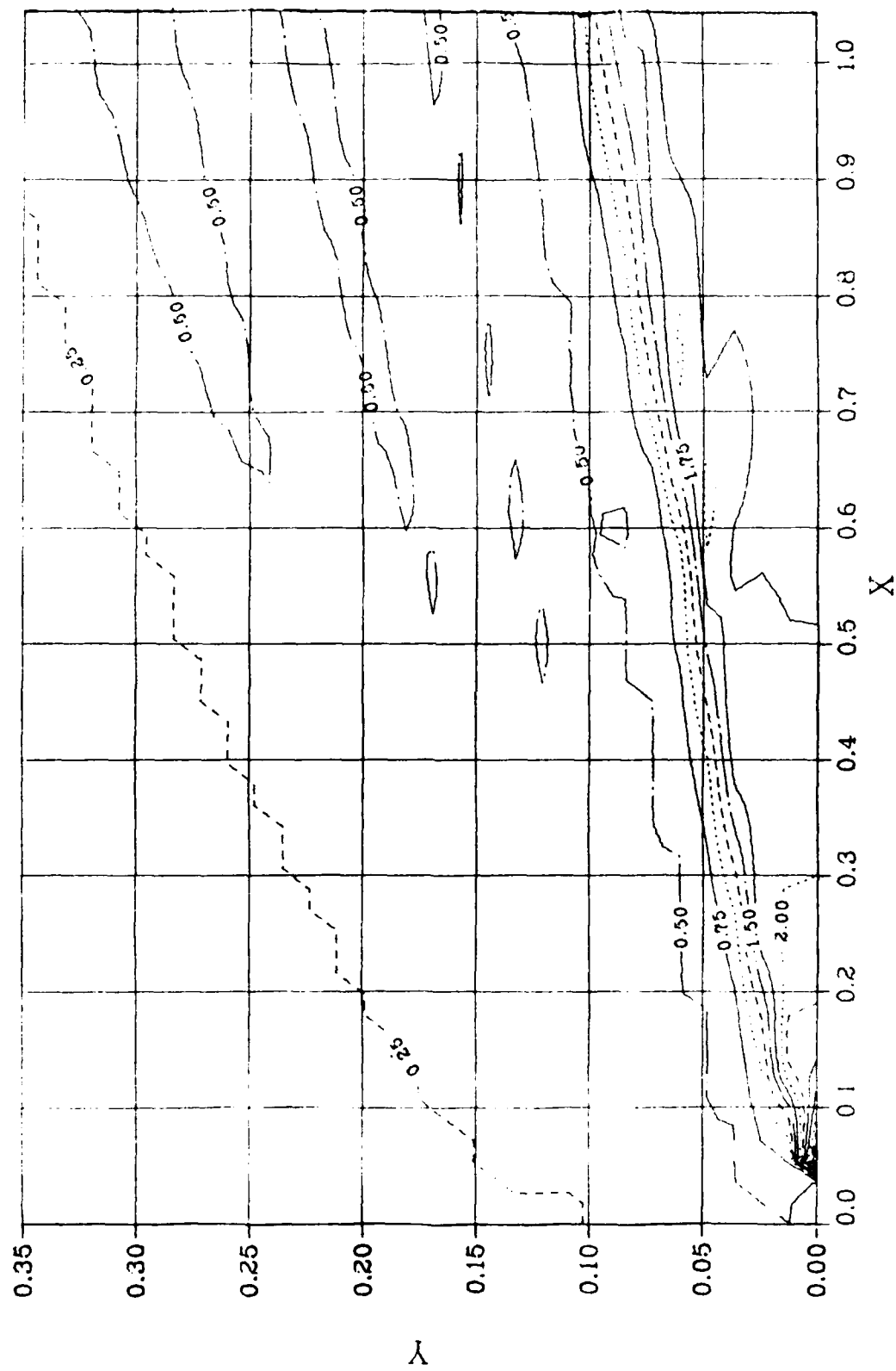


Fig. 13: Isothermal Pressure Contours

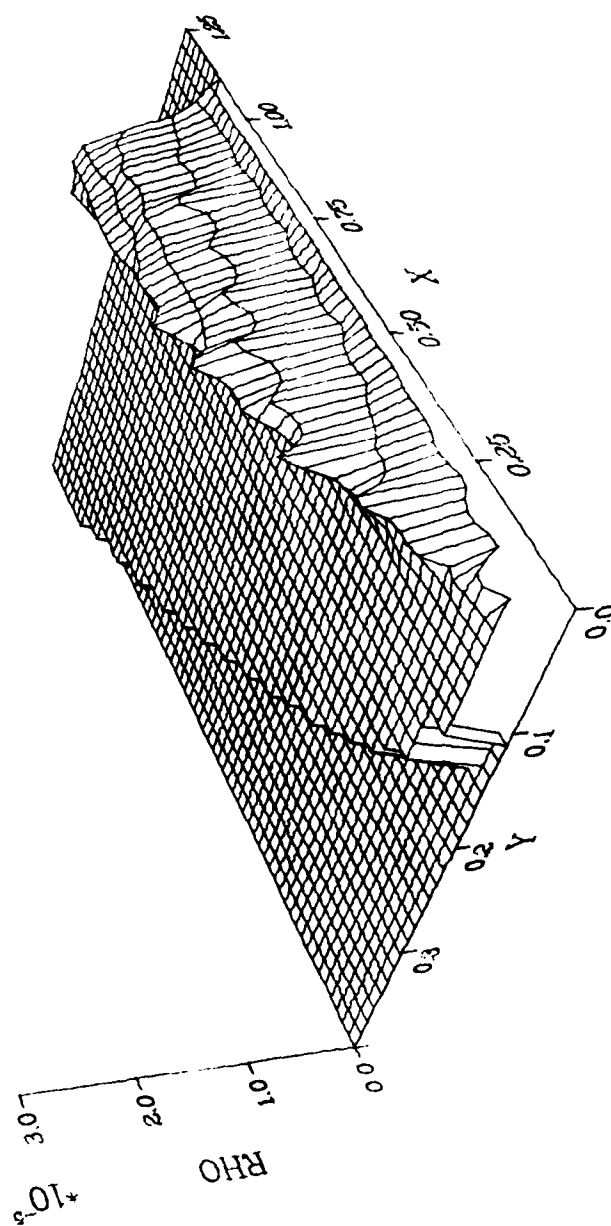
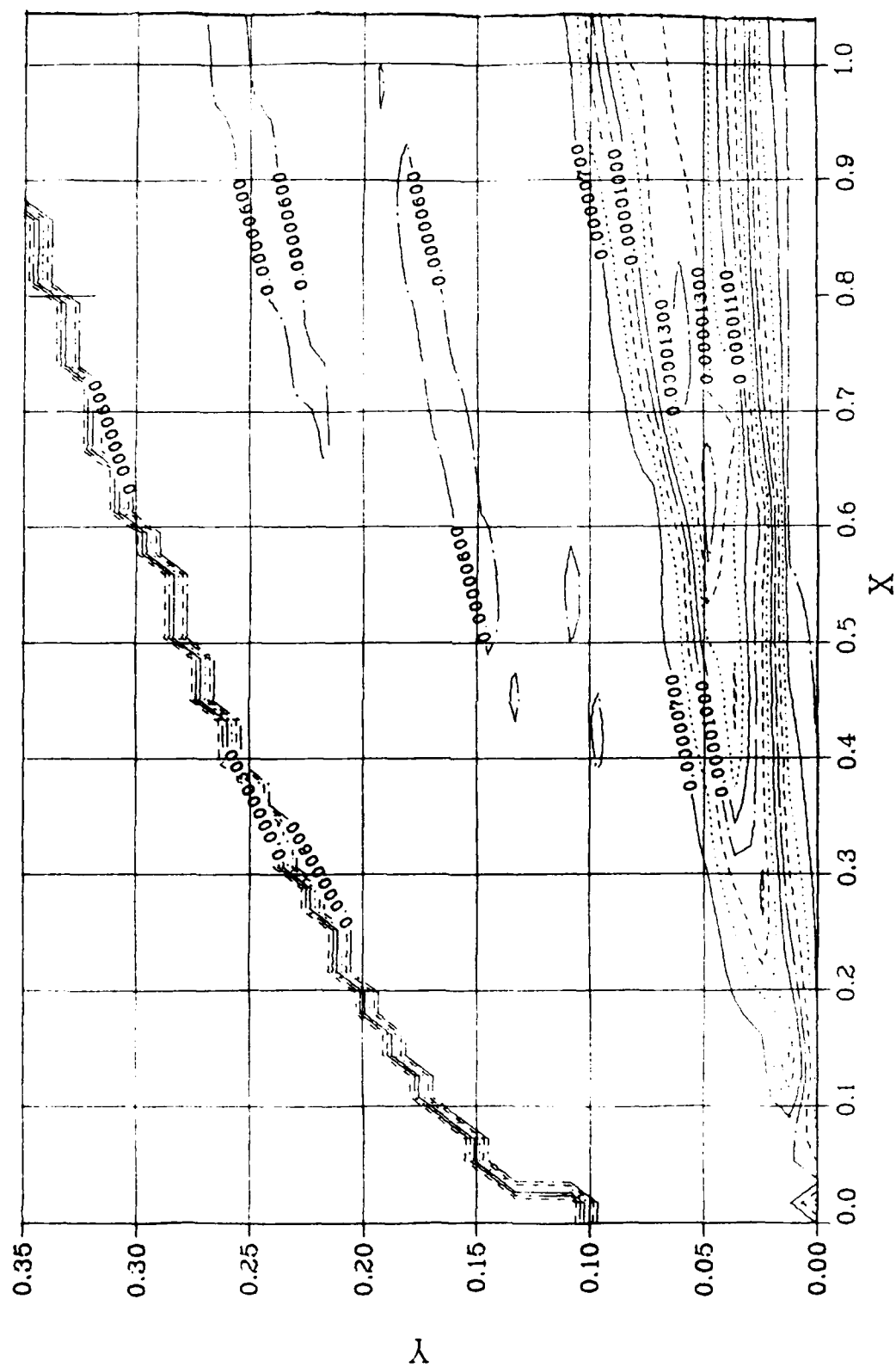


Fig. 14: Isothermal Density Surface





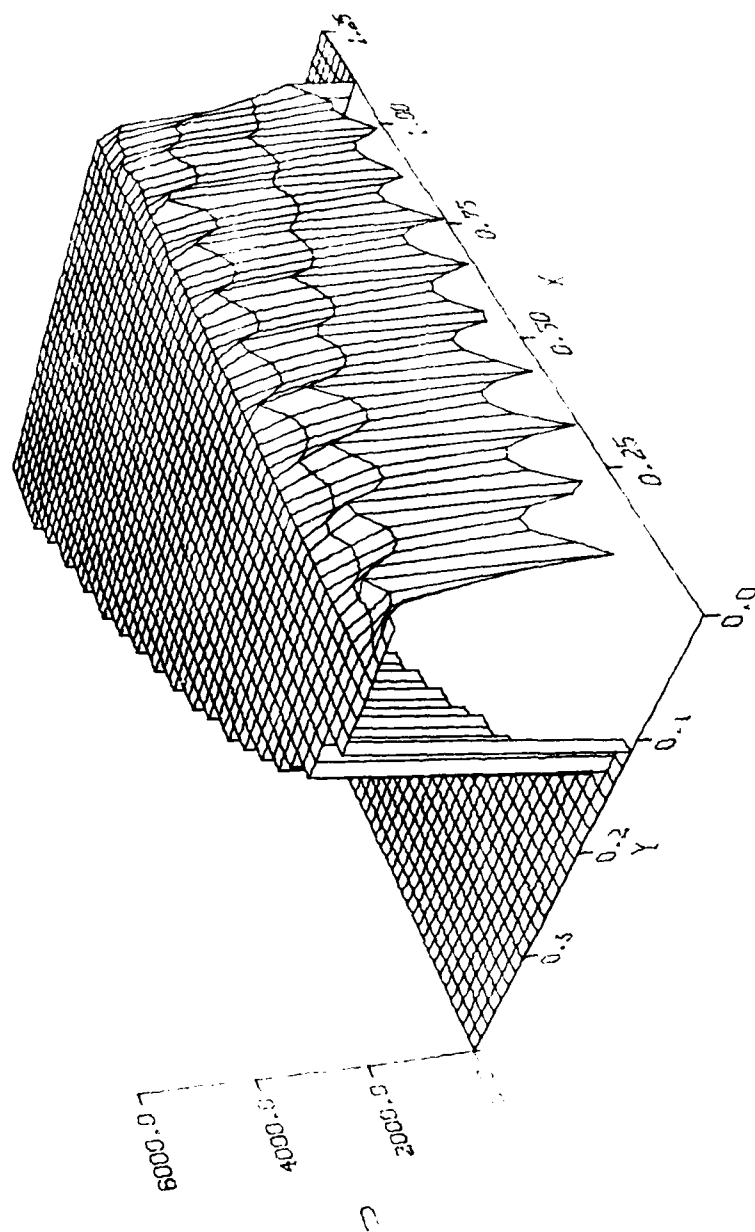


Fig. 16: Nonisothermal Streamwise Velocity Surface

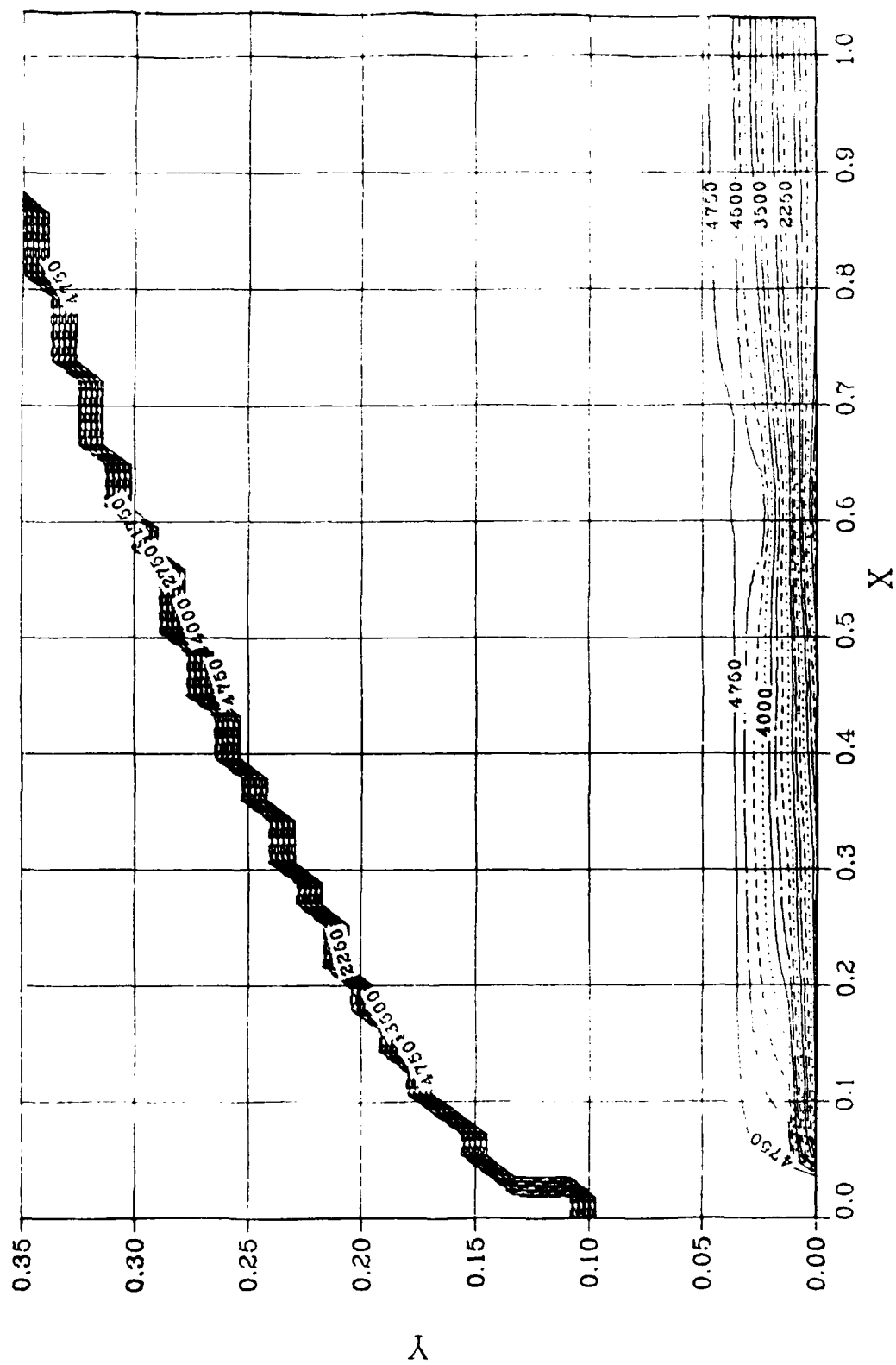


Fig. 17: Nonisothermal Streamwise Velocity Contours

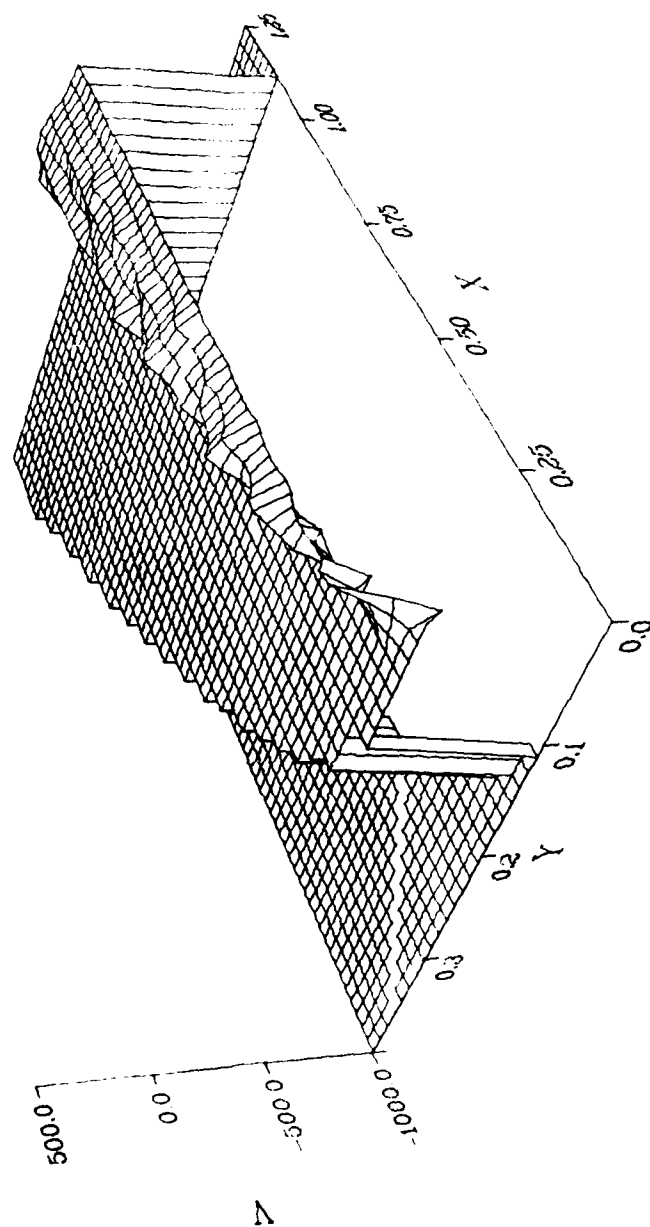


Fig. 18: Nonisothermal Normal Velocity Surface

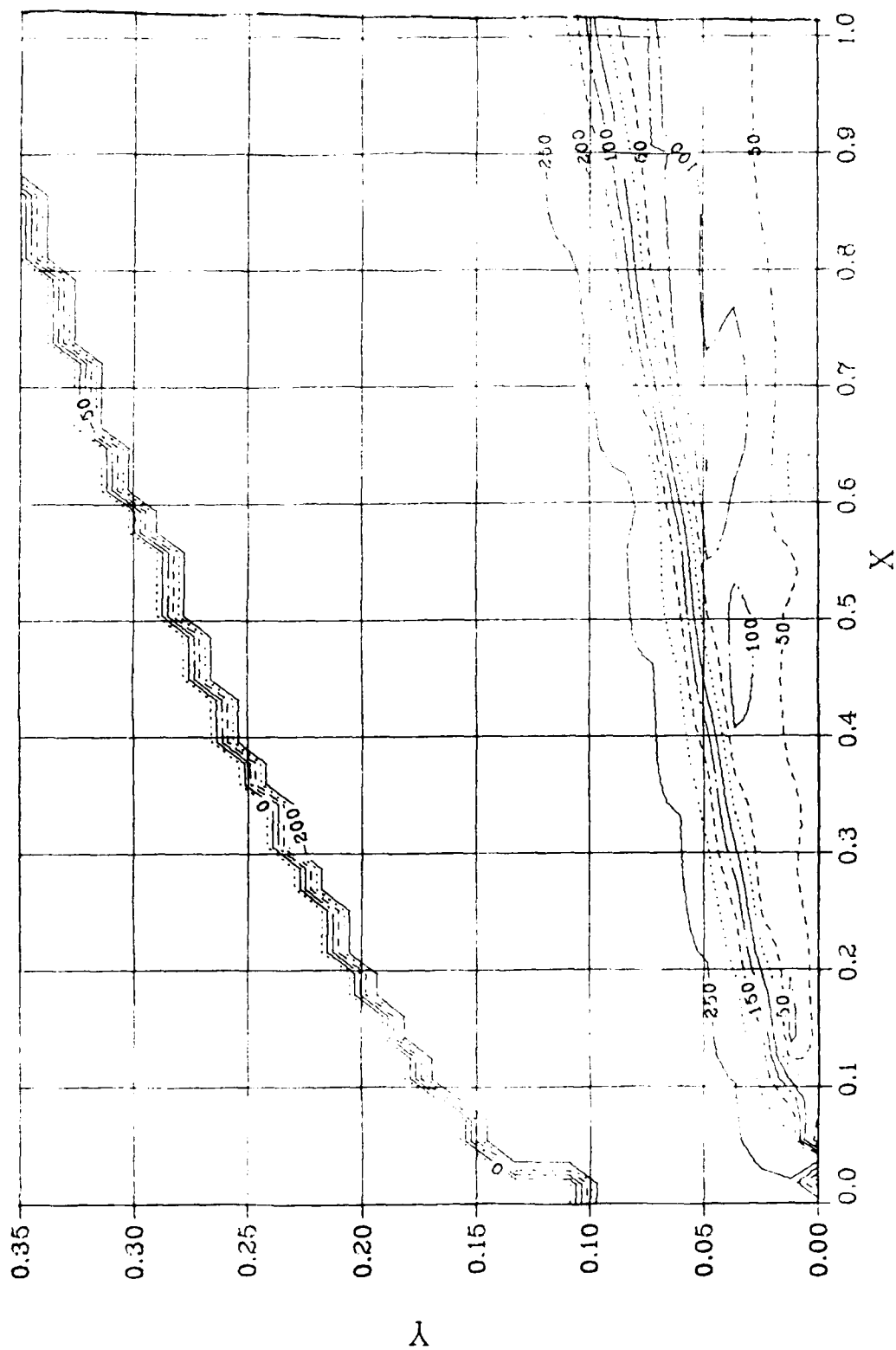


Fig. 19: Nonisothermal Normal Velocity Contours

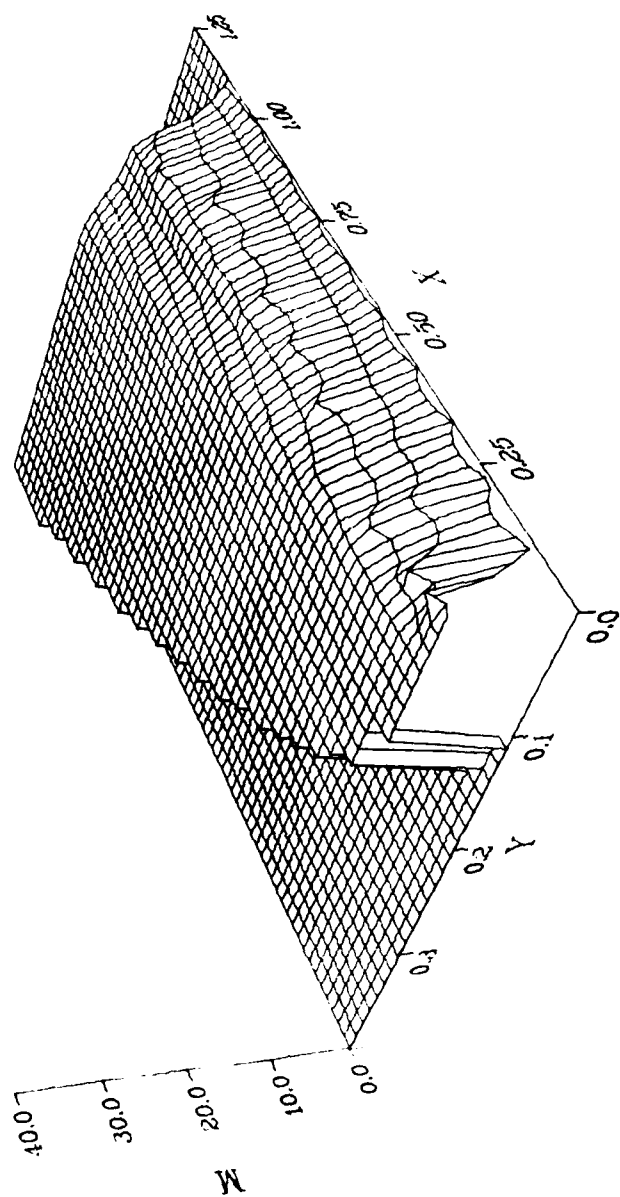


Fig. 20: Nonisothermal Mach Number Surface

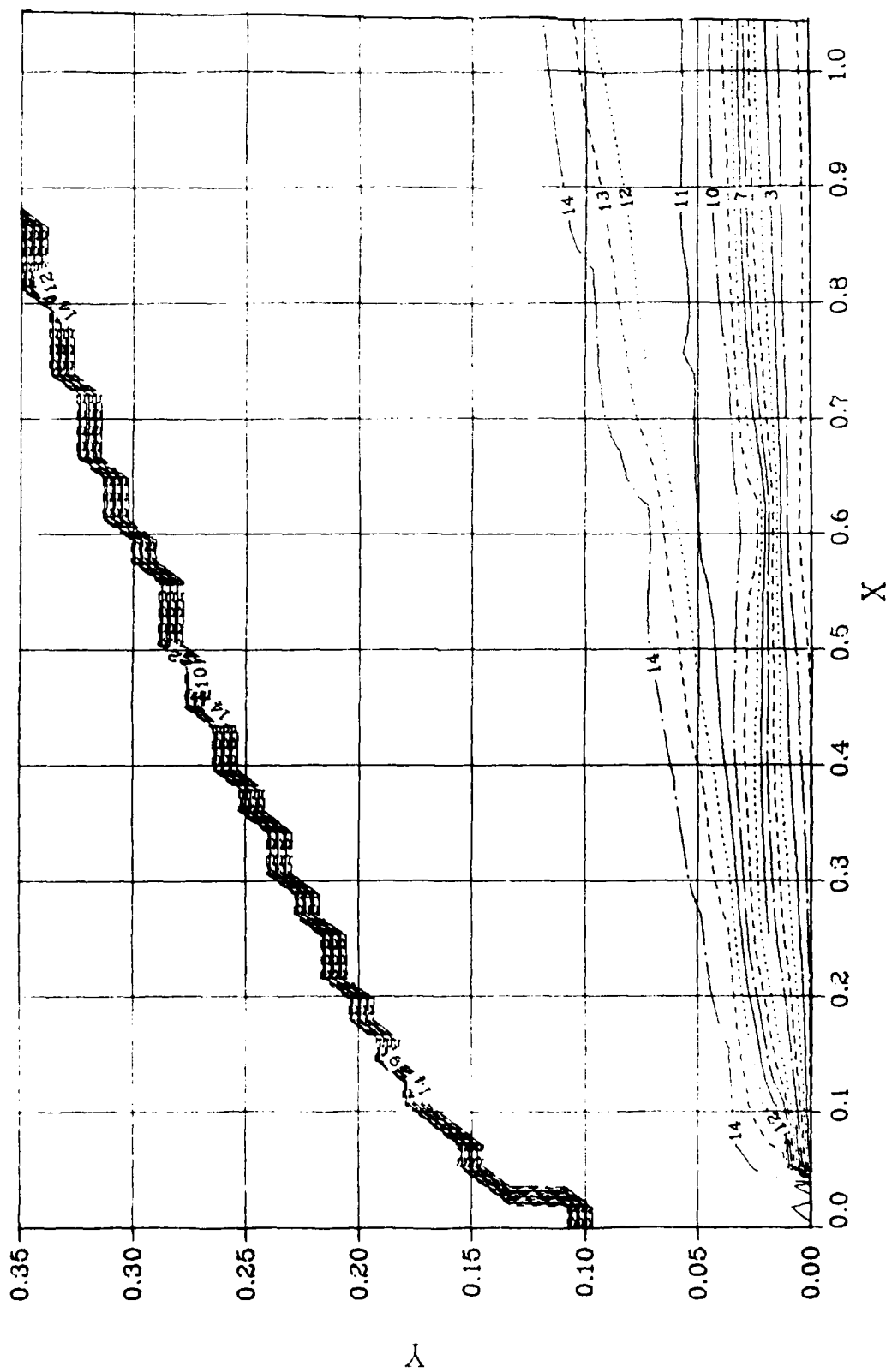


Fig. 21: Nonisothermal Mach Number Contours

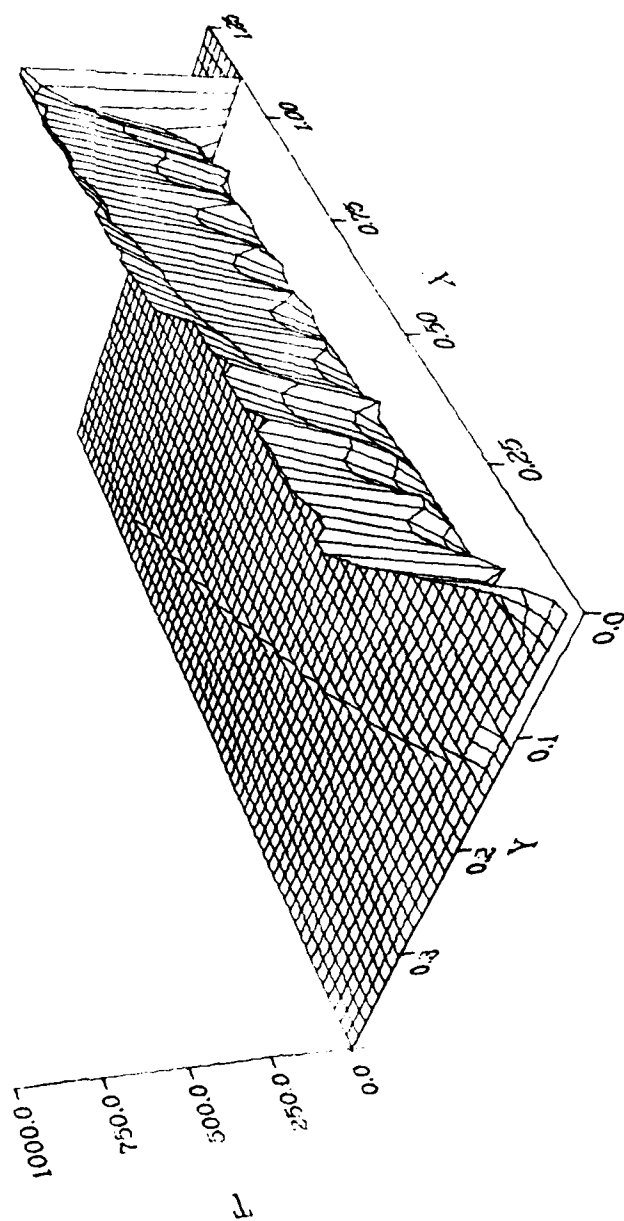


Fig. 22: Nonisothermal Temperature Surface

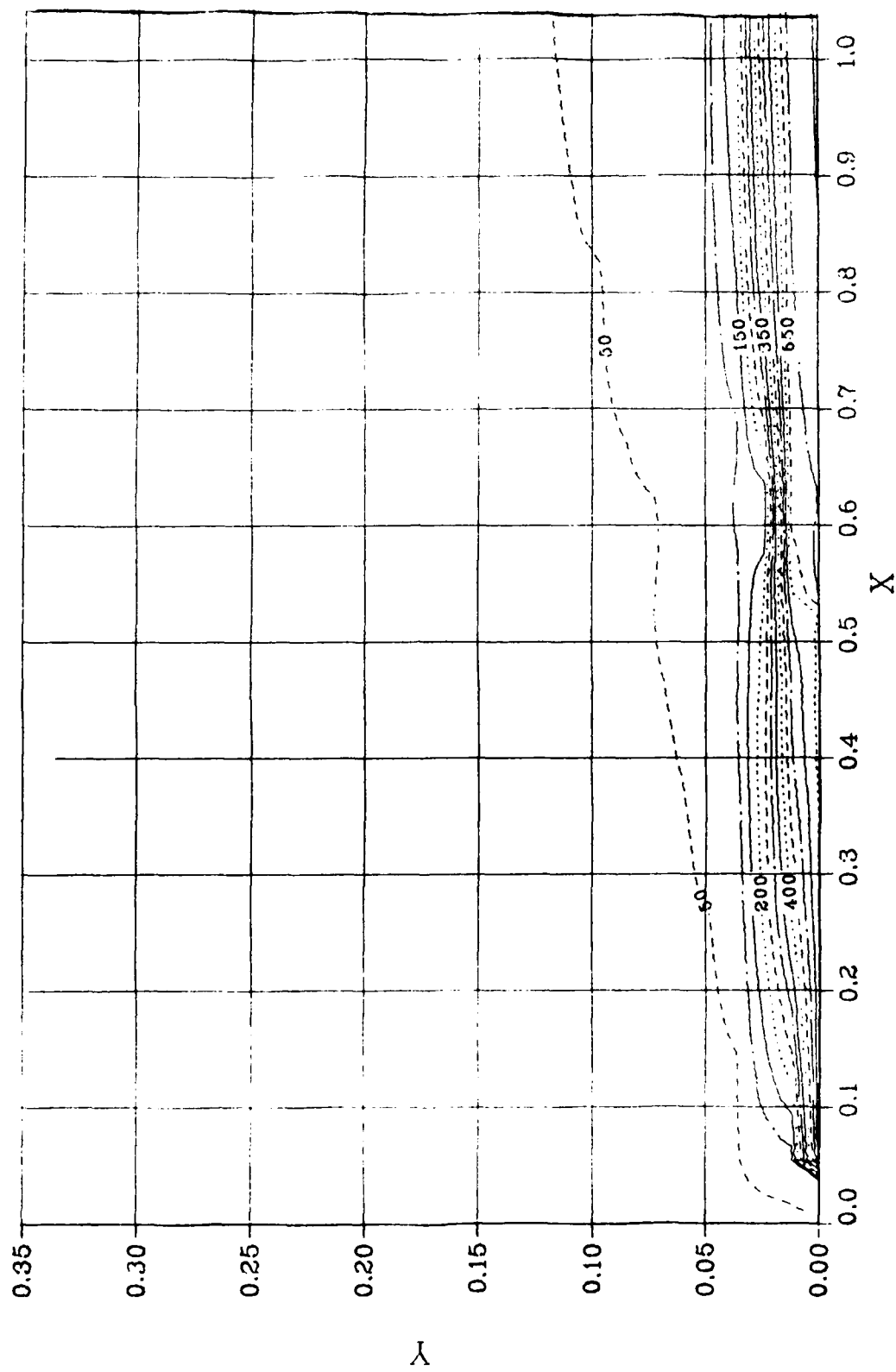


Fig. 23: Nonisothermal Temperature Contours



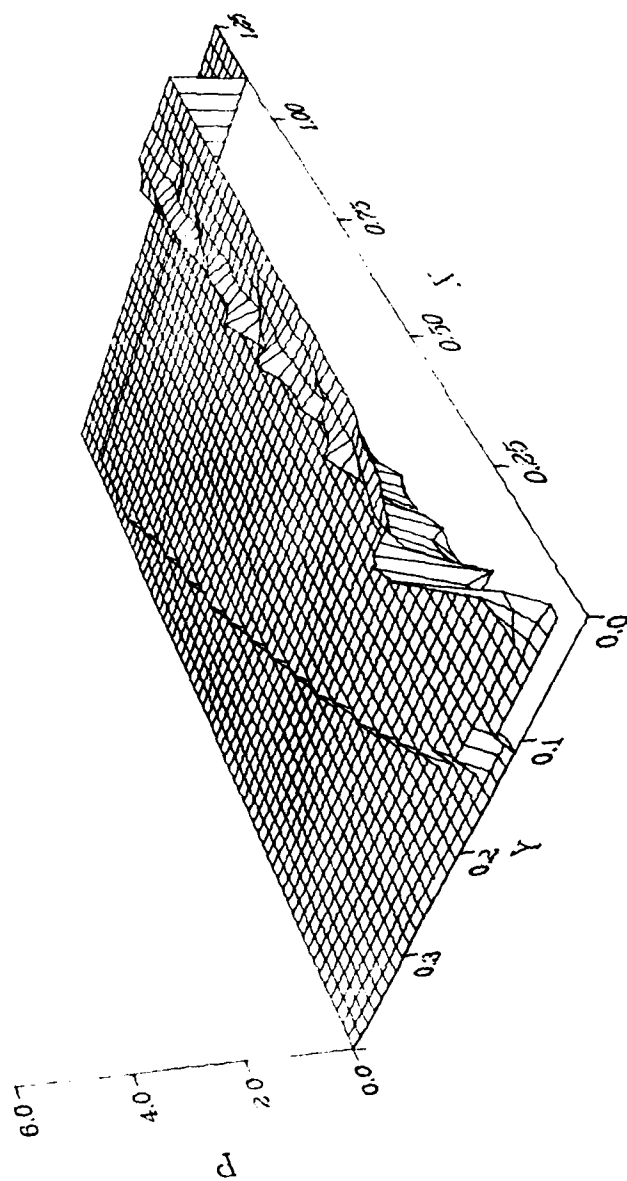


Fig. 24: Nonisothermal Pressure Surface

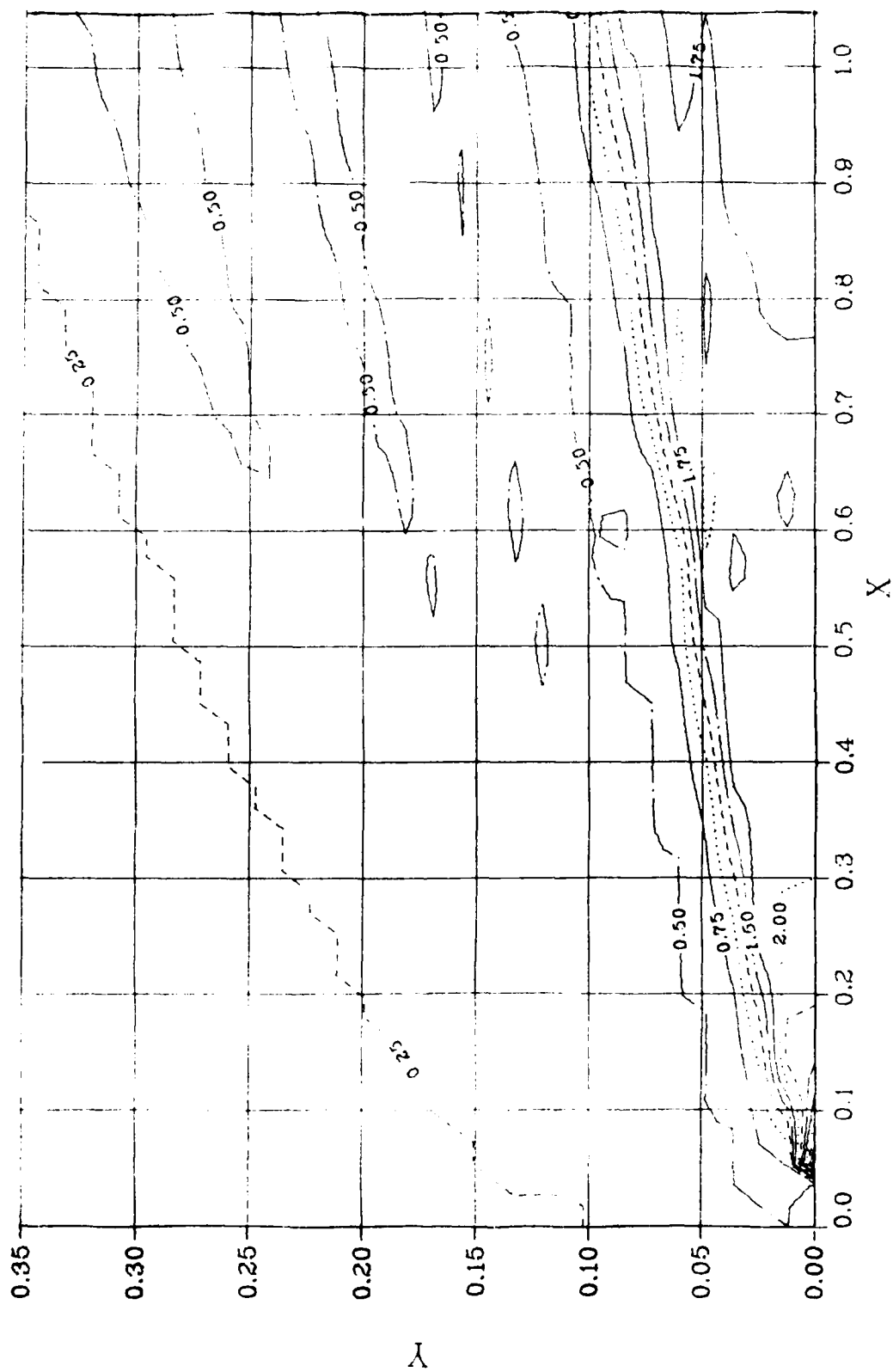


Fig. 25: Nonisothermal Pressure Contours

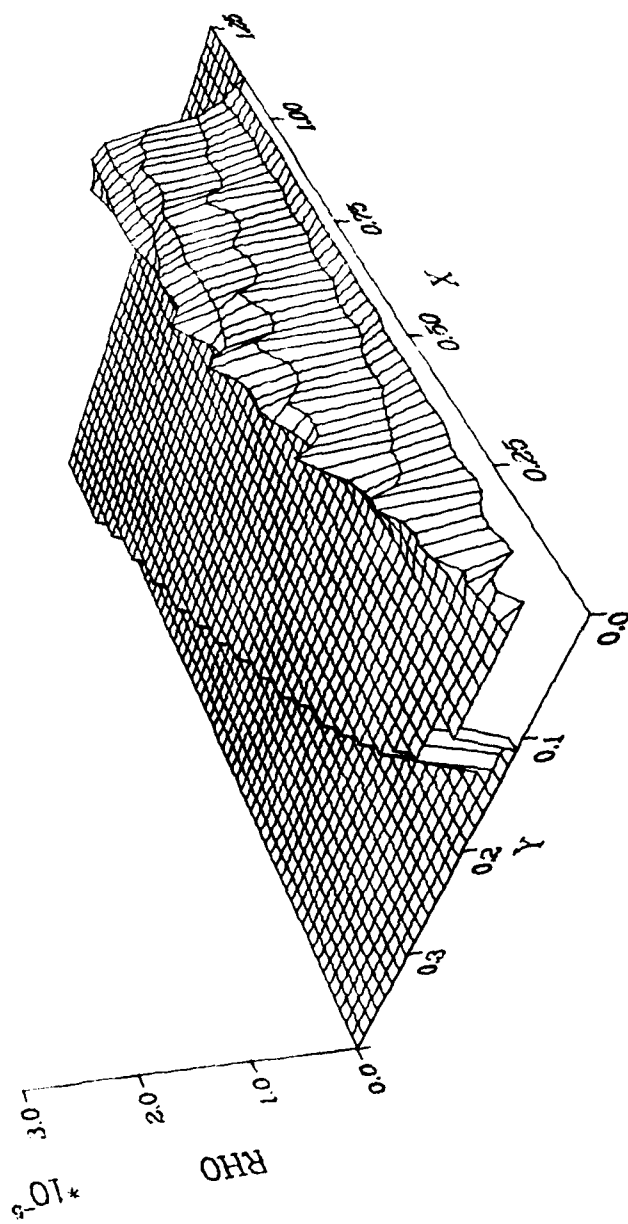


Fig. 26: Nonisothermal Density Surface

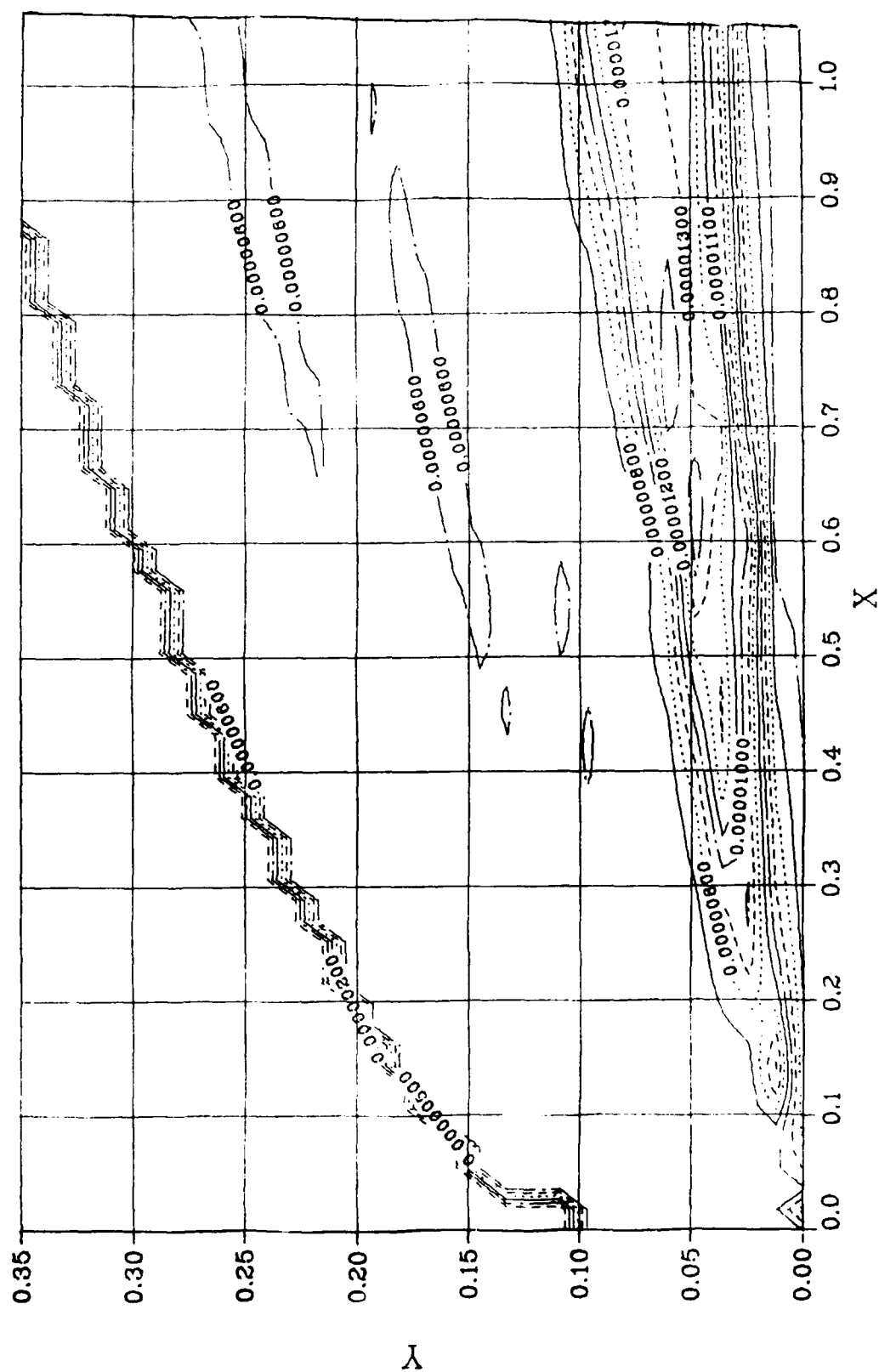


Fig. 27: Nonisothermal Density Contours

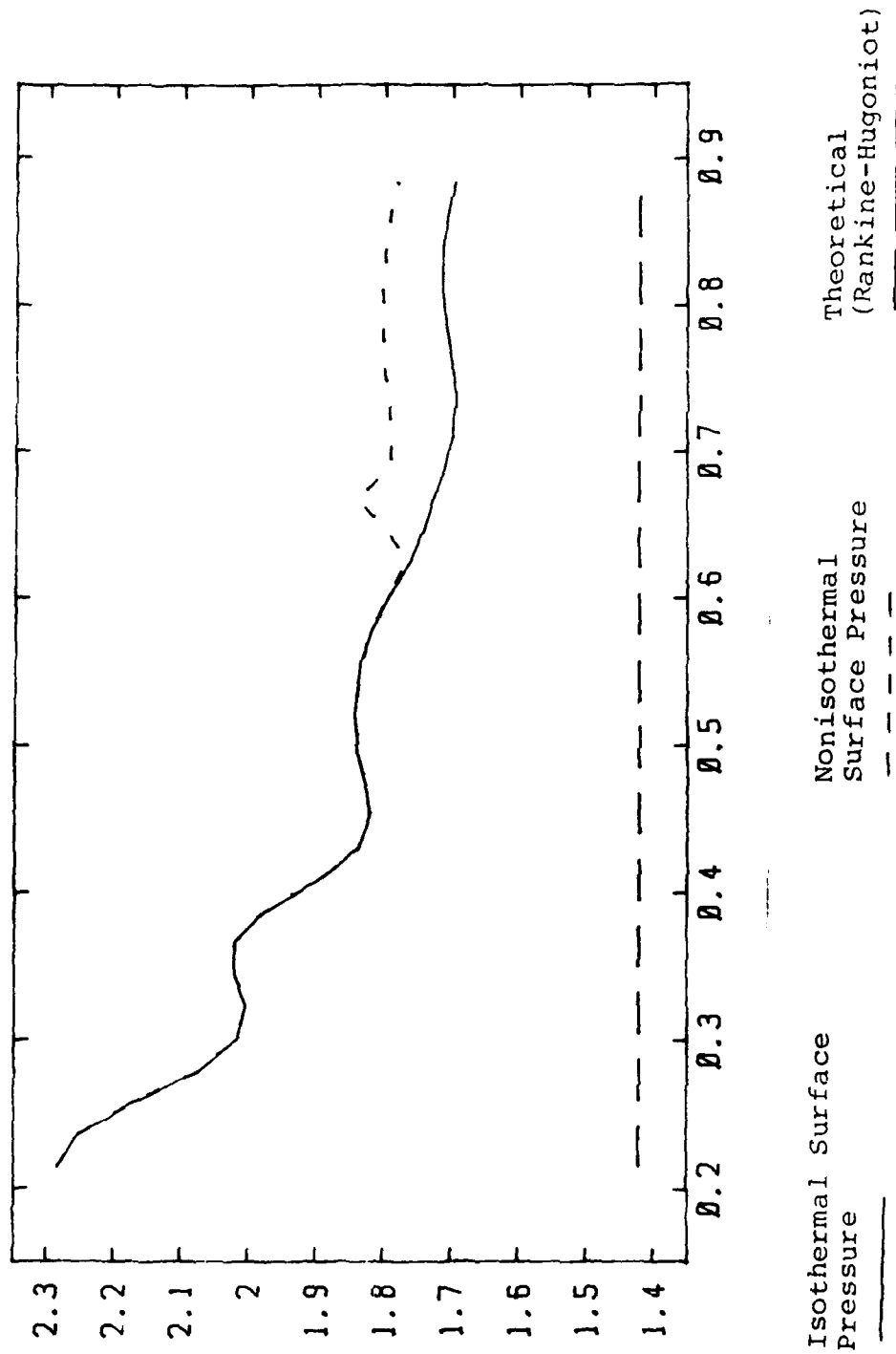


Fig. 28: Surface Pressure

## BIBLIOGRAPHY

1. Cappelano, Lt. Peter S. Heat Transfer/Boundary Layer Investigation of Heating Discrepancies in Wind Tunnel Testing of Orbiter Insulating Articles, MS Thesis, AFIT/GA/AA/82D-3, School of Engineering, Air Force Institute of Technology (AU), Wright-Patterson AFB, OH; December 1982
2. Hodge, Capt James K., Woo, Lt Y. K., and Cappelano, Lt Peter S., "Parameter Estimation for Imbedded Thermocouples in Space Shuttle Wind Tunnel Test Articles With a Nonisothermal Wall," AIAA Paper No. AIAA-83-1533, AIAA 18th Thermophysics Conference, Montreal, Canada; June 1983
3. Woo, Lt Y. K., Transient Heat Transfer Measurement Technique in Wind Tunnel and Data Analysis Technique using System Identification Theory, MS Thesis, School of Engineering, Air Force Institute of Technology (AU), Wright-Patterson AFB, OH; December 1982
4. Schlichting, Dr Hermann, Boundary Layer Theory, 7th Ed., New York, NY, McGraw-Hill Book Co., 1979
5. Nagamatsu, H. T., and Sheer, R. E. Jr., "Hypersonic Shock Wave-Boundary Layer Interaction and Leading Edge Slip," American Rocket Society Journal, Volume 30 Number 5, pp 454-462 (May 1960)

6. Ames Research Staff, National Advisory Committee for Aeronautics, Report 1135: Equations, Tables, and Charts for Compressible Flow, Washington, D.C., U.S. Government Printing Office; 1953
7. Kays, W. M. and Crawford, M. E., Convective Heat and Mass Transfer, 2nd Ed., New York, NY, McGraw-Hill Book Co., 1980
8. MacCormack, Robert W., "The Effect of Viscosity in Hypervelocity Impact Cratering," AIAA Paper No. AIAA-69-354 (1969)
9. MacCormack, Robert W. and Baldwin, B. S., "A Numerical Method for Solving the Navier-Stokes Equations With Application to Shock-Boundary Layer Interactions," AIAA Paper No. AIAA-75-1, AIAA 13th Aerospace Sciences Meeting, Pasadena, CA, January 1975
10. MacCormack, Robert W., "Numerical Solution of the Interaction of a Shock Wave With a Laminar Boundary Layer," Proceedings of the 2nd International Conference on Numerical Methods in Fluid Dynamics; Lecture Notes in Physics, Volume 8, New York, NY, Springer-Verlag; 1970
11. Dorrance, William H., Viscous Hypersonic Flow, New York, NY, McGraw-Hill Book Co.; 1962

## APPENDIX A: PROGRAM LISTINGS FOR NONISOCODE AND STEADY

### OVERVIEW

This Appendix will present the detailed listings for NONISOCODE and STEADY. The programs themselves are explained in detail in Chapter IV.





```

1  *,E15.7/)
525 FORMAT(IX,*SURFACE PARAMETERS:*)
530 FORMAT(IX,* LEADING TEMPERATURE (DEG R) *,F10.4,4X,*REF LENGTH (F
1 T) *,F10.4)
535 FORMAT(IX,* TRAILING TEMPERATURE (DEG R) *,F10.4,3X,*WEDGE ANGLE
1 (DEG) *,F10.4/)
541 FORMAT(IX,*COMPUTATIONAL PARAMETERS:*)
545 FORMAT(IX,* PRESSURE DAMPING: X-DIR *,F10.4,2X,*Y-DIR *,F10.4)
550 FORMAT(IX,* GRID POINTS: X-DIR *,I5,2X,*Y-DIR *,I5)
555 FORMAT(IX,* BETA *,F10.4,2X,*CFL FACTOR *,F10.4)
560 FORMAT(IX,* DETA *,F10.4,2X,*DZETA *,F10.4)
565 FORMAT(IX,*THIS RUN THROUGH ITERATION *,I5/)
540 FORMAT(* X X/RL P/PINF CF*/)
580 FORMAT(* N=*,I5,*DTCFL=*,E15.7,*TMS2=*,E15.7,*TMS1=*,E15.7,
1 *TMS2/TCH=*,E15.7,*DTMAX=*,E15.7)
590 FORMAT(* I J K X Y P RHO EP*/)
1 V W T P
600 FORMAT(IX,3I3,11E11.4)
610 FORMAT(8E15.7)
*****
C READ IN THE INPUT DATA
*****
READ(5,100) XM,REY,TINF,TW1,TW2,RL
READ(5,100) CX,CY,CFL,BETA,DELTAD
READ(5,110) ISTART,ILE,KG
READ(5,110) NEND,JL,KL,ISMTHX,ISMTHY
C
C CONVERT THE WEDGE ANGLE FROM DEGREES TO RADIANS
C
DELTA=(DELTAD*ACOS(-1.))/180.
C
C GENERATING THE FREESTREAM INFORMATION
C
CINF=SQRT(GAMMA*RC*TINF)
UINF=CINF*XM

```

AD-A154 467

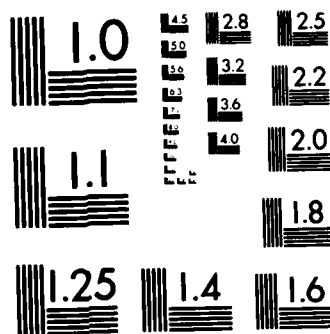
A NUMERICAL SOLUTION OF A NONISOTHERMAL WALL USING THE  
TWO-DIMENSIONAL NA. (U) AIR FORCE INST OF TECH  
WRIGHT-PATTERSON AFB OH SCHOOL OF ENGI. T K ROBERTS  
MAR 85 AFIT/GAE/AA/85M-5 F/G 20/13

2/2

UNCLASSIFIED

NL

										END			
										FINED			
										END			



MICROCOPY RESOLUTION TEST CHART  
NATIONAL BUREAU OF STANDARDS-1963-A

```

RMUINF=2.27E-08*SQRT(TINF**3)/(TINF+198.6)
RHOINF=REY*RMUINF/(UINF*RL)
PINF=RHOINF*RC*TINF
RMUW=2.27E-08*SQRT(TW1**3)/(TW1+198.6)
RU2=RHOINF*UINF**2
TCH=RL/UINF

C
JLM=JL-1
KLM=KL-1
DETA=1.0/JLM
DZETA=1.0/KLM

C
WRITE OUT THE INPUT AND FLOW FIELD INFORMATION

C
IF(BETA.NE.0.0) WRITE(6,200)
WRITE(6,500)
WRITE(6,505) XM,REY
WRITE(6,510) RHOINF,UINF
WRITE(6,515) CINF,TINF
WRITE(6,520) PINF,RMUINF
WRITE(6,525)
WRITE(6,530) TW1,RL
WRITE(6,535) TW2,DELTAD
WRITE(6,541)
WRITE(6,545) CX,CY
WRITE(6,550) KL,JL
WRITE(6,555) BETA,CFL
WRITE(6,560) DETA,DZETA
WRITE(6,565) NEND

C
NI=1
C
TMS1=0.0
TMS2=0.0
C

```



```

C *****
5 CALL PAGE
C *****
1 CONTINUE
C *****
C WRITE THE RESTART DATA INTO RESTART TAPE
C *****
C NEND=NEND+1
C WRITE(2) NEND,TMS1,TMS2,RHO,RHOU,RHOV,RHOW,RHOE,X,Y,EP
C *****
C *****
C WRITE OUT THE COMPUTED FLOW DATA
C *****
C GENERATING THE GRAPHICAL DATA FILE ON TAPE4
C *****
C I=1
C DO 10 K=1,KL
C WRITE(6,590)
C DO 10 J=1,JL
C *****
C RH=1.0/RHO(K,J,1)
C U=RHOU(K,J,1)*RH
C V=RHOV(K,J,1)*RH
C W=U/UIINF
C T=(RHOE(K,J,1)*RH-0.5*(U**2+V**2))*RCV
C P=RHO(K,J,1)*RC*T
C XB=X(K,J,1)/RL
C YB=Y(K,J,1)/RL
C XM=SQRT((U**2+V**2)/(GAMMA*RC*T))
C *****
C WRITE(6,600) I,J,K,X(K,J,1),Y(K,J,1),RHO(K,J,1),
1 U,V,W,T,P,EP(K,J,1)
C WRITE(4,610) XB,YB,U,V,XM,T,P,RHO(K,J,1)
C *****

```

```

10      CONTINUE
C
      WRITE(6,540)
C
      DO 20 K=2,KL
      U=RHO(K,2,1)/RHO(K,2,1)
      IF (K.LE.KG) TW=TW1
      IF (K.GT.KG) TW=TW2
      PDP=RHO(K,1,1)*RC*TW/PINF
      RMUW=2.27E-08*SQR(TW**3)/(TW+198.6)
      CF=2.0*RMUW*ETY(K,1,1)*U/(RU2*DETA)
      XB=X(K,1,1)/RL
      REX=XB*REY
      WRITE(6,610) X(K,1,1),XB,PDP,CF
      WRITE(4,610) REX,CF
C
20      CONTINUE
C
      STOP
      END
      SUBROUTINE PREAMB
      COMMON / / DETA,DZETA,CV,RC,PR,PRT,GAMMA,EP(62,30,1),DTL(30),
1 GAMM1,CFL,BETA,UINF,RHOINF,CINF,TINF,DT,CX,CY,L,DTC(62),KG,
2 IL,JL,KL,ILM,JLM,KLM,ILE,LS,ISMTHX,ISMTHY,DELTA,DELTAD,TW1,TW2
      COMMON /FLUET/ F21(62,2),F22(62,2),F23(62,2),F25(62,2),
1 G21(62,2),G22(62,2),G23(62,2),G25(62,2)
      COMMON /FLUZZ/ F31(62),F32(62),F33(62),F35(62),
1 G31(62),G32(62),G33(62),G35(62)
      COMMON /TV/ ETX(62,30,1),ETY(62,30,1),ZTX(62,30,1),ZTY(62,30,1)
      COMMON /DEP/ RHO(62,30,1),RHOV(62,30,1),RHOV(62,30,1),
1 RHOV(1,1,1),RHOE(62,30,1)
C
      SPECIFY INITIAL CONDITIONS FOR THE FLOW FIELD
C
      RUINF=RHOINF*UINF

```



```

REINF=RHOINF*(CV*TINF+0.5*UINF**2)
RHOW(1,1,1)=0.0

```

C

```

DO 1 J=1,JL
DO 1 K=1,KL
RHO (K,J,1)=RHOINF
RHOV(K,J,1)=RHOINF*COS(DELTA)
RHOV(K,J,1)=-RHOINF*SIN(DELTA)
RHOE(K,J,1)=REINF
EP(K,J,1)=0.0
CONTINUE

```

1

```

SPECIFY THE NOSLIP BOUNDARY CONDITION AND SURFACE TEMPERATURE

```

C  
C  
C

```

RHOWL1=RHOINF*(TINF/TW1)
RHOWL2=RHOINF*(TINF/TW2)
RHOEW=RHOINF*TINF*CV

```

C

```

DO 2 K=1,LE,KL
IF (K.LE.KG) RHOWL=RHOWL1
IF (K.GT.KG) RHOWL=RHOWL2
RHO(K,1,1)=RHOWL
RHOV(K,1,1)=0.0
RHOV(K,1,1)=0.0
RHOE(K,1,1)=RHOEW
CONTINUE

```

2

```

INITIALIZE THE FLUX COMPONENTS

```

C  
C  
C  
C

```

DO 3 J=1,2
DO 3 K=1,KL

```

```

F21(K,J)=0.0
F22(K,J)=0.0

```

C

```

C
F23(K,J)=0.0
F25(K,J)=0.0

G21(K,J)=0.0
G22(K,J)=0.0
G23(K,J)=0.0
G25(K,J)=0.0

C
CONTINUE
C
DO 4 K=1,KL
F31(K)=0.0
F32(K)=0.0
F33(K)=0.0
F35(K)=0.0

G31(K)=0.0
G32(K)=0.0
G33(K)=0.0
G35(K)=0.0

C
CONTINUE
C
RETURN
END
SUBROUTINE TMSTEP
COMMON / / DETA,DZETA,CV,RC,PR,PRT,GAMMA,EP(62,30,1),DTL(30),
1 GAMM1,CFL,BETA,UINF,RHOINF,CINF,TINF,DT,CX,CY,L,DTC(62),KG,
2 IL,JL,KL,ILM,JLM,KLM,ILE,LS,ISMTHX,ISMTHY,DELTA,DELTAD,TW1,TW2
COMMON /TV/ ETX(62,30,1),ETY(62,30,1),ZTX(62,30,1),ZTY(62,30,1)
COMMON /DEP/ RHO(62,30,1),RHOV(62,30,1),RHOV(62,30,1),
1 RHOV(1,1,1),RHOE(62,30,1)
DIMENSION UET(62),UZT(62),U(62),V(62),C(62)
C
SET UP INITIAL CFL TIME STEP VALUE
C

```

```

C      DTC(1)=1.0
      GAMM2=GAMMA*GAMM1
      DTCFL=1.0
      RDET=1.0/DETA
      RDZT=1.0/DZETA

C      DO 1 J=2,JLM
      DO 2 K=2,KLM

C      RH=1.0/RHO(K,J,1)
      U(K)=RHOU(K,J,1)*RH
      V(K)=RHOV(K,J,1)*RH
      C(K)=SQRT(GAMM2*(RHOE(K,J,1)*RH-0.5*(U(K)**2+V(K)**2)))

C      UET(K)=ETX(K,J,1)*U(K)+ETY(K,J,1)*V(K)
      UZT(K)=ZTX(K,J,1)*U(K)+ZTY(K,J,1)*V(K)

C      DTC(K)=1.0/(ABS(UET(K))*RDET+ABS(UZT(K))*RDZT+
1 C(K)*SQRT((ETX(K,J,1)*RDET+ZTX(K,J,1)*RDZT)**2+
2 (ETY(K,J,1)*RDET+ZTY(K,J,1)*RDZT)**2))

C      CONTINUE
2
C      PERFORM THE COMPARISON AND MODIFY THE CFL TIME STEP

C      DTMIN=DTC(1)
      DO 3 K=2,KLM
      DTMIN=AMIN1(DTC(K),DTMIN)
      CONTINUE
3
C      DTL(J)=DTMIN*CFL

C      COMPARING DTMIN BETWEEN ADJACENT PLANES
      DTCFL=AMIN1(DTCFL,DTMIN)

```

```

C 1
C
C  ADJUST DTCFL FOR VISCOUS EFFECT (TRIAL AND ERROR)
C  DT=CFL*DTCFL
C
C  RETURN
C  END
C  SUBROUTINE BC
C  COMMON / / DETA,DZETA,CV,RC,PR,PRT,GAMMA,EP(62,30,1),DTL(30),
1 GAMM1,CFL,BETA,UINF,RHOINF,CINF,TINF,DT,CX,CY,L,DTC(62),KG,
2 IL,JL,KL,ILM,JLM,KLM,ILE,LS,ISMTHX,ISMTHY,DELTA,DELTAD,TW1,TW2
C  COMMON /TV/ ETX(62,30,1),ETY(62,30,1),ZTX(62,30,1),ZTY(62,30,1)
C  COMMON /DEP/ RHO(62,30,1),RHOU(62,30,1),RHOV(62,30,1),
1 RHOH(1,1,1),RHOE(62,30,1)
C  COMMON /DEPP/ RHOP(62,30,1),RHOUP(62,30,1),RHOVP(62,30,1),
1 RHOWP(1,1,1),RHOEP(62,30,1)
C
C  RUINF=RHOINF*UINF
C  REINF=RHOINF*(CV*TINF+0.5*UINF**2)
C
C  IF(L.EQ.2) GO TO 10
C
C  *****
C  PREDICTOR SWEEP
C  *****
C
C  ON THE SOLID CONTOUR, NO-SLIP FOR U,V,W,CONSTANT SURFACE TEMP.
C  AND DP/DN=0. APPROXIMATION
C
C  DO 1 K=2,KLM
C  IF (K.LE.KG) TW=TW1
C  IF (K.GT.KG) TW=TW2
C  RH=1.0/RHOP(K,2,1)
C  RHOU(K,1,1)=0.0

```

```

RHOVP(K,1,1)=0.0
RHOP(K,1,1)=RHOP(K,2,1)*(RHOEP(K,2,1)*RH-0.5*
1 ((RHOUP(K,2,1)*RH)**2+(RHOVP(K,2,1)*RH)**2))/(CV*TW)
RHOEP(K,1,1)=RHOP(K,1,1)*CV*TW
1 CONTINUE

```

1

C

C

C

C FOR ZERO STREAMLINE PRECEDING THE LEADING EDGE  
KF=ILE-1

```

DO 4 K=2,KF
RHOP(K,1,1)=RHOINF
RHOUP(K,1,1)=RHOINF*COS(DELTA)
RHOVP(K,1,1)=-RHOINF*SIN(DELTA)
RHOEP(K,1,1)=REINF
4 CONTINUE

```

4

C

C

C

C

FAR FIELD BOUNDARY CONDITIONS

```

DO 2 K=1,KL
RHOP (K,JL,1)=RHOINF
RHOUP(K,JL,1)=RHOINF*COS(DELTA)
RHOVP(K,JL,1)=-RHOINF*SIN(DELTA)
RHOEP(K,JL,1)=REINF
CONTINUE

```

2

C

C

C

C

THE UPSTREAM AND DOWNSTREAM BOUNDARY CONDITIONS

```

DO 3 J=1,JL
RHOP (1,J,1)=RHOINF
RHOUP(1,J,1)=RHOINF*COS(DELTA)
RHOVP(1,J,1)=-RHOINF*SIN(DELTA)
RHOEP(1,J,1)=REINF

```

C

```

3      RHO (KL,J,1)=RHOP (KLM,J,1)
C      RHOUP(KL,J,1)=RHOUP(KLM,J,1)
C      RHOVP(KL,J,1)=RHOVP(KLM,J,1)
C      RHOEP(KL,J,1)=RHOEP(KLM,J,1)
C      CONTINUE
C
C      GO TO 100
C
C      *****
C      CORRECTOR SWEEP
C      *****
C
C      ON THE SOLID CONTOUR, NO-SLIP FOR U,V,W, CONSTANT SURFACE TEMP.
C      AND DP/DN=0. APPROXIMATION
C
10     DO 11 K=2,KLM
C      IF (K.LE.KG) TW=TW1
C      IF (K.GT.KG) TW=TW2
C      RH=1.0/RHO(K,2,1)
C      RHO(K,1,1)=0.0
C      RHOV(K,1,1)=0.0
C      RHO (K,1,1)=RHO (K,2,1)*(RHOE(K,2,1)*RH-0.5*
1      ((RHOUP(K,2,1)*RH)**2+(RHOV(K,2,1)*RH)**2))/(CV*TW)
C      RHOE(K,1,1)=RHO(K,1,1)*CV*TW
11     CONTINUE
C
C      FOR ZERO STREAMLINE PRECEDING THE LEADING EDGE
C      KF=ILE-1
C      DO 14 K=2,KF
C      RHO(K,1,1)=RHOINF
C      RHOUP(K,1,1)=RUINF*COS(DELTA)
C      RHOV(K,1,1)=-RUINF*SIN(DELTA)
C      RHOE(K,1,1)=REINF

```

```

14 CONTINUE
C
C FAR FIELD BOUNDARY CONDITIONS
C
C
DO 12 K=1,KL
RHO (K,JL,1)=RHOINF
RHOE(K,JL,1)=REINF
RHOE(K,JL,1)=REINF
12 CONTINUE
C
C THE UPSTREAM AND DOWNSTREAM BOUNDARY CONDITIONS
C
C
DO 13 J=1,JL
RHO (1,J,1)=RHOINF
RHO(1,J,1)=RHOINF*COS(DELTA)
RHOV(1,J,1)=-RHOINF*SIN(DELTA)
RHOE(1,J,1)=REINF
C
RHO (KL,J,1)=RHO (KLM,J,1)
RHO(1,J,1)=RHO(KLM,J,1)
RHOV(KL,J,1)=RHOV(KLM,J,1)
RHOE(KL,J,1)=RHOE(KLM,J,1)
13 CONTINUE
C
C
100 RETURN
END
SUBROUTINE TRANS
COMMON / DETA,DZETA,CV,RC,PR,PRT,GAMMA,EP(62,30,1),DTL(30),
1 GAMM1,CFL,BETA,UINF,RHOINF,CINF,TINF,DT,CX,CY,L,DTC(62),KG,
2 IL,JL,KL,ILM,JLM,KLM,ILE,LS,ISMTHX,ISMTHY,DELTA,DELTAD,TW1,TW2
COMMON /TV/ ETX(62,30,1),ETY(62,30,1),ZTX(62,30,1),ZTY(62,30,1)
COMMON /DOF/ X(62,30,1),Y(62,30,1)
DIMENSION XET(62,30),YET(62,30),DJ(62,30),

```

```

C      2 XZT(62,30),YZT(62,30),RDJ(62,30)

      RDET=1.0/(2.0*DETA)
      RDZT=1.0/(2.0*DZETA)
      JLM2=JLM-1
      KLM2=KLM-1

C      SET THE DUMMY THREE DIMENSIONAL METRICS

C      GENERATING DX/DETA AND DY/DETA

C      ONE-SIDE DIFFERENCING FOR J=1
101    DO 101 KV=1,KL
        XET(KV,1)=(4.0*X(KV,2,1)-X(KV,3,1)-3.0*X(KV,1,1))*RDET
        YET(KV,1)=(4.0*Y(KV,2,1)-Y(KV,3,1)-3.0*Y(KV,1,1))*RDET
        CONTINUE
C
C      ONE-SIDE DIFFERENCING FOR J=JL
102    DO 102 KV=1,KL
        XET(KV,JL)=- (4.0*X(KV,JLM,1)-X(KV,JLM2,1)-3.0*X(KV,JL,1))*RDET
        YET(KV,JL)=- (4.0*Y(KV,JLM,1)-Y(KV,JLM2,1)-3.0*Y(KV,JL,1))*RDET
        CONTINUE
C
C      CENTRAL DIFFERENCING FOR FIELD POINTS
      DO 103 JV=2,JLM
        JP=JV+1
        JM=JV-1
        DO 104 KV=1,KL
          XET(KV,JV)=(X(KV,JP,1)-X(KV,JM,1))*RDET

```



```

104 YET(KV,JV)=(Y(KV,JP,1)-Y(KV,JM,1))*RDET
103 CONTINUE
C
C GENERATING DX/DZETA AND DY/DZETA
C
C ONE-SIDE DIFFERENCING FOR K=1
C
DO 201 JV=1,JL
XZT(1,JV)=(4.0*X(2,JV,1)-X(3,JV,1)-3.0*X(1,JV,1))*RDZT
YZT(1,JV)=(4.0*Y(2,JV,1)-Y(3,JV,1)-3.0*Y(1,JV,1))*RDZT
201 CONTINUE
C
C ONE-SIDE DIFFERENCING FOR K=KL
C
DO 202 JV=1,JL
XZT(KL,JV)=- (4.0*X(KLM,JV,1)-X(KLM2,JV,1)-3.0*X(KL,JV,1))*RDZT
YZT(KL,JV)=- (4.0*Y(KLM,JV,1)-Y(KLM2,JV,1)-3.0*Y(KL,JV,1))*RDZT
202 CONTINUE
C
C CENTRAL DIFFERENCING FOR FIELD POINTS
C
DO 203 JV=1,JL
DO 204 KV=2,KLM
KP=KV+1
KM=KV-1
XZT(KV,JV)=(X(KP,JV,1)-X(KM,JV,1))*RDZT
YZT(KV,JV)=(Y(KP,JV,1)-Y(KM,JV,1))*RDZT
204 CONTINUE
203 CONTINUE
C
C GENERATING THE INVERSE JACOBIAN OF TRANSFORMATION
C
DO 300 JV=1,JL

```

```

DO 301 KV=1,KL
DJ(KV,JV)=XET(KV,JV)*YZT(KV,JV)-XZT(KV,JV)*YET(KV,JV)
CONTINUE
301 CONTINUE
300 CONTINUE
C
C
DO 303 JV=1,JL
DO 304 KV=1,KL
RDJ(KV,JV)=1.0/DJ(KV,JV)
CONTINUE
304 CONTINUE
303 CONTINUE
C
C
GENERATING THE METRICS OF COORDINATES TRANSFORMATION
C
DO 305 JV=1,JL
DO 306 KV=1,KL
ETX(KV,JV,1)= YZT(KV,JV)*RDJ(KV,JV)
ZTX(KV,JV,1)=-YET(KV,JV)*RDJ(KV,JV)
ETY(KV,JV,1)=-XZT(KV,JV)*RDJ(KV,JV)
ZTY(KV,JV,1)= XET(KV,JV)*RDJ(KV,JV)
CONTINUE
306 CONTINUE
305 CONTINUE
C
RETURN
END
SUBROUTINE PAGE
COMMON / / DETA,DZETA,CV,RC,PR,PRT,GAMMA,EP(62,30,1),DTL(30),
1 GAMM1,CFL,BETA,UINF,RHOINF,CINF,TINF,DT,CX,CY,L,DTC(62),KG,
2 IL,JL,KL,ILM,JLM,KLM,ILE,LS,ISMTHX,ISMTHY,DELTA,DELTAD,TW1,TW2
COMMON /DV/ R(62,30,1),U(62,30,1),V(62,30,1),W(1,1,1),
1 P(62,30,1),T(62,30,1)
COMMON /TV/ ETX(62,30,1),ETY(62,30,1),ZTX(62,30,1),ZTY(62,30,1)
COMMON /DEP/ RHO(62,30,1),RHOV(62,30,1),

```

```

1 RHOV(1,1,1),RHOE(62,30,1)
COMMON /DEPP/ RHOV(62,30,1),RHOUP(62,30,1),RHOVP(62,30,1),
1 RHOVP(1,1,1),RHOEP(62,30,1)

```

```

W(1,1,1)=0.0

```

```

*****
PREDICTOR SWEEP
*****

```

```

L=1

```

```

GENERATING THREE PAGE TEMPORAL VECTOR ARRAYS

```

```

DO 1 JV=1,JL
DO 1 KV=1,KL

```

```

R(KV,JV,1)=RHO (KV,JV,1)
U(KV,JV,1)=RHOV(KV,JV,1)/R(KV,JV,1)
V(KV,JV,1)=RHOV(KV,JV,1)/R(KV,JV,1)
T(KV,JV,1)=(RHOE(KV,JV,1)/R(KV,JV,1)-0.5*(U(KV,JV,1)**2
1 +V(KV,JV,1)**2))/CV
P(KV,JV,1)=R(KV,JV,1)*RC*T(KV,JV,1)

```

```

CONTINUE

```

```

DO 2 J=2,JLM
CALL LETA(J)
CALL LZETA(J)
CALL SUM(J)
CONTINUE

```

```

CALL BC

```

```
C
C
C *****
C CORRECTOR SWEEPS
C *****
C
C      L=2
C
C GENERATING THREE PAGE TEMPORAL VECTOR ARRAYS
C
C      DO 10 J=1,JL
C      DO 10 KV=1,KL
C
C         R(KV,JV,1)=RHOP (KV,JV,1)
C         U(KV,JV,1)=RHOUP(KV,JV,1)/R(KV,JV,1)
C         V(KV,JV,1)=RHOVP(KV,JV,1)/R(KV,JV,1)
C         T(KV,JV,1)=(RHOEP(KV,JV,1)/R(KV,JV,1)-0.5*(U(KV,JV,1)*2
C
C            1 +V(KV,JV,1)**2))/CV
C         P(KV,JV,1)=R(KV,JV,1)*RC*T(KV,JV,1)
C
C      CONTINUE
C
C      DO 11 J=2,JLM
C      CALL LETA(J)
C      CALL LZETA(J)
C      CALL SUM(J)
C      CONTINUE
C
C      CALL BC
C
C      RETURN
```

```

END
SUBROUTINE LETA(J)
COMMON / / DETA,DZETA,CV,RC,PR,PRT,GAMMA,EP(62,30,1),DTL(30),
1 GAMM1,CFL,BETA,UINF,RHOINF,CINF,TINF,DT,CX,CY,L,DTC(62),KG,
2 IL,JL,KL,ILM,JLM,KLM,ILE,LS,ISMTHX,ISMTHY,DELTA,DELTAD,TW1,TW2
COMMON /FLUET/ F21(62,2),F22(62,2),F23(62,2),F25(62,2),
1 G21(62,2),G22(62,2),G23(62,2),G25(62,2)
COMMON /DV/ R(62,30,1),U(62,30,1),V(62,30,1),W(1,1,1),
1 P(62,30,1),T(62,30,1)
COMMON /TV/ ETX(62,30,1),ETY(62,30,1),ZTX(62,30,1),ZTY(62,30,1)
DIMENSION UET(62),UZT(62),VET(62),VZT(62),RMU(62),
1 RLMBD(62),SMU(62),RK(62),TAUXX(62),TAUXR(62),
2 TAURR(62),TX(62),TY(62),TET(62),Tzt(62),DUDX(62),
3 DVDR(62)

```

C

```

RDET=1.0/DETA
RDZT=1.0/(2.0*DZETA)

```

C

```

DO 1 M=1,2

```

C

C

FORWARD & BACKWARD DIFFERENCING FOR PREDICTOR & CORRECTOR

C

C

```

*****
JV=L+M+J-3
JM=J+M-2
JP=JM+1
*****

```

C

C

C

```

DO 2 KV=2,KLM

```

C

```

KP=KV+1
KM=KV-1

```

```

C
C      GENERATING THE SHEAR STRESS & HEAT FLUX TERMS
      UET(KV)=(U(KV,JP,1)-U(KV,JM,1))*RDET
      VET(KV)=(V(KV,JP,1)-V(KV,JM,1))*RDET
      TET(KV)=(T(KV,JP,1)-T(KV,JM,1))*RDET
C
      UZT(KV)=(U(KP,JV,1)-U(KM,JV,1))*RDZT
      VZT(KV)=(V(KP,JV,1)-V(KM,JV,1))*RDZT
      TZT(KV)=(T(KP,JV,1)-T(KM,JV,1))*RDZT
C
C      GENERATING THE VISCOSITY COEFFS & HEAT CONDUCTIVITY
C
      RMU(KV)=2.27E-08*SQRT(T(KV,JV,1)**3)/(T(KV,JV,1)+198.6)
      RK(KV)=GAMMA*CV*(RMU(KV)/PR+EP(KV,JV,1)/PRT)
      RMU(KV)=RMU(KV)+EP(KV,JV,1)
      RLMBD(KV)=- (2.0/3.0)*RMU(KV)
      SMU(KV)=2.0*RMU(KV)+RLMBD(KV)
C
C      CONTINUE
C
C      DO 3 KV=2,KLM
C
C      DUDX(KV)=ETX(KV,JV,1)*UET(KV)+ZTX(KV,JV,1)*UZT(KV)
C      DVDR(KV)=ETY(KV,JV,1)*VET(KV)+ZTY(KV,JV,1)*VZT(KV)
C
C      TAUX(KV)=SMU(KV)*DUDX(KV)+RLMBD(KV)*DVDR(KV)
C      1 -P(KV,JV,1)
C
C      TAURR(KV)=SMU(KV)*DVDR(KV)+RLMBD(KV)*DUDX(KV)
C      1 -P(KV,JV,1)
C
C      TAUXR(KV)=RMU(KV)*(ETY(KV,JV,1)*UET(KV)+ZTY(KV,JV,1)*
C      1 UZT(KV)+ETX(KV,JV,1)*VET(KV)+ZTX(KV,JV,1)*VZT(KV))
C
C      CONTINUE
C

```

```

C
C      GENERATING THE HEAT FLUX TERMS
C
C      DO 4 KV=2,KLM
C
C      TX(KV)=ETX(KV,JV,1)*TET(KV)+ZTX(KV,JV,1)*TZT(KV)
C      TY(KV)=ETY(KV,JV,1)*TET(KV)+ZTY(KV,JV,1)*TZT(KV)
C
C      CONTINUE
C
C      GENERATING THE FLUX TERMS
C
C      DO 5 KV=2,KLM
C
C      F21(KV,M)=R(KV,JV,1)*U(KV,JV,1)
C      F22(KV,M)=F21(KV,M)*U(KV,JV,1)-TAUXX(KV)
C      F23(KV,M)=F21(KV,M)*V(KV,JV,1)-TAUXR(KV)
C      F25(KV,M)=F21(KV,M)*(CV*T(KV,JV,1)+0.5*(U(KV,JV,1)**2+
C      1 V(KV,JV,1)**2+W(1,1,1)**2))-RK(KV)*TX(KV)
C      2 -(U(KV,JV,1)*TAUXX(KV)+V(KV,JV,1)*TAUXR(KV))
C
C      G21(KV,M)=(R(KV,JV,1)*V(KV,JV,1))
C      G22(KV,M)=G21(KV,M)*U(KV,JV,1)-TAUXR(KV)
C      G23(KV,M)=G21(KV,M)*V(KV,JV,1)-TAURR(KV)
C      G25(KV,M)=G21(KV,M)*(CV*T(KV,JV,1)+0.5*(U(KV,JV,1)**2+
C      1 V(KV,JV,1)**2+W(1,1,1)**2))-RK(KV)*TY(KV)
C      2 -(U(KV,JV,1)*TAUXR(KV)+V(KV,JV,1)*TAURR(KV))
C
C      CONTINUE
C
C      CONTINUE
C      RETURN
C      END
C
C      SUBROUTINE LZETA(J)
C      COMMON / DETA,DZETA,CV,RC,PR,PRT,GAMMA,EP(62,30,1),DTL(30),

```





```

C      V2T(KK)=(V(KP,J,1)-V(KM,J,1))*RDZT
C      TZT(KK)=(T(KP,J,1)-T(KM,J,1))*RDZT
C
C      GENERATING THE VISCOSITY COEFFS & HEAT CONDUCTIVITY
C
C      RMU(KK)=2.27E-08*SQRT(T(KV,J,1)**3)/(T(KV,J,1)+198.6)
C      RK(KK)=GAMMA*CV*(RMU(KK)/PR+EP(KV,J,1)/PRT)
C      RMU(KK)=RMU(KK)+EP(KV,J,1)
C      RLMBD(KK)=-((2.0/3.0)*RMU(KK)
C      SMU(KK)=2.0*RMU(KK)+RLMBD(KK)
C
C      1 CONTINUE
C
C      DO 2 KK=1,KLM
C
C      KV=KK+L-1
C
C      DUDX(KK)=ETX(KV,J,1)*UET(KK)+ZTX(KV,J,1)*UZT(KK)
C      DVDR(KK)=ETY(KV,J,1)*VET(KK)+ZTY(KV,J,1)*VZT(KK)
C
C      TAUXX(KK)=SMU(KK)*DUDX(KK)+RLMBD(KK)*DVDR(KK)
C      1 -P(KV,J,1)
C
C      TAURR(KK)=SMU(KK)*DVDR(KK)+RLMBD(KK)*DUDX(KK)
C      1 -P(KV,J,1)
C
C      TAUXR(KK)=RMU(KK)*(ETY(KV,J,1)*UET(KK)+ZTY(KV,J,1)*
C      1 UZT(KK)+ETX(KV,J,1)*VET(KK)+ZTX(KV,J,1)*VZT(KK))
C
C      GENERATING THE HEAT FLUX TERMS
C
C      TX(KK)=ETX(KV,J,1)*TET(KK)+ZTX(KV,J,1)*TZT(KK)
C      TY(KK)=ETY(KV,J,1)*TET(KK)+ZTY(KV,J,1)*TZT(KK)
C
C      2 CONTINUE

```



```

1 RHOW(1,1,1),RHOE(62,30,1)
COMMON /DEPP/ RHOP(62,30,1),RHOUP(62,30,1),RHOVP(62,30,1),
1 RHOWP(1,1,1),RHOEP(62,30,1)
COMMON /DAMP/ ADD1(62),ADD2(62),ADD3(62),ADD5(62)
DIMENSION U(62),V(62),C(62),UET(62),UZT(62)
REAL GAMM2

C
GAMM2=GAMMA*GAMM1
RDET=1.0/DETA
RDZT=1.0/DZETA
RHOWP(1,1,1)=0.0
RHOW (1,1,1)=0.0

C
IF(L.EQ.2) GO TO 100

C
*****
PREDICTOR SWEEPS
*****

C
DO 1 KV=2,KLM
KM=KV-1
RHOE(KV,J,1)=RHO(KV,J,1)-DT*((ETX(KV,J,1)*(F21(KV,2)-F21(KV,1
1))+ETY(KV,J,1)*(G21(KV,2)-G21(KV,1)))*RDET+(ZTX(KV,J,1)*
2 (F31(KV)-F31(KM))+ZTY(KV,J,1)*(G31(KV)-G31(KM)))*RDZT)

C
RHOUP(KV,J,1)=RHOUP(KV,J,1)-DT*((ETX(KV,J,1)*(F22(KV,2)-F22(KV
1,1))+ETY(KV,J,1)*(G22(KV,2)-G22(KV,1)))*RDET+(ZTX(KV,J,1)*
2 (F32(KV)-F32(KM))+ZTY(KV,J,1)*(G32(KV)-G32(KM)))*RDZT)

C
CONTINUE
1
C
DO 2 KV=2,KLM
C
KM=KV-1
C

```

```

C      RHOVP(KV,J,1)=RHOV(KV,J,1)-DT*((ETX(KV,J,1))*(F23(KV,2))-F23(KV
1,1))+ETY(KV,J,1)*(G23(KV,2)-G23(KV,1))*RDET+(ZTX(KV,J,1)*
2 (F33(KV)-F33(KM))+ZTY(KV,J,1)*(G33(KV)-G33(KM)))*RDZT)

C      RHOEP(KV,J,1)=RHOE(KV,J,1)-DT*((ETX(KV,J,1))*(F25(KV,2))-F25(KV
1,1))+ETY(KV,J,1)*(G25(KV,2)-G25(KV,1))*RDET+(ZTX(KV,J,1)*
2 (F35(KV)-F35(KM))+ZTY(KV,J,1)*(G35(KV)-G35(KM)))*RDZT)

C      CONTINUE
C      IF((ISMTHX.EQ.0).AND.(ISMTHY.EQ.0)) GO TO 200
C      CALL DAMPING(J)
C      DO 10 KV=2,KLM
C      RHO (KV,J,1)=RHOP (KV,J,1)+ADD1(KV)
RHOUP(KV,J,1)=RHOUP(KV,J,1)+ADD2(KV)
RHOVP(KV,J,1)=RHOVP(KV,J,1)+ADD3(KV)
RHOEP(KV,J,1)=RHOEP(KV,J,1)+ADD5(KV)
10 CONTINUE
C      GO TO 200
C      *****
C      CORRECTOR SWEEPS
C      *****
C      DO 3 KV=2,KLM
KM=KV-1
C      RHO(KV,J,1)=0.5*(RHO(KV,J,1)+RHOP(KV,J,1)-DT*((ETX(KV,J,1)*
1 (F21(KV,2)-F21(KV,1))+ETY(KV,J,1)*(G21(KV,2)-G21(KV,1))*RDET
2 +(ZTX(KV,J,1)*(F31(KV)-F31(KM))+ZTY(KV,J,1)*(G31(KV)-G31(KM)))*
3 *RDZT))
C

```

```

RHO(KV,J,1)=0.5*(RHO(KV,J,1)+RHO(KV,J,1)-DT*((ETX(KV,J,1)
1 *(F22(KV,2)-F22(KV,1))+ETY(KV,J,1)*(G22(KV,2)-G22(KV,1)))*RDET
2 +(ZTX(KV,J,1)*(F32(KV)-F32(KM))+ZTY(KV,J,1)*(G32(KV)-G32(KM))))
3 *RDZT))

```

C

```

CONTINUE

```

3

C

```

DO 4 KV=2,KLM

```

C

```

KM=KV-1

```

C

```

RHOV(KV,J,1)=0.5*(RHOV(KV,J,1)+RHOV(KV,J,1)-DT*((ETX(KV,J,1)
1 *(F23(KV,2)-F23(KV,1))+ETY(KV,J,1)*(G23(KV,2)-G23(KV,1)))*RDET
2 +(ZTX(KV,J,1)*(F33(KV)-F33(KM))+ZTY(KV,J,1)*(G33(KV)-G33(KM))))
3 *RDZT))

```

C

```

RHOE(KV,J,1)=0.5*(RHOE(KV,J,1)+RHOE(KV,J,1)-DT*((ETX(KV,J,1)
1 *(F25(KV,2)-F25(KV,1))+ETY(KV,J,1)*(G25(KV,2)-G25(KV,1)))*RDET
2 +(ZTX(KV,J,1)*(F35(KV)-F35(KM))+ZTY(KV,J,1)*(G35(KV)-G35(KM))))
3 *RDZT))

```

C

```

CONTINUE

```

4

C

```

IF((ISMTHX.EQ.0).AND.(ISMTHY.EQ.0)) GO TO 200

```

C

```

CALL DAMPING(J)

```

C

```

DO 20 KV=2,KLM

```

C

```

RHO(KV,J,1)=RHO(KV,J,1)+ADD1(KV)
RHO(KV,J,1)=RHO(KV,J,1)+ADD2(KV)
RHOV(KV,J,1)=RHOV(KV,J,1)+ADD3(KV)
RHOE(KV,J,1)=RHOE(KV,J,1)+ADD5(KV)

```

C

```

CONTINUE

```

20

```

C 200 RETURN
      END
      SUBROUTINE DAMPING(J)
      COMMON / / DETA,DZETA,CV,RC,PR,PRT,GAMMA,EP(62,30,1),DTL(30),
1 GAMM1,CFL,BETA,UINF,RHOINF,CINF,TINF,DT,CX,CY,L,DTC(62),KG,
2 IL,JL,KL,ILM,JLM,KLM,ILE,LS,ISMTHX,ISMTHY,DELTA,DELTAD,TW1,TW2
      COMMON /DEP/ RHO(62,30,1),RHOUP(62,30,1),RHOV(62,30,1),
1 RHOV(1,1,1),RHOE(62,30,1)
      COMMON /DEPP/ RHOE(62,30,1),RHOUP(62,30,1),RHOVP(62,30,1),
1 RHOVP(1,1,1),RHOEP(62,30,1)
      COMMON /DAMP/ ADD1(62),ADD2(62),ADD3(62),ADD5(62)
      COMMON /DV/ R(62,30,1),U(62,30,1),V(62,30,1),W(1,1,1),
1 P(62,30,1),T(62,30,1)
      COMMON /TV/ ETX(62,30,1),ETY(62,30,1),ZTX(62,30,1),ZTY(62,30,1)
      DIMENSION ADDG1(62),ADDG2(62),ADDG3(62),
2 ADDG5(62),ADDH1(62),ADDH2(62),ADDH3(62),
3 ADDH5(62),PD(62,2)

      KLM2=KLM-1
      GAMMR=GAMMA*RC
      RDET=1.0/DETA
      RDZT=1.0/DZETA

C      SET DAMPING TERMS TO ZERO FOR END POINTS
C
C      DO 1 KV=1,KL
C
C          ADDG1(KV)=0.0
C          ADDG2(KV)=0.0
C          ADDG3(KV)=0.0
C          ADDG5(KV)=0.0
C
C          ADDH1(KV)=0.0
C          ADDH2(KV)=0.0

```

```

C      1
C      ADDH3(KV)=0.0
C      ADDH5(KV)=0.0
C      CONTINUE
C      *** GENERATING ADDG ***
C      IF((J.LE.2).OR.(J.GE.JLM)) GO TO 200
C
C      DO 110 M=1,2
C
C      JV=J+M+L-3
C      JP=JV+1
C      JM=JV-1
C
C      DO 120 KV=1,KL
C      PD(KV,M)=CY*(ABS(P(KV,JP,1))-2.0*P(KV,JV,1)+
C      1 P(KV,JM,1))/(P(KV,JP,1)+2.0*P(KV,JV,1)+P(KV,JM,1))*
C      2 (ABS(ETX(KV,JV,1)*U(KV,JV,1)+ETY(KV,JV,1)*V(KV,JV,1))+
C      3 SQRT(GAMMR*T(KV,JV,1)*(ETX(KV,JV,1)**2+ETY(KV,JV,1)**2)))
C      120 CONTINUE
C      110 CONTINUE
C
C      IF(L.EQ.2) GO TO 140
C
C      PREDICTOR
C
C      JP=J+1
C      JM=J-1
C
C      DO 130 KV=1,KL
C
C      ADDG1(KV)=DT*(PD(KV,2)*(RHO (KV,JP,1)-RHO (KV,J,1))-
C      1 PD(KV,1)*(RHO (KV,J,1)-RHO (KV,JM,1)))*RDET
C      ADDG2(KV)=DT*(PD(KV,2)*(RHO(KV,JP,1)-RHO(KV,J,1))-

```

```

1 PD(KV,1)*(RHO(KV,J,1)-RHO(KV,JM,1))*RDET
  ADDG3(KV)=DT*(PD(KV,2)*(RHO(KV,JP,1)-RHO(KV,J,1))-
1 PD(KV,1)*(RHO(KV,J,1)-RHO(KV,JM,1))*RDET
  ADDG5(KV)=DT*(PD(KV,2)*(RHO(KV,JP,1)-RHO(KV,J,1))-
1 PD(KV,1)*(RHO(KV,J,1)-RHO(KV,JM,1))*RDET
C
130 CONTINUE
C
GO TO 200
C
CORRECTOR
140 JP=J+1
  JM=J-1
C
DO 150 KV=1,KL
C
  ADDG1(KV)=DT*(PD(KV,2)*(RHO(KV,JP,1)-RHO(KV,J,1))-
1 PD(KV,1)*(RHO(KV,J,1)-RHO(KV,JM,1))*RDET
  ADDG2(KV)=DT*(PD(KV,2)*(RHO(KV,JP,1)-RHO(KV,J,1))-
1 PD(KV,1)*(RHO(KV,J,1)-RHO(KV,JM,1))*RDET
  ADDG3(KV)=DT*(PD(KV,2)*(RHO(KV,JP,1)-RHO(KV,J,1))-
1 PD(KV,1)*(RHO(KV,J,1)-RHO(KV,JM,1))*RDET
  ADDG5(KV)=DT*(PD(KV,2)*(RHO(KV,JP,1)-RHO(KV,J,1))-
1 PD(KV,1)*(RHO(KV,J,1)-RHO(KV,JM,1))*RDET
C
150 CONTINUE
C
*** GENERATING ADDH ***
C
DO 200 M=1,2
DO 220 K=3,KLM2
C
  KV=K+M+L-3
  KP=KV+1

```



```

C      KM=KV-1
      PD(K,M)=CX*(ABS(P(KP,J,1)-2.0*P(KV,J,1))+
1 P(KM,J,1))/(P(KP,J,1)+2.0*P(KV,J,1)+P(KM,J,1))*
2 (ABS(ZTX(KV,J,1)*U(KV,J,1)+ZTY(KV,J,1)*V(KV,J,1))+
3 SQR(GAMMR*T(KV,J,1)*(ZTX(KV,J,1)**2+ZTY(KV,J,1)**2)))
C
220  CONTINUE
210  CONTINUE
C      IF(L.EQ.2) GO TO 240
      PREDICTOR
C
DO 230 KV=3,KLM2
C      KP=KV+1
      KM=KV-1
C
      ADDH1(KV)=DT*(PD(KV,2)*(RHO(KP,J,1)-RHO(KV,J,1))-
1 PD(KV,1)*(RHO(KV,J,1)-RHO(KM,J,1))*RDZT
      ADDH2(KV)=DT*(PD(KV,2)*(RHO(KP,J,1)-RHO(KV,J,1))-
1 PD(KV,1)*(RHO(KV,J,1)-RHO(KM,J,1))*RDZT
      ADDH3(KV)=DT*(PD(KV,2)*(RHO(KP,J,1)-RHO(KV,J,1))-
1 PD(KV,1)*(RHO(KV,J,1)-RHO(KM,J,1))*RDZT
      ADDH5(KV)=DT*(PD(KV,2)*(RHO(KP,J,1)-RHO(KV,J,1))-
1 PD(KV,1)*(RHO(KV,J,1)-RHO(KM,J,1))*RDZT
C
230  CONTINUE
C      GO TO 300
      CORRECTOR
C
240  DO 250 KV=3,KLM2

```

```

C
  KP=KV+1
  KM=KV-1
C
  ADDH1(KV)=DT*(PD(KV,2)*(RHOP (KP,J,1)-RHOP (KV,J,1))-
1 PD(KV,1)*(RHOP (KV,J,1)-RHOP (KM,J,1)))*RDZT
  ADDH2(KV)=DT*(PD(KV,2)*(RHOUP(KP,J,1)-RHOUP(KV,J,1))-
1 PD(KV,1)*(RHOUP(KV,J,1)-RHOUP(KM,J,1)))*RDZT
  ADDH3(KV)=DT*(PD(KV,2)*(RHOVP(KP,J,1)-RHOVP(KV,J,1))-
1 PD(KV,1)*(RHOVP(KV,J,1)-RHOVP(KM,J,1)))*RDZT
  ADDH5(KV)=DT*(PD(KV,2)*(RHOEP(KP,J,1)-RHOEP(KV,J,1))-
1 PD(KV,1)*(RHOEP(KV,J,1)-RHOEP(KM,J,1)))*RDZT
C
250  CONTINUE
C
C
C
C
C
C
  SUMMING THE ARTIFICIAL VISCOSITY-LIKE TERMS
C
300  DO 310 KV=1,KL
C
  ADD1(KV)=ISMTHX*ADDG1(KV)+ISMTHY*ADDH1(KV)
  ADD2(KV)=ISMTHX*ADDG2(KV)+ISMTHY*ADDH2(KV)
  ADD3(KV)=ISMTHX*ADDG3(KV)+ISMTHY*ADDH3(KV)
  ADD5(KV)=ISMTHX*ADDG5(KV)+ISMTHY*ADDH5(KV)
C
310  CONTINUE
C
  RETURN
  END

```

```

PROGRAM STEADY (INPUT,OUTPUT,TAPE1=INPUT,TAPE6=OUTPUT,TAPE2,TAPE3,
1 TAPE4)
C THIS PROGRAM COMPUTES THE RATIO H/HREF TO DETERMINE WHETHER THE
C NAVIER-STOKES SOLUTION HAS REACHED STEADY-STATE CONVERGENCE.
C THIS CODE IS WRITTEN IN FORTRAN IV AND IS RUN ON A CDC CYBER 750.
C DECLARATIONS AND DIMENSIONING
REAL EP(62,30,1),H(62),HFRAC(62),HREF(62),RHO(62,30,1),RHOE(62,30,
1 1),RHOV(62,30,1),RHOV(62,30,1),RHOW(1,1,1),T(62,30),X(62,30,1)
2 ,Y(62,30,1),XL(62)

REAL CP,CV,DT,DY,MINF,MUINF,MU,PR,R,RH,RHOINF,TAW,TINF,TMS1
1 ,TMS2,T0,UINF,MU,MU0,U,V,RL,TW,KAIR,DTDY,DETA
INTEGER NI,I,J,K,L
C READ THE SETUP FILE
READ(1,*) UINF,RHOINF,MUINF,TINF,MINF,RL,L
C READ THE RESTART FILE
READ(2) NI,TMS1,TMS2,RHO,RHOV,RHOW,RHOE,X,Y,EP
C COMPUTE FLOW CONDITIONS
R=1716.
T0=2000.
CP=6006.
CV=4290.
MU0=2.27E-8
PR=0.72
DETA=1.0/29.0
DO 20 K=2,62
DO 10 J=1,30
RH=1.0/RHO(K,J,1)
U=RHOV(K,J,1)*RH
V=RHOV(K,J,1)*RH
T(K,J)=(RHOE(K,J,1)*RH-(U**2.+V**2.)/2.)/CV
10 CONTINUE
20 CONTINUE
C COMPUTE THE ADIABATIC WALL TEMPERATURE
TAW=TINF+0.9*((UINF**2.)/(2.*CP))
C COMPUTE HREF (IN BTU/SQFT*SEC*DEGREE R)

```

```

DO 30 K=2,62
  HREF(K)=(0.332*CP*SQRT((MUINF*RHOFNF*UINF)/X(K,1,1)))/(PR** (2./
1    3.)*778.0)
30 CONTINUE
C COMPUTE THE ISOTHERMAL HEAT TRANSFER AT THE WALL
C IN BTU/SQFT*SEC*DEGREE R
DO 40 K=2,62
  IF (K.LE.31) TW=540.0
  IF (K.GT.31) TW=700.0
  IF (L.EQ.1) TW=540.0
  MU=(MU0*TW**1.5)/(TW+198.6)
  KAIR=(MU*CP)/(PR*778.0)
  DT=(-3.0*T(K,1)+4.0*T(K,2)-T(K,3))/(2.0*DETA)
  DY=(-3.0*Y(K,1,1)+4.0*Y(K,2,1)-Y(K,3,1))/(2.0*DETA)
  DTDY=DT/DY
  H(K)=(-KAIR*DTDY)/(TW-TAW)
40 CONTINUE
C COMPUTE THE RATIO H/HREF
DO 50 K=2,62
  HFRAC(K)=H(K)/HREF(K)
50 CONTINUE
C COMPUTE THE NONDIMENSIONAL LENGTH X/L
DO 51 I=1,62
  XL(I)=X(I,1,1)/RL
51 CONTINUE
C OUTPUT SECTION
WRITE(3,41) NI
41 FORMAT(1X,'##### THE BEGINNING ITERATION IS *,I5,* #####')
WRITE(3,42)
42 FORMAT(9X,'X/L*,9X,'HREF*,18X,'H*,18X,'HFRAC*')
DO 60 K=2,62
  WRITE(3,45) XL(K),HREF(K),H(K),HFRAC(K)
45 FORMAT(1X,4(3X,E14.4))
  WRITE(4,46) XL(K),HFRAC(K)
46 FORMAT(1X,2(F14.8,3X))

```

60 CONTINUE  
END

### VITA

Timothy Kenneth Roberts was born on 28 June 1953 in Wilmington, Delaware. He graduated from high school in High Point, North Carolina in 1971. He graduated cum laude from North Carolina State University in 1975, receiving a Bachelor of Science in Aerospace Engineering degree. Upon graduation, he received a commission in the United States Air Force. Entering active duty in August 1975, he attended Minuteman Mod Initial Qualification training at Vandenberg Air Force Base, California. He then served four years as a missile combat crewmember at Ellsworth Air Force Base, South Dakota. His next assignment was to Headquarters, Foreign Technology Division at Wright-Patterson Air Force Base, Ohio. He served two and a half years as a ballistic missile systems engineer. In June 1982, he entered the School of Engineering, Air Force Institute of Technology. Since January 1984, Captain Roberts has been serving as a section chief at the Air Force Rocket Propulsion Laboratory, Edwards Air Force Base, California.

Permanent address: 2101 E. Lexington Ave.

High Point, North Carolina, 27262

UNCLASSIFIED

SECURITY CLASSIFICATION OF THIS PAGE

## REPORT DOCUMENTATION PAGE

1a. REPORT SECURITY CLASSIFICATION UNCLASSIFIED			1b. RESTRICTIVE MARKINGS		
2a. SECURITY CLASSIFICATION AUTHORITY			3. DISTRIBUTION/AVAILABILITY OF REPORT Approved for public release; distribution unlimited.		
2b. DECLASSIFICATION/DOWNGRADING SCHEDULE					
4. PERFORMING ORGANIZATION REPORT NUMBER(S) AFIT/GAE/AA/85M-5			5. MONITORING ORGANIZATION REPORT NUMBER(S)		
6a. NAME OF PERFORMING ORGANIZATION School of Engineering Air Force Instit. of Tech.		6b. OFFICE SYMBOL (If applicable) AFIT/EN	7a. NAME OF MONITORING ORGANIZATION		
6c. ADDRESS (City, State and ZIP Code) Wright-Patterson AFB, OH 45433			7b. ADDRESS (City, State and ZIP Code)		
8a. NAME OF FUNDING/SPONSORING ORGANIZATION		8b. OFFICE SYMBOL (If applicable)	9. PROCUREMENT INSTRUMENT IDENTIFICATION NUMBER		
8c. ADDRESS (City, State and ZIP Code)			10. SOURCE OF FUNDING NOS.		
			PROGRAM ELEMENT NO.	PROJECT NO.	TASK NO.
11. TITLE (Include Security Classification) See Box 19.			WORK UNIT NO.		
12. PERSONAL AUTHOR(S) Timothy K. Roberts, Captain, USAF					
13a. TYPE OF REPORT MS Thesis		13b. TIME COVERED FROM _____ TO _____		14. DATE OF REPORT (Yr., Mo., Day) March 1985	
15. PAGE COUNT 129					
16. SUPPLEMENTARY NOTATION					
17. COSATI CODES			18. SUBJECT TERMS (Continue on reverse if necessary and identify by block number)		
FIELD	GROUP	SUB. GR.	Aerodynamic Heating		
1	1	26	Convection (Heat Transfer)		
			Heat Transfer Coefficients		
			Navier-Stokes Equations		
			Numerical Methods & Procedures		
19. ABSTRACT (Continue on reverse if necessary and identify by block number)					
Title: A NUMERICAL SOLUTION OF A NONISOTHERMAL WALL USING THE TWO-DIMENSIONAL NAVIER-STOKES EQUATIONS.					
Thesis Advisor: James K. Hodge, Major, USAF					
<div style="text-align: right;"> <p>Approved for public release: IAW AFR 190-17</p> <p><i>John E. Glover</i> 12afit/EN</p> <p>Dean for Research and Professional Development</p> <p>Air Force Institute of Technology (AFIT)</p> <p>Wright-Patterson AFB OH 45433</p> </div>					
20. DISTRIBUTION/AVAILABILITY OF ABSTRACT UNCLASSIFIED/UNLIMITED <input type="checkbox"/> SAME AS RPT <input checked="" type="checkbox"/> DTIC USERS <input type="checkbox"/>			21. ABSTRACT SECURITY CLASSIFICATION UNCLASSIFIED		
22a. NAME OF RESPONSIBLE INDIVIDUAL James K. Hodge, Major, USAF		22b. TELEPHONE NUMBER (Include Area Code) (513) 257-3517		22c. OFFICE SYMBOL AFIT/EN	

Wind tunnel tests of Space Shuttle Orbiter insulating articles have demonstrated the presence of a nonisothermal wall effect, which is a lag in heat transfer recovery after the flow passes over a surface temperature discontinuity resulting in a downstream transport of energy. Theoretical analyses and numerical simulations of hypersonic flow over discontinuous nonisothermal surfaces using boundary layer theory have also indicated the presence of this effect.

This thesis studies the nonisothermal wall effect by modeling the hypersonic flow over an inclined wedge with a discontinuous nonisothermal surface. The flow is modeled using the two-dimensional Navier-Stokes equations. MacCormack's method is used to solve the Navier-Stokes equations. The program used to implement these methodologies is discussed and a listing given. A semi-adaptive grid is used to represent the physical conditions of the problem. Heat transfer is presented as a nondimensional ratio of the local convective heat transfer coefficient to a reference heat transfer coefficient.

The results of this study show that the nonisothermal wall effect can be successfully modeled using the two-dimensional Navier-Stokes equations and MacCormack's explicit method. The lag in the recovery of the convective heat transfer coefficient is found to match lags seen in other analyses of the problem. Due to the high Mach number modeled, a shock wave-boundary layer interaction is found to have an effect on heat transfer. A significant surface pressure spike is found to occur downstream of the discontinuity, which may be a result of the increase in size of the momentum and thermal boundary layers at the discontinuity.

The study concludes that the nonisothermal wall effect can be adequately modeled by the two-dimensional Navier-Stokes equations; that the shock wave-boundary layer interaction does have an effect on the heat transfer; and that the occurrence of a spike in surface pressure may be a unique result of the nonisothermal wall effect. Significant recommendations include the need for further study of the nonisothermal wall effect, the need to use more optimal grids and solution methods, the need to more thoroughly investigate the shock wave-boundary layer effect, and the need for further study of the surface pressure response to the nonisothermal wall effect.



**END**

**FILMED**

**7-85**

**DTIC**